

DESIGN, OPTIMIZATION AND TESTING OF MICRO-EVAPORATOR AND
MICRO-CONDENSER COMPONENTS USED IN A MINIATURE VAPOR
COMPRESSION REFRIGERATION CYCLE

A THESIS SUBMITTED TO
THE GRADUATE SCHOOL OF NATURAL AND APPLIED SCIENCES
OF
MIDDLE EAST TECHNICAL UNIVERSITY

BY

GÖKER TÜRKAKAR

IN PARTIAL FULLFILLMENT OF THE REQUIREMENTS
FOR
THE DEGREE OF DOCTOR OF PHILOSOPHY
IN
MECHANICAL ENGINEERING

SEPTEMBER 2016

Approval of the thesis:

**DESIGN, OPTIMIZATION AND TESTING OF MICRO-EVAPORATOR
AND MICRO-CONDENSER COMPONENTS USED IN A MINIATURE
VAPOR COMPRESSION REFRIGERATION CYCLE**

submitted by **GÖKER TÜRKAKAR** in partial fulfillment of the requirements for the degree of **Doctor of Philosophy in Department of Mechanical Engineering, Middle East Technical University** by,

Prof. Dr. Gülbin Dural Ünver
Dean, Graduate School of **Natural and Applied Sciences**

Prof. Dr. Tuna Balkan
Head of Department, **Mechanical Engineering**

Assoc. Prof. Dr. Tuba Okutucu-Özyurt
Supervisor, **Mechanical Engineering Dept., METU**

Examining Committee Members:

Assoc. Prof. Dr. Cüneyt Sert
Mechanical Engineering Dept., METU

Assoc. Prof. Dr. Tuba Okutucu-Özyurt
Mechanical Engineering Dept., METU

Prof. Dr. L. Berrin Erbay
Mechanical Engineering Dept., Eskişehir Osmangazi University

Assoc. Prof. Dr. Murat Kadri Aktaş
Mechanical Engineering Dept., TOBB University

Assist. Prof. Dr. Özgür Bayer
Mechanical Engineering Dept., METU

Date: 09.09.2016

I hereby declare that all information in this document has been obtained and presented in accordance with academic rules and ethical conduct. I also declare that, as required by these rules and conduct, I have fully cited and referenced all material and results that are not original to this work.

Name, Last Name: GÖKER TÜRKAAR

Signature:

ABSTRACT

DESIGN, OPTIMIZATION AND TESTING OF MICRO-EVAPORATOR AND MICRO-CONDENSER COMPONENTS USED IN A MINIATURE VAPOR COMPRESSION REFRIGERATION CYCLE

TÜRKAKAR, Göker

Ph.D., Department of Mechanical Engineering

Supervisor: Associate Professor Dr. Tuba OKUTUCU-ÖZYURT

September 2016, 146 pages

This study aims to optimize the dimensions and operating conditions of two main components of a miniature vapor compression refrigeration cycle (MVCRC), evaporator and condenser by using entropy generation minimization (EGM). In addition, some performance tests are conducted on a MVCRC which is constructed based on the EGM analysis as long as the manufacturing constraints permit. R134a is used as the coolant.

Entropy generation rate in the evaporator of the MVCRC is investigated under the effects of exit vapor quality, mass and heat flux, saturation temperature, and channel dimensions. Dimensionless entropy generation number for the condenser of the MVCRC is investigated under the effects of fin pitch, fin height, louver angle and air

mass flow rate on the air side, hydraulic diameter of the channel for the refrigerant side.

The exit vapor quality of the evaporator yielding the minimum entropy generation rate is found as 0.846. The optimum channel and fin widths are 66 and 50 μm , respectively, for 700 μm channel height. Heat transfer is the major source of the total entropy production for 200-400 μm wide channels, while the contribution of pressure drop becomes comparable for narrower channels.

The optimum air mass flow rate interval for the condenser is found to be between 0.055-0.1 kg s^{-1} for a given fin pitch interval of 1-1.6 mm. The entropy generation number due to pressure drop on the air side becomes dominant for mass flow rates greater than 0.08 kg s^{-1} .

Experimental results match well with the theoretical calculations. A maximum COP of 7.71 is obtained under 96 W cooling load.

Keywords: Miniature Vapor Compression Refrigeration Cycle, Micro-Evaporator, Micro-Condenser, Entropy Generation Minimization, Dimensional Optimization, R134a.

ÖZ

MİNYATÜR BİR BUHAR SIKIŞTIRMALI SOĞUTMA ÇEVİRİMİNDE KULLANILAN MİKRO-EVAPORATÖR VE MİKRO KONDENSER BİLEŞENLERİNİN TASARIM, OPTİMİZASYON VE TESTLERİ

TÜRKAKAR, Göker

Doktora, Makina Mühendisliği Bölümü

Tez Yöneticisi: Doç. Dr. Tuba OKUTUCU-ÖZYURT

Eylül 2016, 146 sayfa

Bu çalışma, minyatür buhar sıkıştırırmalı soğutma çevriminin (MBSSÇ) ana bileşenleri olan evaporatör ve kondenser boyutlarını ve çalışma koşullarını entropi üretimi minimizasyonu (EÜM) ile optimize etmeyi amaçlar. Bunun haricinde üretim kısıtlarının elverdiği ölçüde EÜM analizi sonucuna dayalı olarak üretilmiş olan MBSSÇ üzerinde bazı performans testleri yapılmıştır. R134a soğutucu akışkan olarak kullanılmıştır.

MBSSÇ'nin evaporatör bileşenindeki entropi üretimi, çıkış buhar kalitesi, ısı ve kütle akısı, doyma sıcaklığı, ve kanal boyutlarına göre değerlendirilmiştir. MBSSÇ'nin kondenser bileşeninde boyutsuz entropi üretim sayısı, hava tarafı için kanatçık aralığı,

kanatçık yüksekliği, panjur açısı, hava debisi; soğutkan tarafı için ise kanal hidrolik çapı değiştirilerek incelenmiştir.

Entropi üretiminin minimum olduğu evaporatör buhar çıkış kalitesi, 0.846 olarak bulunmuştur. Kanal yüksekliği 700 μm olan durum için optimum kanal ve kanatçık genişliği sırasıyla, 66 ve 50 μm 'dir. Genişliği 200-400 μm olan kanallar için entropi üretimi ağırlıklı olarak ısı transferiyle gerçekleşirken daha dar kanallar için basınç düşümü kaynaklı entropi üretimi kıyaslanabilir hale gelmektedir.

Kanatçık genişliğinin 1-1.6 mm aralığında olduğu durumda, optimum hava debisi 0.055-0.1 kg s^{-1} aralığında belirlenmiştir. Hava tarafında basınç düşümü kaynaklı entropi üretimi sayısı, 0.08 kg s^{-1} hava debisinden sonra baskın hale gelmektedir.

Anahtar Kelimeler: Minyatür Buhar Sıkıştırılmalı Soğutma Çevrimi, Mikro Evaporatör, Mikro Kondenser, Entropi Üretimi Minimizasyonu, Boyutsal Optimizasyon, R134a.

To my family...

ACKNOWLEDGEMENTS

I would like to express my gratitude to my advisor Dr. Tuba Okutucu for her great support and perfect guidance and encouragement. I would like to thank to my advisory committee members Dr. Cüneyt Sert and Dr. Murat Kadri Aktaş for their valuable comments and suggestions on my study. I would like to thank also Dr. Satish G. Kandlikar who supervised my studies in RIT, USA.

I would like to thank to Rahim Jafari and Mustafa Yalçın for their support and friendship during my experimental studies. I want to thank all the people I worked with in METU. I would like to especially thank to last generation TA's Onur Özkan, Mine Kaya, Serhat Bilyaz, Eylül Şimşek, Erdem Dursunkaya, Berke Harmancı and Serdar Hiçdurmaz. I had a great time while I was working and spending time with you.

I want to thank to Yiğit Ata Ağartan, Melih Çalamak, Bilgehan Tekin, Mine Özdemir Tekin, Seyfettin Yıldız, Zuhul Karakoç Yıldız, Murat Özkaptan for their sincere friendship and support. A special thanks to Mustafa Koz and Olivia Scheibel who made me feel at home with their great friendship during my stay in USA. I also want to thank to labmates Vickie Chiang and Isaac Peres for their sincere friendship and help.

This study has been supported by “The Scientific and Technological Research Council of Turkey, TÜBİTAK” under grant number 112M168.

The studies conducted in the Thermal Analysis, Microfluidics, and Fuel Cell Laboratory at Rochester Institute of Technology, Rochester, NY, USA have also been supported by “The Scientific and Technological Research Council of Turkey, TÜBİTAK” through the visiting scholar program 2214a.

TABLE OF CONTENTS

ABSTRACT	v
ÖZ	vii
ACKNOWLEDGEMENTS	x
TABLE OF CONTENTS	xi
LIST OF TABLES	xiv
LIST OF FIGURES	xvi
LIST OF SYMBOLS AND ABBREVIATIONS	xix
1 INTRODUCTION	1
1.1 Motivation	1
1.2 Scope of the Study	2
1.2.1 Evaporator Design	3
1.2.2 Condenser Design	3
1.2.3 Experimental Studies	4
1.3 Literature Survey	5
1.3.1 Microscale Vapor Compression Refrigeration Cycles	5
1.3.2 Evaporation Studies in Microchannels	8
1.3.3 Condensation Studies in Microchannels	11
1.3.4 Entropy Generation Minimization	12
1.4 Thesis Outline	14
2 EVAPORATOR DESIGN	17

2.1	Problem Definition	17
2.2	Second Law Modeling.....	19
2.3	Hydrodynamic Theory.....	22
2.4	Thermal Theory	25
2.5	Fin Model	27
2.6	Solution Methodology and Code Validation	28
2.7	Optimization Study.....	34
2.7.1	Optimization Methodology	35
2.8	Evaporator Results.....	38
2.8.1	Entropy Generation Rate Analysis	38
2.8.2	Optimization Results	43
3	CONDENSER DESIGN	49
3.1	Problem Definition	49
3.2	Second Law Modeling.....	53
3.3	Computational Algorithm.....	56
3.4	Thermal Analysis.....	59
3.5	Hydrodynamic Analysis	66
3.6	Validation of Computer Code.....	69
3.7	Condenser Results	71
4	EXPERIMENTS	83
4.1	Experimental Setup.....	84
4.1.1	Components of the Cycle and Measuring Devices	84
4.1.2	Microchannel Evaporator	88
4.1.3	Microchannel Condenser.....	91
4.2	Energy Balance for the Refrigeration Cycle.....	94

4.3	Uncertainty Analysis	97
4.4	Experimental Results.....	102
4.5	Performance Comparison of the Present Study with the Literature	110
4.6	Comparison of Experiment Results with Theory	112
5	CONCLUSIONS AND FUTURE RECOMMENDATIONS	125
5.1	Evaporator	125
5.2	Condenser	126
5.3	Experiments.....	128
5.4	Future Work	130
	REFERENCES.....	131
	CURRICULUM VITAE	141

LIST OF TABLES

TABLES

Table 1.1 Miniature vapor compression refrigeration cycles, some data is obtained from [4]	7
Table 1.2 Microchannel evaporation studies in the literature	10
Table 1.3 Summary of microchannel condensation studies in the literature	12
Table 2.1 Cooling load and main dimensions of Intel Core i7-900, [45].	18
Table 2.2 Values of examined parameters	19
Table 2.3 Interval of design variables and grid numbers	35
Table 2.4 Optimization Results for $H = 500 \mu\text{m}$, $q'' = 47.74 \text{ W cm}^{-2}$	44
Table 2.5 Optimization Results for $H = 600 \mu\text{m}$, $q'' = 47.74 \text{ W cm}^{-2}$	44
Table 2.6 Optimization Results for $H = 700 \mu\text{m}$, $q'' = 47.74 \text{ W cm}^{-2}$	46
Table 3.1 Fixed parameters of the condenser	50
Table 3.2 Fixed dimensions of the condenser	52
Table 3.3 Ranges of examined parameters	52
Table 3.4 Input parameters and results of the validation case (Yuan et al. [5])	70
Table 4.1 Experiments matrix	83
Table 4.2 Application and specifications of the components used in the test setup. Some information is obtained from [4]	87
Table 4.3 Condenser dimensions used	92
Table 4.4 Temperatures and pressures at various states of the cycle at $\dot{Q}_{evap} = 70 \text{ W}$	95
Table 4.5 Fan stages and corresponding velocities	96
Table 4.6 Uncertainty of direct measurements. Some data is obtained from [4]	98
Table 4.7 Uncertainty results of calculated parameters. Some data is obtained from [4]	102
Table 4.8 Performance parameters of MVCRC's available in the literature and present study	111
Table 4.9 Input parameters for the inspected case	114
Table 4.10 Comparison of theoretical and experimental results for the evaporator	115

Table 4.11 Condenser parameters for comparison.....	121
Table 4.12 Comparison of the condenser length used in the experiments and found by louvered fin model.	121
Table 4.13 Comparison of the condenser length used in the experiments and found by plain fin model.	123

LIST OF FIGURES

FIGURES

Figure 2.1 Evaporator geometry (Türkakar and Okutucu-Özyurt [45]).....	17
Figure 2.2 T-s diagram for the evaporator	19
Figure 2.3 Microchannel heat sink and control volume (segment).....	20
Figure 2.4 Comparison of the variation of heat transfer coefficient with vapor quality as obtained by Bertsch et al. [12] and by the present study. Red-green and blue-purple markers correspond to the same conditions.	29
Figure 2.5 Comparison of the total pressure drop values of the present study, and those available in the literature (Lee and Mudawar [48], Qu and Mudawar [53]), $G= 415 \text{ kg m}^{-2} \text{ s}^{-1}$	32
Figure 2.6 Comparison of the pressure drop components of the present study and those available in the literature (Lee and Mudawar [48], Qu and Mudawar [53]), $G= 415 \text{ kg m}^{-2} \text{ s}^{-1}$	33
Figure 2.7 Computational algorithm for evaporator design calculations.....	37
Figure 2.8 Effect of mass flow rate on entropy generation rate for various heat and mass fluxes, $H = 500 \text{ }\mu\text{m}$, $T_{\text{sat}} = 20^\circ\text{C}$, $w_w = 250 \text{ }\mu\text{m}$, $x_{\text{out}} \cong 0.72\text{-}0.95$, $w_c = 200\text{:}10\text{:}400 \text{ }\mu\text{m}$	38
Figure 2.9 Effect of mass flow rate on entropy generation rate for various mass flux and channel height values, $q'' = 47.74 \text{ W cm}^{-2}$, $T_{\text{sat}} = 20^\circ\text{C}$, $w_w = 250 \text{ }\mu\text{m}$, $x_{\text{out}} \cong 0.72\text{-}0.93$, $w_c = 200\text{:}10\text{:}400 \text{ }\mu\text{m}$	39
Figure 2.10 Effect of mass flow rate on entropy generation rate at constant channel width and wall thickness for various heat flux values, $H = 700 \text{ }\mu\text{m}$, $T_{\text{sat}} = 20^\circ\text{C}$, $w_c = 200$, $w_w = 250 \text{ }\mu\text{m}$, $x_{\text{out}} \cong 0.74\text{-}0.91$	40
Figure 2.11 Effect of mass flow rate on entropy generation rate at constant channel width and wall thickness for various channel height values, $q'' = 47.74 \text{ W cm}^{-2}$, $T_{\text{sat}} = 20^\circ\text{C}$, $w_c = 200 \text{ }\mu\text{m}$, $w_w = 250 \text{ }\mu\text{m}$, $x_{\text{out}} \cong 0.74\text{-}0.91$	41
Figure 2.12 Effect of mass flux on entropy generation rate for various heat fluxes, and flow rates, $H = 700 \text{ }\mu\text{m}$, $T_{\text{sat}} = 20^\circ\text{C}$, $w_c = 400\text{:}10\text{:}200 \text{ }\mu\text{m}$, $w_w = 250 \text{ }\mu\text{m}$, $x_{\text{out}} \cong 0.90\text{--}0.92$	

Figure 2.13 Variation of entropy generation rate with mass flux for various saturation temperatures, $m = 1.01 \text{ g s}^{-1}$, $H = 700 \text{ }\mu\text{m}$, $q'' = 47.74 \text{ W cm}^{-2}$, $w_c = 400:10:200 \text{ }\mu\text{m}$, $w_w = 250 \text{ }\mu\text{m}$, x_{out} : varies.....	43
Figure 2.14 Contour plot of entropy generation rate for $H = 500 \text{ }\mu\text{m}$, $m = 1 \text{ g s}^{-1}$, $q'' = 47.74 \text{ W cm}^{-2}$	46
Figure 2.15 Contribution of heat transfer (HT) and pressure drop (PD) to the entropy generation rate of the optimized channels.....	48
Figure 2.16 Effect of mass flow rate on entropy generation rate at constant channel width and wall thickness for various channel height values, $q'' = 47.74 \text{ W cm}^{-2}$, $T_{\text{sat}} = 20^\circ\text{C}$, $w_c = 70 \text{ }\mu\text{m}$, $w_w = 50 \text{ }\mu\text{m}$, $x_{\text{out}} \cong 0.727\text{-}0.974$	48
Figure 3.1 Air cooled aluminum condenser geometry [56]	50
Figure 3.2 T-s diagram for the condenser	53
Figure 3.3 Control volume for a segment of the heat exchanger	54
Figure 3.4 Computational algorithm of the heat exchanger design	58
Figure 3.5 Fin pitch effect on entropy generation number and heat exchanger length for various mass flow rates	71
Figure 3.6 Fin height effect on entropy generation number and heat exchanger length for various mass flow rates	73
Figure 3.7 Entropy generation number map for the air mass flow rate and the hydraulic diameter ($\alpha_c = 1$)	74
Figure 3.8 Entropy generation number map for the air mass flow rate and the louver angle	75
Figure 3.9 Entropy generation number map for the fin pitch and the louver angle at a constant air mass flow rate of $m_a = 0.08 \text{ kg s}^{-1}$	76
Figure 3.10 Entropy generation number (a) and heat exchanger length (b) maps for the fin pitch and the hydraulic diameter ($\alpha_c = 1$) at the constant air mass flow rate of $m_a = 0.08 \text{ kg s}^{-1}$	78
Figure 3.11 Entropy generation number due to pressure drop and heat transfer	79
Figure 3.12 Entropy generation number distribution for superheated, two phase and subcooled parts.....	80
Figure 4.1 Schematic diagram of the test setup [4].....	85

Figure 4.2 Photograph of the test setup	86
Figure 4.3 Evaporator test piece [4]	88
Figure 4.4 Side view of the fabricated microchannels (dimensions in μm) [4]	89
Figure 4.5 Evaporator test section [4]	90
Figure 4.6 Condenser test piece [4]	91
Figure 4.7 Variation of COP and η_{II} with \dot{Q}_{evap} at different CP, RC= 64 g, FS = 1 103	
Figure 4.8 Variation of COP and η_{II} with T_{sat} at different \dot{Q}_{evap} , CP = 50%, RC = 64 g, FS = 1	104
Figure 4.9 Variation of T_{base} and h_{av} with T_{sat} for different, CP = 50%, RC = 64 g, FS= 1.	105
Figure 4.10 Variation of T_{base} and h_{av} with \dot{Q}_{evap} at different FS, $T_{sat} \cong 21.5^\circ\text{C}$, CP = 50%, RC = 64 g	106
Figure 4.11 Variation of COP and η_{II} with \dot{Q}_{evap} for different FS, CP = 50%, RC = 64 g	108
Figure 4.12 Variation of T_{base} with \dot{Q}_{evap} for different cases	109
Figure 4.13 Variation of h_{av} with \dot{Q}_{evap} for different cases	110
Figure 4.14 P-h diagram of the refrigeration cycle for this part	113
Figure 4.15 T-s diagram of the refrigeration cycle for this part	114
Figure 4.16 Comparison of Bertsch et al. [12] and experimental results of present study, Experimental conditions, [12], $P_{sat} = 550 \text{ kPa}$, $T_{sat} \cong 20^\circ\text{C}$, $G = 167 \text{ kg m}^{-2} \text{ s}^{-1}$. Experimental conditions of the present study, CP : 50%, RC : 64 g.	117
Figure 4.17 Comparison of the experimental [12] and theoretical [50] results, units $q''_{heated} : \text{W cm}^{-2}$, $G: \text{kg m}^{-2} \text{ s}^{-1}$, $D_h : \text{mm}$	119

LIST OF SYMBOLS AND ABBREVIATIONS

A	: area [m^2]
A_c	: cross sectional area [m^2]
A_w	: conduction heat transfer area [m^2]
b	: center to center distance of channel
Bo	: boiling number
C_r	: heat capacity ratio
Co	: convection number
D_h	: hydraulic diameter [m]
dz	: unit length [m]
f	:friction factor
F_{Fl}	: fluid to surface parameter
F_δ	: fin thickness [m]
F_h	: fin height [m]
F_p	: fin pitch [m]
Fr	: Froude number
G	: mass flux [$\text{kg m}^{-2} \text{s}^{-1}$]
h	: heat transfer coefficient [$\text{W m}^{-2} \text{K}^{-1}$]
H	: channel height of evaporator [μm]
H_c	: channel height for condenser (refrigerant side) [μm]
I	: current [A]
i	: enthalpy [kJ kg^{-1}]

j	: Colburn factor
k	: thermal conductivity [$\text{W m}^{-1} \text{K}^{-1}$]
l	: fin length, [m]
L	: length [m], heat exchanger length,
L_α	: louver angle [$^\circ$]
L_p	: louver pitch [m]
L_l	: louver length [m]
\dot{m}	: mass flow rate [kg s^{-1}]
n	: number of channels, fins or tube
NTU	: number of transfer units
Nu	: Nusselt number
N_S	: entropy generation number
p	: perimeter [m]
P	: pressure [Pa]
Po	: Poiseuille number
Pr	: Prandtl number
q''	: base heat flux [W m^{-2}]
q''_{heated}	: heat flux (based on heated area) [W m^{-2}]
\dot{Q}	: heat transferred [W]
R	: gas constant for air [$\text{J kg}^{-1} \text{K}^{-1}$]
Re	: Reynolds number
\dot{S}_{gen}	: entropy generation rate [W K^{-1}]
s	: specific entropy [$\text{kJ kg}^{-1} \text{K}^{-1}$]

t	: substrate thickness [μm], time [s]
T	: temperature [K]
T_0	: reference temperature
T_d	: tube depth [mm]
T_δ	: tube thickness [m]
T_p	: tube pitch [m]
u	: velocity [m s^{-1}]
U_o	: overall heat transfer coefficient [$\text{W m}^{-2} \text{K}^{-1}$]
V	: voltage [V]
W	: total width of evaporator
\dot{W}	: work power [W]
We	: Weber number
w_c	: microchannel width [m]
w_w	: microchannel wall thickness [m]
x	: vapor quality
v	: specific volume [$\text{m}^3 \text{kg}^{-1}$]
z	: stream-wise coordinate

Greek

α	: void fraction
α_c	: channel aspect ratio
ε	: effectiveness
η	: efficiency
η_o	: overall surface efficiency

η_{II}	: second law efficiency
μ	: dynamic viscosity [Pa s]
ϑ	: kinematic viscosity [$\text{m}^2 \text{s}^{-1}$]
σ	: surface tension [N m^{-1}]
σ'	: entropy gen. rate per length [$\text{W m}^{-1} \text{K}^{-1}$]
ρ	: density [kg m^{-3}]
ϕ_{lo}, ϕ_L	: two phase multiplier
χ	: Lockhart-Martinelli parameter
\dot{V}_a	: volumetric flow rate [$\text{m}^3 \text{h}^{-1}$]

Subscripts

a	: air
acc	: acceleration
base	: base
c	: cold side
CBD	: convective boiling dominant
cond	: condenser
comp	: compressor
cooling fans	: cooling fans
evap	: evaporator
F	: frictional
f	: frictional, fin
fin	: fin
g	: vapor phase

gen	: generation
go	: all vapor
H	: hot side
ht	: heat transfer
i	: inner
in	: inlet
l	: liquid
lg	: liquid-gas, latent heat
lo	: all liquid
Lp	: louver pitch
m	: mean
max	: maximum
min	: minimum
NBD	: nucleate boiling dominant
o	: outer, overall air surface
out	: outlet
pd	: pressure drop
post heater	: post heater
r	: refrigerant
real	: real fin length
rev	: reversible
sat	: saturation
sc	: subcooled
seg	: segment

sp	: superheated
tot	: total
tube	: tube
tp	: two-phase
lv	: liquid vapor
LO	: entire flow as liquid
w	: wall

ABBREVIATIONS

CP	: compressor power
COP	: Coefficient of performance
FS	: fan stage
RC	: refrigerant charge

CHAPTER 1

INTRODUCTION

1.1 Motivation

There has been increasing demand of heat dissipation from electronic components for nearly thirty years. Because of their decreasing sizes, dissipating heat from electronic components gets difficult day by day. At the same time, rapidly developing technology and increasing functionality of electronic components bring about more consumption of energy, this means higher necessity of heat removal from these devices. Therefore, classical air cooling and natural convection with extended surfaces, two primitive cooling methods, are not sufficient anymore. For this reason, new ways of cooling applications are sought. As a promising alternative, mini and micro refrigeration cycles have been implemented on electronic devices in recent years. Microchannels are thought to be a tool for removing high amount of heat from small volumes by Tuckerman and Pease, 1981 firstly [1]. They proved that high heat fluxes can be removed from the system in a limited space. Despite high pressure drop due to small hydraulic diameter and large temperature difference between the inlet and outlet, having high heat transfer coefficients and occupying small volumes, microchannels and micro systems offer a reasonable cooling. In the design and manufacturing of microchannels, optimization plays an important role. It is crucial that an engineering design should be made in the most efficient way to reduce the manufacturing and operational costs while meeting some design constraints. A microchannel should be designed in such a way that the pressure drop should be kept low, thermal performance should be maximized thereby thermal resistance is desired to be low. If a micro scale cooling system is considered, the COP of the cycle, and the second law efficiency should be maximized and dimensions of the system should be kept as small as possible.

After the study of Tuckerman and Pease [1], many other studies have been presented but most do not consider dimensional and thermal optimization of the micro components (microchannel heat sinks, heat exchanger, condenser etc.) of micro-scale systems.

Due to their high efficiencies, high heat removal rates and ability to operate reliably under different operating temperatures for a long time, miniature vapor compression refrigeration cycles (MVCRC) are considered as promising cooling options. These cycles are used for electronics cooling purposes mostly and also in protective clothing which serves as thermal resistance for human body in very hot environments [2]. In recent applications, as the cycle is generally used where the space is limited, its compactness is critical. In addition, the energy consumption becomes a challenge when these systems are to be mounted on mobile electronic devices. Although there has been some studies related to microscale vapor compression refrigeration systems, they do not consider any kind of optimization and suffer from deep theoretical background. In addition, the most critical components of MVCRC systems, namely the evaporator (heat sink) and condenser (heat exchanger) have not been examined in terms of detailed entropy generation analysis and minimization.

1.2 Scope of the Study

Using entropy generation analysis, it is aimed to design evaporator and condenser components of a MVCRC so that they will occupy less space, have high effectiveness (for condenser), low pressure drop throughout the channels and work with low surface temperatures (for evaporator). Entropy generation rate analysis gives us a chance to evaluate the component's performance under different working conditions. A mapping study has been conducted for some parameters like air mass flow rate, refrigerant mass flow rate, dimensions of the components (spacing of the fins, diameter of the channels etc.). In addition some of these parameters are optimized under specified working conditions.

The critical components, evaporator and condenser to be used in MVCRC are assessed individually. As the compressor characteristics varies for different working conditions and there is no reliable and enough data for characteristics of micro-compressor, evaporator and condenser analyses are performed individually. Their performance is

investigated under reasonable working conditions of a moderate MVCRC and they are designed such that they can be used in the constructed MVCRC.

1.2.1 Evaporator Design

The objective of the evaporator studies is to determine the entropy generation in the evaporator component of a MVCRC, and to dimensionally optimize the micro-evaporator section by minimizing the entropy generation rate. Copper microchannels of rectangular cross-section are considered, and R-134a is used as the refrigerant. The interval of the investigated parameters is constrained using the heat dissipation value of the contemporary processor Intel Core i7 [3]. Limitations on the mass flow rate are also determined based on the capacity of a micro compressor provided by Embraco Inc. that is being used in the experimental part of the study. Using two-phase models available in the literature, entropy generation rate is calculated. A mapping study is conducted to investigate the effects of mass flux, saturation temperature, channel dimensions, and heat flux on entropy generation rate. In addition, an optimization study is performed for obtaining micro-evaporator dimensions, and vapor qualities that yield minimum entropy generation rate. As the fluid properties vary due to the pressure drop in the flow direction, the computational domain is divided into segments for the accurate calculation of the entropy generation rate. Adiabatic fin tip approximation is employed to find the base temperature which is required when calculating the entropy generation rate due to heat transfer. The variation of heat transfer coefficient with vapor quality is also calculated and compares very well with available studies in the literature.

As a result of the present optimization study, the maximum temperature at the base and the pressure drop values occurring in the system are reduced. Hence, higher COP values can be expected from the optimized refrigeration cycles. Besides, the performance of the device to be cooled, e.g. an electronic chip will be improved as it is maintained at lower temperatures.

1.2.2 Condenser Design

An entropy generation number analysis of a microscale heat exchanger is believed to be useful for designing such a compact and thermally efficient device. It is aimed to design a heat exchanger which occupies small volume thanks to its high thermal performance, and to minimize the pressure drop for both air and refrigerant sides under various design and operating conditions (mass flow rates of air and refrigerant etc.).

Entropy generation number due to pressure drop and heat transfer is investigated according to refrigerant state in the heat exchanger: superheated, two phase, subcooled. The entropy generation number due to pressure drop on the air side becomes dominant after a certain air mass flow rate so there is a trade of between entropy generation number due pressure drop of air and heat transfer between the fluids. It is aimed to find the optimum dimensions and operating conditions yielding minimum entropy generation number in total for different sizes of the heat exchanger.

The present study offers an entropy generation number analysis for the micro-condenser component in an air cooled brazed aluminum parallel flow heat exchanger. The effects of various parameters, such as the fin pitch, fin height, channel width and height, refrigerant side fin (wall) thickness and air side mass flow rate have been investigated. Refrigerant R-134a is used as working fluid. The saturation temperature is considered approximately as 45°C and the condenser inlet temperature is 85°C at the same saturation pressure. The mass flow rate of the refrigerant is kept at 1.73 g s⁻¹. The saturation temperature and the mass flow rate are determined based on the data sheet of the micro compressor of Embraco Inc. brand which is built for similar operation. Calculations are performed for superheated, two phase and subcooled regions separately. Each region is divided into sufficiently many segments to consider the effect of changing thermophysical properties for obtaining realistic heat transfer coefficients. The segmentation procedure is important also in terms of the calculation of the entropy generation rate as the air outlet temperature, the density of the refrigerant, and the saturation temperature (due to pressure drop) differ for each segment. The entropy generation number terms are derived for pressure drop and heat transfer for both air and refrigerant sides.

To the best of the authors' knowledge, the study is the first in the literature in carrying out an entropy generation minimization study for two-phase flow in microchannel condensers.

1.2.3 Experimental Studies

An experimental set up has been constructed in a parallel study [4] based on the evaporator and condenser analyses of the present study as long as the manufacturing constraints permit. An oxygen free copper evaporator has been manufactured with

high aspect ratio channels ($700\text{ }\mu\text{m}\times 250\text{ }\mu\text{m}$). In addition, a compact condenser with $160\times 120\times 30\text{ mm}$ overall dimensions has been manufactured. The heat exchanger is air cooled and has triangular plain fin structure on the air side. Refrigerant flows in tubes through 25 parallel rectangular channels with $500\times 500\text{ }\mu\text{m}$ cross section dimensions. The schematic structure and photograph of the condenser are given in Figure 3.1 and Figure 4.6, respectively. Evaporator and condenser's performances are examined individually and cycle's performance is investigated as well. Experimental measurements and calculations are compared with theoretical calculations.

Evaporator's performance is evaluated in terms of heat transfer coefficient, base temperature and pressure drop. In addition, the length of the condenser used in the experiments is compared with theoretical calculation explained in Chapter 3.

The cycle performance is investigated in terms of COP, η_{II} and \dot{Q}_{evap} and they are compared with available studies in the literature. Effects of air mass flow rate, refrigerant, compressor power, refrigerant charge and saturation temperature on the mentioned parameters are sought.

1.3 Literature Survey

1.3.1 Microscale Vapor Compression Refrigeration Cycles

Designing a compact microscale vapor compression refrigeration cycle has been an attractive topic among the scientists for the last ten years (Yuan et al. [5]; Wu and Du [6]; Yu-Ting et al. [2]). The most recent study is conducted by Yuan et al. [5]. They designed a MVCRC with 260 W cooling load to provide cooling for one person with moderate working load when the ambient temperature is as high as 50°C . Under these conditions, they reached a COP of 1.62 and a reversible efficiency of 0.324. Although they do not specify the condenser heat load and changes depending on the operating conditions, the condenser heat load may reach the values about 476 W according to their COP and evaporator cooling load plots. They used a brazed aluminum parallel flow microchannel condenser as in the present study. Wu and Du [6] designed a similar system for electronics cooling purposes. They were able to remove 200 W heat from an electronic equipment and the total system dimensions were $300\times 230\times 70\text{ mm}^3$. The condenser heat load was stated as 260 W. The second law efficiency of the cycle was 31%. The authors stated that although the designed system was not small enough to be

mounted in a computer case, it can be installed next to the PC. Yu-Ting et al. [2] constructed a cycle using a second generation miniature Wankel compressor with 300 W cooling capacity. The coefficient of performance was determined to be 2.3 which corresponds approximately to a 430 W condenser load for the given cooling capacity. All of these three studies have focused on miniaturizing the size of the system while trying to increase the cooling capacity and COP of the system. However, detailed theoretical calculations have not been provided for the heat exchanger and the cycle design. The studies focused rather on the construction of the experimental setup and the evaluation of the cycle's performances based on data obtained. Although some correlations have been presented in the above-mentioned studies, no results have been reported based on these correlations. The present study offers the optimal brazed aluminum parallel flow heat exchanger geometry for various operating conditions by using an entropy generation minimization scheme. Basically, this study provides guidance for designing such a cycle. As a result of the presented second law analysis, the designed condenser is aimed to be the smallest possible thanks to its high thermal efficiency, to cause lower pressure drops, and ultimately, help increase the COP of the cycle. Trutassanawin et al. [7] have built a miniature cycle with R134a as the working fluid. They used DC variable rotary compressor and manually operated a needle valve for expansion valve. They have reached 268 W and a COP of 4.7 for maximum. Produced and experimented microscale vapor compression refrigeration cycles are summarized in Table 1.1.

Table 1.1 Miniature vapor compression refrigeration cycles, some data is obtained from [4]

Author	Q_{evap} (W)	T_{evap} (°C)	T_{cond} (°C)	Ref.	Compressor	Condenser	Evaporator $w_e \times H_e \times L$	Overall size of the system	Efficiency
Wu and Du [6]	100- 200	20	45	R134a	Aspen Inc. 14-24-000X Dia.58 mm, Height 78 mm 2858 rpm	0.55×0.70×100 mm $w_w = 0.26$ mm $n_{channel} = 18$ Overall Dim. 100×100×16 mm	0.5×4×57 Wall Th. 0.5 Channel No. 60 Overall Dim. 75×9×75 mm	300×230×70 mm Ref. charge 100 g	$\eta_{II} = 23\%$ to 31% COP 8.5
Yu-Ting, et al. [2]	300	21.6	40	R22	Dia.50 mm × 70 mm 1650 rpm Shaft power 95 W	1.2 mm×1.2 mm Overall Dim. 130×140×16 mm Fin Height 8 mm	Spiral-tube Dia.4 mm $w_w = 0.75$ mm $L = 550$ mm	260×250×120 mm (2.85 kg) Ref. Charge 100 g	COP 2.2
Trutassn avin et al. [7]	121-268	10 -20	40 - 60	R134a	Hitachi XL0623D1 Dia.85mm, Length 166 mm	Overall Dim. 45×180×25 mm Inlet air 25,27,35°C	Al 0.8×2.3 mm No. 41 Model CP20G01 mass flow meter)	100 g (Micro motion model D6S-SS mass flow meter)	COP 2.8-4.7
Mongia et al. [8]	-	50 (P= 6.85 bar)	90 (P=16. 4 bar)	isobutene	-	Inlet air 50°C	0.30 mm × 0.7 mm No.21	0.26 g s ⁻¹	COP > 2.25 25%-30%
Yuan et al. [5]	260			R134a	Miniature DC variable		48.3×27.3×21.1 mm	190×190×100	COP 2.3
Mancin et al. [9]	37-374	5-25	30-60	R134a	Oil free linear compressor prototype	Water cooled, not specified	L=4 mm.		COP 1.04-5.8
Present Study	<96	18-23	27-31	R134a	Oil free, Hermetic Linear	Air cooled aluminum brazed	700 $\mu\text{m} \times 250 \mu\text{m} \times$ 19 mm ($H_e \times w_e \times L$)		COP \leq 7.71

1.3.2 Evaporation Studies in Microchannels

Evaporation in microchannels has been a widely studied subject in the near past. Researchers inspected the pressure drop, heat transfer coefficient and flow characteristics for evaporation in microchannels. The dependence of heat transfer coefficient on local vapor quality and boiling regimes has been investigated extensively. Bertsch et al. [10] measured the local heat transfer coefficient for a wide range from subcooled liquid to superheated vapor for refrigerant R-134a in rectangular microchannels. The investigated channel width was 0.762 mm with 2.5 aspect ratio and 1.09 mm hydraulic diameter. Four different mass fluxes of 20.3, 40.5, 60.8 and 81 $\text{kg m}^{-2} \text{s}^{-1}$ have been inspected in a corresponding mass flow rate range of 0.5-2 g s^{-1} . The tests were conducted at three different saturation temperatures: 8.9°C, 18.7°C and 29°C. The wall heat flux range was from 0 to 20 W cm^{-2} . The maximum heat transfer coefficient was obtained for a vapor quality of 0.2 after which the heat transfer coefficient decreased sharply. It was concluded that the heat transfer coefficient strongly depended on the heat flux and the corresponding mass flow rate. It increased with increasing heat flux. It was also reported that saturation temperature had almost no effect on the heat transfer coefficient.

Lee and Mudawar [11] determined heat transfer coefficients for flow boiling of R134a in the range of 15.9-93.8 Wcm^{-2} heat flux and 0.26-0.87 vapor quality. Contrary to previous studies claiming that nucleate boiling or annular film evaporation was dominant in terms of heat transfer for channels with small diameters, Lee and Mudawar [11] classified heat transfer characteristics in three zones of low, medium and high qualities. At low heat fluxes, nucleate boiling ($x < 0.05$) occurs. On the other hand, at high heat fluxes, medium ($0.05 < x < 0.55$) or high ($x > 0.55$) quality flow take place and annular film evaporation becomes dominant. Because of distinctive heat transfer characteristics, it was advised to separate these regions based on their vapor qualities. As a result, a new correlation was offered which is claimed to estimate the heat transfer coefficient very well for R134a.

Some other experimental studies on microchannel evaporation are summarized in Table 1.2. Contrary to other experimental studies inspected in Table 1.2, Bertsch et al. [12], [10] worked on rectangular channels. Wang et al. [13] tested the largest diameter (6.5mm) channel among the examined studies and they used R22 as the refrigerant. Their channel material was copper. Yan and Lin [14] conducted experiments in multiple tubular channels using R134a. They modified their heat transfer coefficient calculations by taking into account the pressure drop effect on saturation pressure. They measured the pressure drop fluctuation to be under 5 kPa. Sumith et al. [15] is the only study which examined water flow. They used single stainless steel channels and noted that pressure fluctuation is under 4 kPa. Greco [16] examined various fluids for tubular channels for a wide range of mass flux $200\text{-}1100\text{ kg m}^{-2}\text{ s}^{-1}$. Tibirca and Ribatsky [17] conducted experiments for refrigerants R134a and R245fa in stainless steel channels. Distinctive aspect of Tibirca and Ribatsky [17]'s study is that they used a needle valve just before the test section in order to make the flow stable. Huo et al. [18] used calming section for the sake of stability as well.

Table 1.2 Microchannel evaporation studies in the literature

Author	Fluid	α Aspect ratio	G kg/m ² s ⁻¹	D _h mm	q''_{heated} kW m ⁻²	Material	n_{channels}
[12]	R134a, R245fa	Rec, 2.5	20-350	1.089 0.544	25-196	copper	17, 33
[10]	R134a	Rec, 2.5	20.3-81.0	1.089		copper	17
[19]	R113	Tube	30-300	2.92	8.8- 90.75	s. steel	1
[13]	R22	Tube	50-700	6.5	2.5-20	copper	1
[14]	R134a	Tube	50-200	2	5-20	not certain	28
[20]	HCFC123 and R11	Tube	50-1800	1.95	5-200	copper	1
[15]	Water	Tube	23.4- 152.7	1.45	10-715	s. steel	1
[18]	R134a	Tube	100-500	4.26, 2.01	13-150	s. steel	1
[21]	CO ₂ , R134a	Tube	240	6	10, 15, 2 0	s. steel	1
[16]	R134a, R22, R404a, R407c, R410a, R417a	Tube	200-1100	6	3.5-47	s. steel	1
[22]	R134a, R123	Tube	314, 392, 470	0.19	10, 15, 20	s. steel	1
[23]	R134a	Tube	310-860	1.3	21-50	s. steel	1
[17]	R134a, R245fa	Tube	50-700	2.3	5-55.0	s. steel	1
[24]	R134a	Tube	50-600	1.7	2-156	s. steel	1
[25]	R134a	Tube	240-930	2.6	10-100	s. steel	1
[26]	R22 and R134a	Tube	200-600	1.77, 3.36, 5.35	5.0-30	copper	1
[27]	R134a	Tube	200-500	1.1	20.8- 95.0	s. steel	1
[28]	R32	Tube	100, 200 and 400	2	6, 12 and 24	s. steel	1
[29]	R245fa	Tube		3	10-90	s. steel	1
[30]	R22, R134a, R410a, C ₃ H ₈ , CO ₂	Tube	300- 600/300- 600	3, 1.5, 0.5	20- 40/5-40	s. steel	1
[31]	R134a, R236fa and R245fa	Tube	200-1600	1.03	2.3-250	s. steel	1
[32]	R134a, R236fa and R245fa	Tube	200-500	1.03, 2.2, 3.04	10.0-30	s. steel	1
[33]	R134a, R1234	Tube	50-1500	1.0, 2.2	10-300	s. steel	1
Present study, Exp part	R134a	Rec, 2.8	140-190	0.37	≤ 7.77	copper	40

1.3.3 Condensation Studies in Microchannels

There are numerous studies about condensation in microchannels in the literature for various fluids. For brevity, the literature survey for condensation in microchannels are restricted to refrigerant R-134A and contemporary studies.

Su et al. [34] compared four experimental studies in the literature and a theoretical one. These four experimental studies used their own distinctive experimental data to form a heat transfer coefficient correlation for refrigerant R-134a. Based on these data, they have developed some correlations. Although they agree quite good in terms of heat transfer coefficients for various vapor qualities and mass fluxes, there are some discrepancies reaching up to 30%. However, the heat transfer coefficient trends are similar. In general, theoretical correlations showed better agreement with experimental ones for low heat transfer coefficients at high mass flux, and for higher heat transfer coefficients at low mass flux and high vapor quality values.

Al-Hajri et al. [35] have performed an extensive experimental study about thermal and hydrodynamic characteristics of refrigerant R134a and R245a during condensation for high aspect ratio microchannels. The channel cross sectional dimensions were 0.4 mm to 2.8 mm (corresponding to an aspect ratio of 7) and the length was 190 mm. The study examined the effects of saturation temperature between 30°C and 70°C, mass flux from 50 to 500 kg m⁻²s⁻¹) and inlet superheats between 0°C to 20°C. In the range of these parameters, average heat transfer coefficients and pressure drop characteristics are investigated and the results are compared with those obtained from the correlations available in the literature. As a result of the experiments, an increase in the saturation temperature resulted in a decrease in the heat transfer coefficient and pressure drop for both refrigerants. Not surprisingly, higher mass flux values yielded higher heat transfer coefficient and pressure drop. Inlet superheat temperature hardly affected the heat transfer phenomena but it had no effect on the pressure drop characteristics. R245fa performed 25% better than R134a in terms of heat transfer performance for a certain conditions. On the other hand, pressure drop value for R245fa was twice that of R134a for the same operating conditions.

Moser et al. [36] created a condensation model with a new equivalent Reynolds number. This Reynolds number is based on heat-momentum analogy. The created

condensation model is shown to predict experimental Nusselt number with an average deviation of 13.64% based on 1197 data points from 18 sources. Koyama et al. [37]'s results agree with Moser et al. [36]'s for high mass fluxes. Error is reported to be under $\pm 30\%$. Koyama et al. [37] conducted experiments with R134a for rectangular microchannels having diameters ranging from 0.8 to 1.1 mm. Moser et al. [36]'s two phase condensation correlation is applied in the present study. Contemporary experimental condensation studies related to present study are summarized in Table 1.3.

Table 1.3 Summary of microchannel condensation studies in the literature

Author	Fluid	α Aspect ratio	G kg/m ² s ⁻¹	D_h mm	L mm	T_{sat} °C	Measured parameter
[35]	R134a, R245fa	Rec, 7	50-500	0.7	190	30-70	PD, HTC
[37]	R134a	Rec, 0.7, 2	100-700	1.11, 0.8	600	60	PD, HTC
Present study, Experiments section.	R134a	Rec, 1	80-110	0.5	131	27-30	Cycle perf.

1.3.4 Entropy Generation Minimization

1.3.4.1 Entropy Generation Minimization in Evaporators

The entropy generation minimization method has always attracted researchers, especially when they are designing a heat exchanger. To some extent, the method is used for designing microchannel heat sinks. Almost all studies using entropy generation minimization method have focused on single phase, laminar and incompressible flow (Khan et al., [38]; Jafari et al., [39]). Khan et al. [38] carried out an optimization study for the overall performance of microchannel heat sinks employing entropy generation minimization method. Both thermal and hydrodynamic performances of the system are examined by the help of this method. Some general expressions were derived using mass, energy and entropy balances. In slip flow regime, important parameters, such as the channel aspect ratio, Knudsen number,

accommodation coefficient were evaluated for incompressible fluids. The authors concluded that the optimum entropy generation rate decreased with an increase in Knudsen number in the slip flow region. Similarly, Abbasi [40] inspected the entropy generation rate in a uniformly heated microchannel heat sink, and sought a solution for fluid flow with the porous medium model on extended Darcy equation. A 2-D model for the heat transfer was used in the study. The effects of the channel aspect ratio, thermal conductivity ratio and porosity on thermal and entropy generation rate characteristics of the flow are examined. Abbasi [40] reported that the ratio of the channel height to the channel width should be kept at the maximum in order to maximize the thermal performance. Contrary to majority of the studies dealing with optimization of rectangular microchannel heat sinks, Jafari et al. [39] optimized a circular microchannel geometry using entropy generation minimization method. Water was used as the coolant, and the effects of the channel diameter, number of channels, heat flux and pumping power on the entropy generation rate were investigated. They reported that the channel diameter has no significant effect for low heat flux values.

Although there is no dimensional optimization study other than the present one on microchannels using entropy generation minimization method for two-phase flow, there are some studies focusing on the entropy generation rate analysis in two-phase flow in mini or macro channels. Revellin and Bonjour [41] examined the entropy generation rate during flow boiling of refrigerant alone and refrigerant-oil mixture in a 10 mm diameter tube. Entropy generation rates are evaluated for smooth or enhanced tubes with varying tube diameters and mass flux (ratio of the mass flow rate to the flow cross sectional area) values for pure refrigerants or refrigerant-oil mixtures. The results indicated that the enhanced tube performed better in low mass velocities; on the other hand, smooth tubes are advised for higher mass velocities under uniform heat flux boundary condition at the tube wall. Sarkar et al. [42] carried out a study minimizing the irreversibility of heat exchangers for transcritical CO₂ systems for macro scale systems. They have conducted a second law analysis for both the evaporator and the gas cooler. The analysis comprised both operational and material related irreversibilities. The effects of the tube diameter, length, number of tube passes, the mass flow rate on heat exchanger performance were evaluated in the study.

1.3.4.2 Entropy Generation Minimization in Condensers

Entropy generation minimization studies available in the literature mainly concentrate on macroscale condensers. Sarkar et al. [42] carried out a study minimizing the irreversibility of heat exchangers for macroscale transcritical CO₂ systems. They conducted a second law analysis in a manner similar to the present study for both the evaporator and the gas cooler and examined operational and material based irreversibilities. The heat exchanger performance was evaluated as a function of tube diameter, length, number of tube passes, and the mass flow rate. Similarly, Saechan and Wongwises [43] searched optimal configuration for macroscale cross flow plate finned tube condenser using entropy generation rate analysis. The condenser had an aluminum plain fin geometry with air in crossflow. They investigated entropy production due to heat transfer and pressure drop in the air and refrigerant sides and also examined superheated, two phase and subcooled regions in terms of a dimensionless entropy generation number, N_s defined as the entropy generation rate divided by the minimum capacity rate. Their results showed that increasing the fin pitch and decreasing the number of rows and the tube diameter resulted in a lower entropy generation number. Pussoli et al. [44] used entropy generation minimization method for optimizing the peripheral finned-tube heat exchangers. They performed this optimization for fixed geometry, fixed face area and variable geometry.

Although many researchers have studied the entropy generation rate of heat exchangers of macro dimensions, there is a lack of heat exchanger design with entropy generation minimization method for condensing microchannel flow. The present study is unique in the literature in pursuing an entropy generation number mapping study for microscale two-phase flow air cooled heat exchangers.

1.4 Thesis Outline

The motivation and the scope of the present study as well as a detailed literature survey are provided in this first chapter. The optimized design of the microchannel evaporator is presented in Chapter 2. The micro-condenser design is detailed in Chapter 3. Experimental investigation of the designed micro-evaporator and micro-condenser components is given in Chapter 4. The experimental and theoretical results are also

compared in Chapter 4. Finally, Chapter 5 lists the summary and major conclusions of this dissertation.

CHAPTER 2

EVAPORATOR DESIGN

2.1 Problem Definition

The evaporator under investigation is essentially a rectangular microchannel heat sink. Pure copper is selected as the channel material due to its high thermal conductivity and ease of machining. The evaporator is planned for heat removal from electronic devices. As a reference contemporary device, Intel Core i7-900 processor is considered. The geometry of the evaporator is given in Figure 2.1. The cooling load and dimensions of the processor are summarized in Table 2.1.

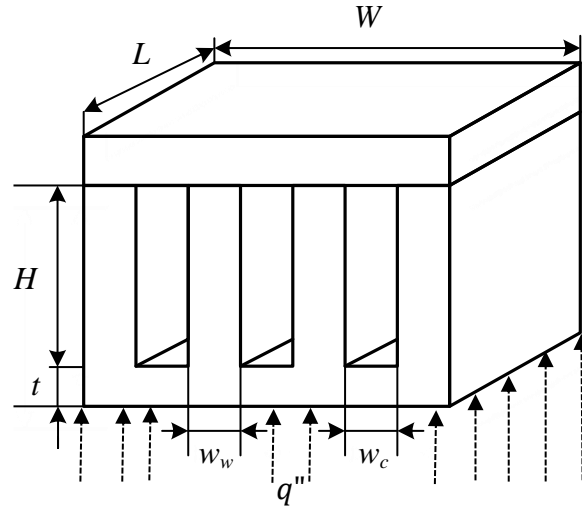


Figure 2.1 Evaporator geometry (Türkakar and Okutucu-Özyurt [45])

Table 2.1 Cooling load and main dimensions of Intel Core i7-900, [45].

Cooling load	130 W
Heat Flux (based on base area, $L \times W$)	47.74 W cm ⁻²
Length	1.891 cm
Width	1.44 cm

The following assumptions have been utilized for the calculations:

- Insulated top surface. Adiabatic fin tip.
- No contact resistance between the substrate (t) and the fins.
- Steady flow.
- Constant thermophysical properties of copper at 300 K.
- Uniform heat flux at the bottom surface and no contact resistance between the substrate and the electronic chip to be cooled.
- 1D heat transfer in the copper substrate (200 μm thickness)

In the evaporator design, the total channel length and the width are fixed parameters which are selected as the length and width of the processor, respectively. In addition to the cooling load of the reference processor, heat flux values of 40 and 55 Wcm⁻² are inspected as well. Unless stated otherwise, the saturation temperature inside the evaporator is chosen as 20°C as lower values may cause condensation on the evaporator surface. In all cases inspected for the entropy generation rates, the channel wall thickness (fin thickness) is kept constant at 250 μm , a value as thin as possible to ensure low entropy generation rates while maintaining the structural integrity.

The influence of a variety of parameters, such as the channel height, channel width, heat flux, mass flow rate, mass flux, outlet vapor quality, and saturation temperature on entropy generation rate have been inspected. The examined values of these parameters are stated in Table 2. The heat flux values given in

Table 2.2 are for the bottom surface area ($L \times W$, given in Table 2.1) of the system.

Table 2.2 Values of examined parameters

Heat Flux, W cm^{-2}	40, 47.74, 55
Mass Flow Rate, g s^{-1}	0.8-1.45
Inlet Vapor Quality	0.2
Outlet Vapor Quality (approximate)	0.7-0.92
Channel Height, μm	500, 600, 700
$T_{\text{sat}}, ^\circ\text{C}$	20
Substrate Thickness, $t, \mu\text{m}$	200

A T-s diagram for the evaporator is given in Figure 2.2

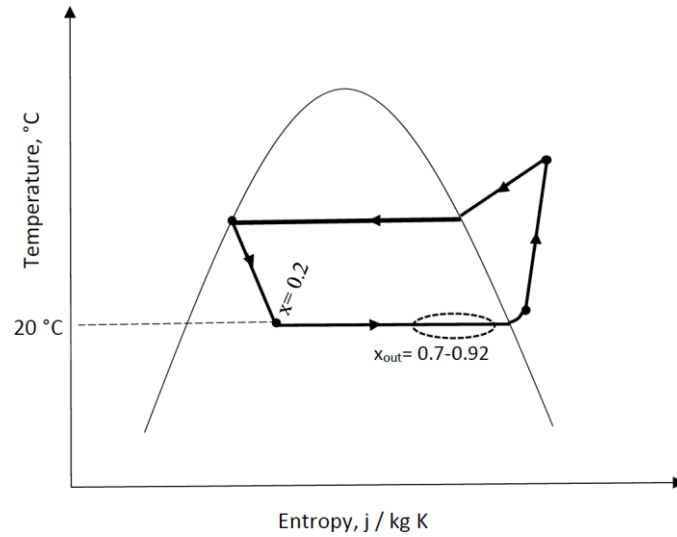


Figure 2.2 T-s diagram for the evaporator

2.2 Second Law Modeling

Although there are numerous entropy generation models for single phase and incompressible flow in the literature, only a few relevant studies exist on two-phase flow. Revellin and Bonjour [41] performed such a study on the second law analysis of two-phase flow through a circular tube of 10 mm diameter. They derived an entropy generation model for pure refrigerant and refrigerant oil mixture for minichannels.

Their aim was to compare the performances of enhanced and smooth tubes using local entropy generation modeling.

In the present work, the second law analysis has been applied to microchannel heat sinks using the control volume depicted in Figure 2.3. In Figure 2.3, the control volume shown on the left hand side is drawn at the beginning of the channel for better visualization; however, the control volume might be placed in any other location along the channel as shown on the right hand side.

In general, entropy generation for a control volume can be written as

$$\frac{dS}{dt} = \sum \dot{m} s_{in} - \sum \dot{m} s_{out} + \sum \frac{\dot{Q}}{T} + \dot{S}_{gen}. \quad (2.1)$$

Eq. (2.1) may be written in differential form for steady state flow for a small segment as (Revellin and Bonjour [41])

$$\sigma' dz = d(\dot{m}_g s_g + \dot{m}_l s_l) - \frac{q'' W dz}{T_{base}} \quad (2.2)$$

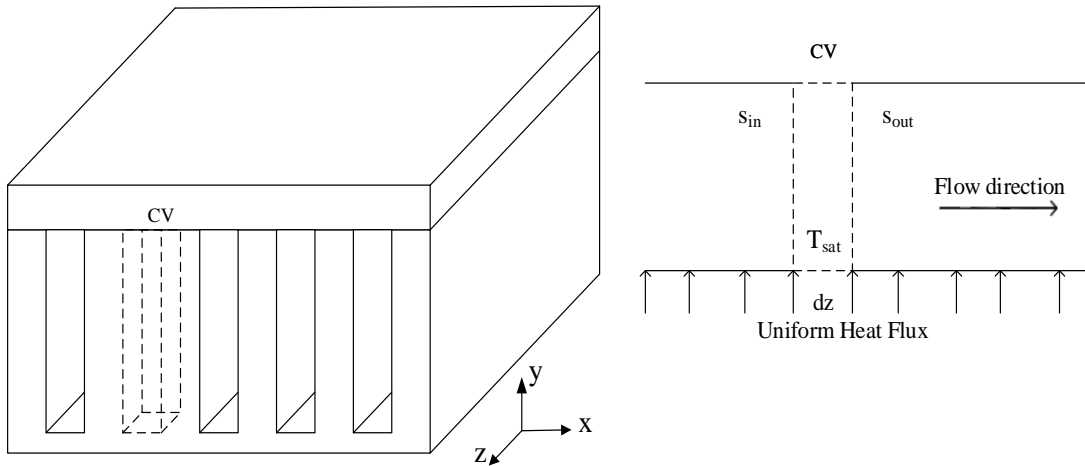


Figure 2.3 Microchannel heat sink and control volume (segment)

where σ' is the entropy generation per unit length, dz is the channel segment length, s represents the entropy with subscripts g and l standing for vapor and liquid phases,

respectively, $q'' W dz$ is the heat transferred to the control volume, T_{base} is the temperature of the bottom wall of the channel where heat transfer occurs between the wall and the fluid.

Eq. (2.2) may be written in terms of vapor quality, x as

$$\sigma' dz = \dot{m}_t d(x s_g + (1 - x) s_l) - \frac{q'' W dz}{T_{\text{base}}} \quad (2.3)$$

where $\dot{m}_t = \dot{m}_g + \dot{m}_l$ and $x = \frac{\dot{m}_g}{\dot{m}_t}$.

From the Gibbs relation,

$$di_g = T_g ds_g + v_g dp_g, \quad (2.4)$$

$$i_l = T_l ds_l + v_l dp_l. \quad (2.5)$$

Revellin and Bonjour [41] used the assumptions of $dp_g = dp_l$, $T_g = T_l = T_{\text{sat}}$ and they neglected the capillary contribution.

$$\sigma' dz = \frac{\dot{m}_t}{T_{\text{sat}}} d(x i_g + (1 - x) i_l) - \frac{\dot{m}_t dp}{T_{\text{sat}}} (x v_g + (1 - x) v_l) - \frac{q'' W dz}{T_{\text{base}}} \quad (2.6)$$

or in simplified form

$$\sigma' dz = \frac{\dot{m}_t}{T_{\text{sat}}} di_{\text{tp}} - \frac{\dot{m}_t v_{\text{tp}}}{T_{\text{sat}}} dp - \frac{q'' W dz}{T_{\text{base}}} \quad (2.7)$$

where

$$v_{\text{tp}} = x v_g + (1 - x) v_l \quad (2.8)$$

$$di_{tp} = x di_g + (1 - x) di_l + i_{lg} dx. \quad (2.9)$$

Substituting the cooling load per segment given in Eq. (2.10),

$$q'' W dz = \dot{m}_t di_{tp} \quad (2.10)$$

the final form of the entropy generation rate equation becomes

$$\sigma' dz = q'' W dz \left(\frac{T_{base} - T_{sat}}{T_{base} T_{sat}} \right) - \frac{\dot{m}_t v_{tp}}{T_{sat}} dp. \quad (2.11)$$

The first term on the right hand side of Eq. (2.11) is the entropy generation rate due to heat transfer and the second term is that due to the pressure drop.

2.3 Hydrodynamic Theory

There are two main pressure drop sources for two-phase flow in microchannels, namely, frictional and accelerational pressure drops (Kandlikar [46]). The total pressure drop is the summation of the two. The frictional pressure drop can be expressed as

$$\frac{dp_F}{dz} = \left(\frac{dp_F}{dz} \right)_L \phi_l^2 \quad (2.12)$$

where $\left(\frac{dp_F}{dz} \right)_L$ is the liquid phase frictional pressure gradient in the flow direction given by

$$\left(\frac{dp_F}{dz} \right)_L = \frac{2 f_l G^2 (1 - x)^2}{D_h \rho_l}. \quad (2.13)$$

Likewise, the vapor phase pressure drop may be obtained using

$$\left(\frac{dP_F}{dz}\right)_g = \frac{2 f_g G^2 x^2}{D_h \rho_g} . \quad (2.14)$$

In Eq. (2.13) and (2.14), f_l and f_g are the liquid and vapor phase friction factors. For laminar fully developed flow conditions. The Poiseuille number which is constant for fully developed flow conditions for certain geometries is equal to the multiplication of the Fanning friction factor and the Reynolds number [47]. Poiseuille number formulation dependent on aspect ratio is given by Kandlikar et al. [46].

$$\begin{aligned} Po &= f \times Re \\ &= 24 \times (1 - 1.3553 \alpha_c + 1.94677 \alpha_c^2 - 1.7012 \alpha_c^3 + 0.9564 \alpha_c^4 \\ &\quad - 0.2537 \alpha_c^5) \end{aligned} \quad (2.15)$$

where α_c is aspect ratio of the channel (longer side/short side). Poiseuille number is only dependent on the channel geometry for fully developed flow conditions [47].

For turbulent flow, $2000 \leq Re_g \leq 20000$, vapor phase fanning friction factor is given as

$$f_g = 0.079 Re_g^{-0.25} \quad (2.16)$$

In calculations, Eq (2.16) is used for fanning friction factor calculations for all cases. Results are observed and for the extreme case pressure drop increased 7% ($H=500\mu\text{m}$, $\dot{m} = 1.35 \text{ g s}^{-1}$) (Total entropy generation rate increased only 2.6%) if turbulent fanning friction factor is used for cases $2000 \leq Re_g$. As it is thought that entropy generation rate due to pressure drop is so small compared to heat transfer one and also mass flow rate is not too high, this change is negligible.

The two-phase pressure drop multiplier is defined as

$$\phi_l^2 = 1 + \left(\frac{C}{X}\right) + \left(\frac{1}{X^2}\right). \quad (2.17)$$

The Martinelli parameter, X , is the ratio of frictional pressure drop in liquid and vapor phases as given in Eq. (2.18).

$$X = \sqrt{\frac{\left(\frac{\Delta P}{L}\right)_l}{\left(\frac{\Delta P}{L}\right)_g}} \quad (2.18)$$

For the parameter C , Lee and Mudawar [48] proposed two different correlations for two different cases. If both liquid and vapor flow are laminar,

$$C = 2.16 (Re_{LO}^{0.047}) (We_{LO}^{0.6}) \quad (2.19)$$

and for laminar liquid and turbulent vapor (gas phase critical Reynolds number is taken as 2000, (Lockhart and Martinelli, [49])) flow conditions,

$$C = 1.45 (Re_{LO}^{0.25}) (We_{LO}^{0.23}). \quad (2.20)$$

In Eq. (2.19) and (2.20), Re_{LO} is the Reynolds number based on the liquid phase (entire flow as liquid). We_{LO} is the Weber number based on the liquid phase flow. In addition to the frictional pressure drop, accelerational pressure drop is also an important source of pressure drop in two-phase microchannel flow. Accelerational pressure drop per segment is given in (Kandlikar [46]) as,

$$\frac{dP_{\text{acc}}}{dz} = \frac{G^2 v_{\text{lg}} (x_2 - x_1)}{dz} \quad (2.21)$$

v is defined in Eq. (2.21) as specific volume of the refrigerant. Variables x_1 and x_2 in Eq. (2.21) are local vapor qualities. The total pressure drop is equal to the summation of frictional and acceleration pressure drops and given in Eq. (2.22).

$$\frac{dP_{\text{tot}}}{dz} = \frac{dp_{\text{F}}}{dz} + \frac{dP_{\text{acc}}}{dz} \quad (2.22)$$

2.4 Thermal Theory

Two-phase heat transfer coefficient is dependent on several parameters including but not limited to, the vapor quality, boiling number and convection number. Kandlikar and Balasubramanian [50] proposed the following correlations of heat transfer coefficient for two-phase flow in microchannels.

for $Re_1 > 100$

$$h_{\text{tp}} = \max \text{ of } (h_{\text{tp,NBD}}, h_{\text{tp,CBD}}), \quad \text{for } Re_{\text{LO}} > 100 \quad (2.23)$$

$$\begin{aligned} h_{\text{tp,NBD}} = & 0.6883 Co^{-0.2} (1-x)^{0.8} h_{\text{LO}} \\ & + 1058 Bo^{0.7} (1-x)^{0.8} F_{\text{Fl}} h_{\text{LO}} \end{aligned} \quad (2.24)$$

$$\begin{aligned} h_{\text{tp,CBD}} = & 1.136 Co^{-0.9} (1-x)^{0.8} h_{\text{LO}} \\ & + 667.2 Bo^{0.7} (1-x)^{0.8} F_{\text{Fl}} h_{\text{LO}} \end{aligned} \quad (2.25)$$

where Bo is the boiling number which is non-dimensional heat flux and is equal to $q''/(G i_{\text{lg}})$. The heat flux here is based on the heated area (three sides of the channel,

side surfaces and bottom). Co is the convection number (a modified Martinelli parameter) given as

$$Co = \left(\frac{1-x}{x} \right)^{0.8} \sqrt{\frac{\rho_g}{\rho_l}}. \quad (2.26)$$

For $Re_l < 100$, the use of $h_{tp,NBD}$ Eq. (2.24) is advised (Kandlikar [46]).

h_{LO} is the single phase, all liquid, heat transfer coefficient, and is provided for various ranges of Re_{LO} in (Kandlikar, [46]). F_{Fl} is the fluid surface parameter, and is given as 1.63 for R-134A/copper surface interface (Kandlikar [46]).

for $100 \leq Re_{LO} \leq 1600$

$$h_{LO} = \frac{Nu_{LO} k}{D_h} \quad (2.27)$$

for $3000 \leq Re_{LO} \leq 10^4$

$$h_{LO} = \frac{(Re_{LO} - 1000) Pr_L \left(\frac{f}{2} \right) \left(\frac{k_l}{D_h} \right)}{1 + 12.7 \left(Pr_l^{\frac{2}{3}} - 1 \right) \left(\frac{f}{2} \right)^{0.5}} \quad (2.28)$$

for $10^4 \leq Re_{LO} \leq 5 \times 10^6$

$$h_{LO} = \frac{Re_{LO} Pr_l \left(\frac{f}{2} \right) \left(\frac{k_l}{D_h} \right)}{1 + 12.7 \left(Pr_l^{\frac{2}{3}} - 1 \right) \left(\frac{f}{2} \right)^{0.5}} \quad (2.29)$$

For the transition region where $1600 < Re_{LO} < 3000$, a linear interpolation is advised [46].

2.5 Fin Model

The fin performance is crucial in microchannel heat sinks, and is affected by parameters, such as the fin length, shape and material, and the base temperature.

In most applications, the top surface of a microchannel heat sink is covered with an insulation material to confine the rejected heat within the heat sink. The studies aiming to observe flow patterns preferred glass as the top surface material that is bonded to the fin material. For this reason, adiabatic fin tip model is employed in the present study.

The heat transferred to the fluid may be calculated using

$$\begin{aligned}\dot{Q}_{\text{seg}} &= q'' W dz \\ &= n h_{\text{tp}} dz (2 \eta_{\text{fin}} H + w_c) (T_{\text{base}} - T_{\text{sat}})\end{aligned}\quad (2.30)$$

where n represents the number of channels, dz is the segment length, H is the channel height (fin length) and w_c is the channel width. Using adiabatic fin tip model, T_{base} is calculated by taking top surface as adiabatic.

For fins of uniform cross section, and adiabatic tip, the fin efficiency is derived to be

$$\eta_{\text{fin}} = \frac{\tanh(m H)}{m H} \quad (2.31)$$

where m is defined as

$$m = \left(\frac{h p}{k_{\text{fin}} A_c} \right)^{\frac{1}{2}} = \left(\frac{2 h}{k_{\text{fin}} w_w} \right)^{\frac{1}{2}}. \quad (2.32)$$

Under uniform heat flux, \dot{Q}_{seg} is known, and the only unknown remains as the base temperature, T_{base} which is an important parameter affecting entropy generation rate.

2.6 Solution Methodology and Code Validation

Employing the described entropy generation rate, pressure drop and thermal models, a simple but effective solution methodology has been developed. As evaporation in microchannels shows different characteristics depending on the vapor quality, heat flux, mass flow rate and saturation temperature, the computational domain has been divided into small segments. This way, calculations are not affected by the change of thermophysical properties and diverse evaporation characteristics. In the present study, the computational domain has been divided into forty eight small segments of the same lengths in the direction of the channel length. A grid independence test has been performed and taking forty eight and ninety six segments yielded less than 1% difference in the entropy generation rate.

The computational algorithm starts with evaluating the thermophysical properties of refrigerant R-134a corresponding to the saturation temperature, pressure and inlet vapor quality. Next, the main parameters and dimensions are entered. The calculation process (for a specific combination of the mass flow rate, the channel width and the fin thickness) basically involves taking the inlet properties from the exit of the previous segments. As the segment length, the heat flux and the mass flow rate are known, the outlet vapor quality of a given segment can be calculated using the first law of thermodynamics. Then, the hydrodynamic and thermal calculations are carried to obtain results for the segment in consideration. The base temperature and the pressure drop are then determined. Subsequently, a second law analysis is carried out, and the entropy generation rate for this segment is calculated and recorded. As the pressure drop is known, the inlet temperature of the next segment and all other required variables are known. The thermophysical properties in a given segment are averaged using the values at the segment inlet and the outlet. As the computational domain is divided into 48 regions, this assumption is quite reasonable. The calculations are repeated for the remaining segments and the total entropy generation rate is obtained.

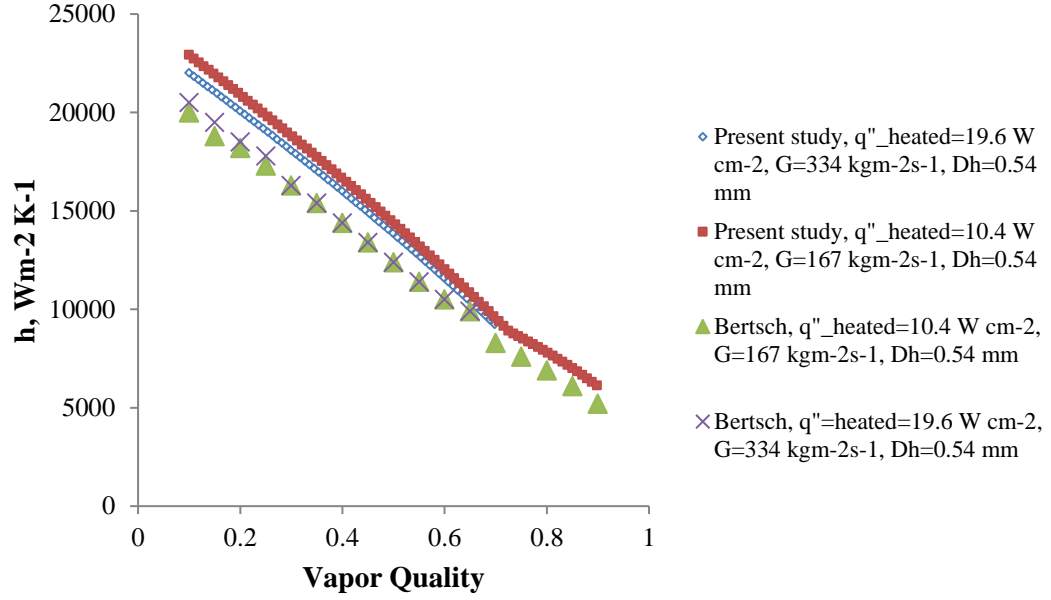


Figure 2.4 Comparison of the variation of heat transfer coefficient with vapor quality as obtained by Bertsch et al. [12] and by the present study. Red-green and blue-purple markers correspond to the same conditions.

For the validation of the code written in Matlab R2011b, the variation of the heat transfer coefficient with the local vapor quality has been computed, and a comparison has been made with the study of Bertsch et al. [12] using the correlations provided in (Kandlikar and Balasubramanian [50]) for the same conditions ($P_{\text{sat}} = 550 \text{ kPa}$). The results are plotted in Figure 2.4.

Bertsch et al. [12] formed this plot to compare their experimental results with widely used correlations. In both plots, the same conditions and dimensions have been used. In the present study, the evaluation of thermophysical properties accounted for the pressure drop. On the other hand, in (Bertsch et al. [12]), the properties were taken as constant at 20°C (Refprop). The code in present study is integrated with the self-developed code using data of ASHRAE 1997, and the slight deviation for low vapor qualities is believed to be due to this difference in property evaluation.

In addition to the thermal validation, the hydrodynamic part of the code has also been validated. Mahmoud et al. [51] compared experimental correlations in the literature

with their experiments about flow boiling pressure drop of R134a in a microdiameter tube, and noticed remarkable deviation among them. As an extreme deviation, 264% mean absolute error has been obtained for a specific case and correlation. Asadi et al. [52] reviewed the literature for heat transfer and pressure drop characteristics of two-phase flow in microchannels, and provided a comparison of experimental studies. Among the reported studies, those of Qu and Mudawar [53], and Lee and Mudawar [48] seemed suitable for comparisons with the present work.

Lee and Mudawar [48] suggested a new correlation for the two phase pressure drop multiplier of separated flow model which included the effects of liquid viscosity and surface tension. 5.62% mean absolute error was obtained between the results of their model and experiments with R134a taking 87 data points. The authors conducted the experiments at the mass velocity range of $G = 127\text{-}654 \text{ kg m}^{-2} \text{ s}^{-1}$, inlet quality range of 0.001-0.25, outlet quality of 0.49-superheat and the heat flux range of $31.6\text{-}93.8 \text{ Wcm}^{-2}$.

The authors interpreted the pressure drop components for different cases using their modified dimensionless parameter, C . The two phase pressure drop multiplier in Eq. (15) has been calculated using this parameter. However, the separated flow model used in their calculations has not been specified. Lee and Mudawar's [48] frictional and accelerational pressure drop formulae are presented in Eqs. (2.33),(2.34) and (2.35), respectively.

$$\frac{dP_F}{dz} = \frac{1}{x_{\text{out}}} \int_0^{x_{\text{out}}} \frac{2 f_l G^2 (1-x) v_l}{D_h} \phi_l^2 dx \quad (2.33)$$

$$\Delta P_{\text{acc}} = G^2 \left\{ \left[\frac{v_g x_{\text{out}}^2}{\alpha_{\text{out}}} + \frac{v_l (1-x_{\text{out}})^2}{(1-\alpha_{\text{out}})} \right] - \left[\frac{v_g x_{\text{in}}^2}{\alpha_{\text{in}}} + \frac{v_l (1-x_{\text{in}})^2}{(1-\alpha_{\text{in}})} \right] \right\} \quad (2.34)$$

with void fraction, α

$$\alpha = \left[1 + \left(\frac{1-x}{x} \right) \left(\frac{v_l}{v_g} \right)^{\frac{2}{3}} \right]^{-1} \quad (2.35)$$

In Qu and Mudawar [53] on the other hand, Eq. (2.21) has been used to calculate the accelerational pressure drop. The frictional pressure drop in their study is given by

$$\frac{dP_F}{dz} = \frac{1}{x_{\text{out}}} \int_0^{x_{\text{out}}} \frac{2 f_l G^2 (1-x)^2 v_l}{D_h} \phi_l^2 dx. \quad (2.36)$$

In the present study, instead of the integral form of the frictional pressure drop given by Eqs. (2.33) or (2.36), the flow system has been divided into differential segments and the vapor quality has been evaluated as the arithmetic average of segment inlet and outlet pressures.

In Figure 2.5, the variation of the total pressure drop with the heat flux obtained by Lee and Mudawar [48], Qu and Mudawar [53] and the present study are compared. As may be observed from the figure, there is excellent agreement between the results of the present study and that of Qu and Mudawar [53]. The agreement between the results of Lee and Mudawar [48] and those of the present study are also very good at low heat fluxes, and the maximum deviation is less than only 1 kPa at the highest heat flux value.

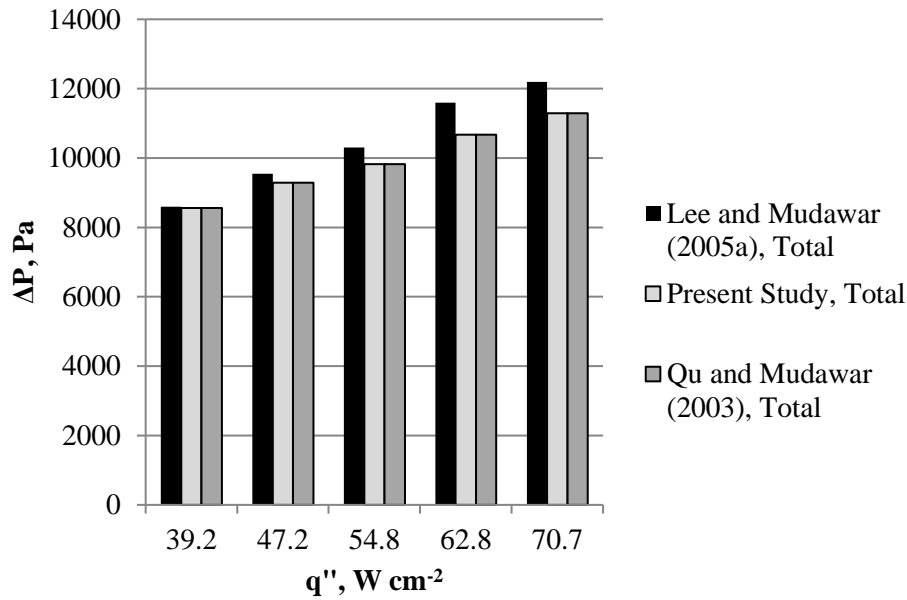


Figure 2.5 Comparison of the total pressure drop values of the present study, and those available in the literature (Lee and Mudawar [48], Qu and Mudawar [53]), $G = 415 \text{ kg m}^{-2} \text{ s}^{-1}$

The frictional and acceleration pressure drop components have been calculated and compared as well. The results are presented in Figure 2.6. Since a range, rather than exact values, for the saturation temperature, and inlet or outlet vapor qualities are provided in the reference study, the calculations have been performed at a saturation temperature of 10°C and an approximate inlet quality of 0.15 which are in the given range of parameters provided by Lee and Mudawar [48].

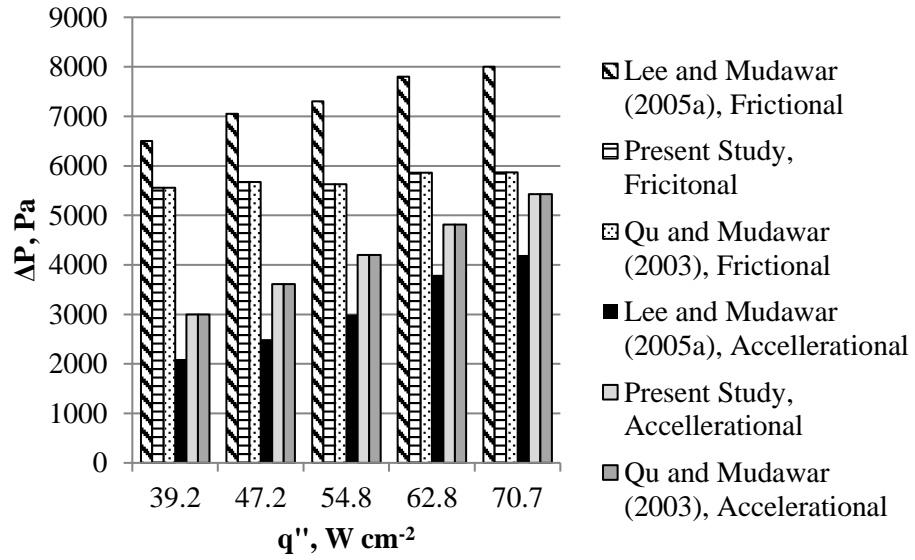


Figure 2.6 Comparison of the pressure drop components of the present study and those available in the literature (Lee and Mudawar [48], Qu and Mudawar [53]), $G = 415\ kg\ m^{-2}\ s^{-1}$

It should be noted that the accelerational pressure drop correlation used in the present study is different than that used by Lee and Mudawar [48]. As illustrated in Figure 2.6, both frictional and accelerational pressure drop values of the present study perfectly match with those provided by Qu and Mudawar [53]. The accelerational pressure drop component of the present study is higher than that of Lee and Mudawar [48], however the general trend is similar.

It should be noted that as the mass velocities are low in the present study, the accelerational pressure drop is a minor component. Hence, the difference between the results does not cause a mentionable error. On the other hand, the frictional pressure drop component in the present study seems to be stable against the variation of heat flux, and it underestimates the results obtained by Lee and Mudawar [48]. The difference might stem from the unspecified parameters and the separated flow model used in Lee and Mudawar's [48] study. When the total pressure is inspected, the variation between the two models is very little, under 8%, even for the extreme case (Figure 2.5).

Before closing the discussion on the code validation, it is worth mentioning that as the entropy generation rate due to pressure drop is low compared to that due to heat transfer, the deviation in the pressure drop between the present study and that of Lee and Mudawar [48] does not lead to a major concern.

2.7 Optimization Study

Entropy generation minimization is commonly used in thermal design as an optimization technique lately. The use of this technique is quite new and is limited to single phase and incompressible flow among microchannel studies. Hence, the use of entropy generation minimization method in dimensional optimization of microchannel heat sinks in two-phase flow is a new approach, and is being utilized for the first time in the literature by the present study.

Previously, the authors have conducted an optimization study minimizing the thermal resistance for the dimensional optimization of a microchannel heat sink in single phase, incompressible flow (Türkakar and Okutucu-Özyurt [45]). A similar methodology is applied in the present study to find the optimum heat sink dimensions minimizing the entropy generation rate for two-phase flow this time. In other words, the objective function in the present study is the entropy generation rate.

The objective function has two design variables: the channel width and the fin thickness. Although the mass flow rate is not stated as a design variable, the optimization has been conducted for a wide range of mass flow rates. The fixed parameters of the design are

- the total channel width, W
- the substrate thickness, t
- the cooling load, Q
- the evaporator inlet temperature and pressure,
- the evaporator inlet vapor quality, x_{in} .

The values of these fixed parameters have been stated before in Table 2.1 and Table 2.2. In the optimization part of the study, the heat flux is considered constant at 47.74 W cm^{-2} , the value corresponding to Intel Core i7 processor.

Table 2.3 Interval of design variables and grid numbers

Height, μm	Upper bound		Lower bound		Grid
	w_c	w_w	w_c	w_w	
500	300	200	50	50	251×151
600	300	200	50	50	251×151
700	300	200	50	50	251×151

The interval of design variables determined based on manufacturing constraints are stated in Table 2.3. The minimum channel width is specified as $50 \mu\text{m}$, which may be produced in a copper block using wire-cut electro discharge machining (EDM). According to the entropy generation rate analyses, thinner fins produced less entropy. Hence, the minimum fin thickness is also determined to be $50 \mu\text{m}$. Even thinner fins ($46 \mu\text{m}$) are produced and experimented for silicon microchannels in the literature (Costa-Patry et al. [54]). There is no manufacturing limitation for the maximum channel widths and fin thicknesses. The upper bounds stated in Table 2.3 seem to be adequate when looked at optimization results because optimum dimensions are much lower than the upper limits. The desired channel heights can be produced with wire-cut EDM. Three different channel heights are examined in the present study.

2.7.1 Optimization Methodology

Entropy generation rates are evaluated analytically following the procedure outlined in section 2.2 for each combination of w_c and w_w in the interval of design variables. Grid search is utilized in finding the combination that yields minimum entropy generation rate. The interval of design variables is divided into grids, and at the

intersection of these grids, the entropy generation rate is calculated. As a result, an entropy generation rate matrix is generated. This matrix includes entropy generation rates for all combinations of w_c and w_w specified in the design interval, Table 2.3. In order to determine the optimum combination, the smallest entropy generation rate in this matrix is searched for. The optimum w_c and w_w combination yielding the minimum entropy generation rate is then recorded. The dimensions of the entropy generation rate matrix might be adjusted by the user. In the present study, the resolution is chosen such that, for each micrometer value in the interval of design variables, w_c and w_w , the entropy generation rate is calculated. As a check, decreasing the resolution by one order of magnitude ($0.1 \mu\text{m}$) did not cause a worthy change in the results, hence, it has been decided that a $1 \mu\text{m}$ grid interval was adequate. Besides, $1 \mu\text{m}$ is surely within the tolerance limits of metal based, or even MEMS based fabrication techniques. The number of grids and the interval of design variables are listed in Table 2.3.

The entropy generation rate calculations in the computational domain for specified values of w_c and w_w has been explained in Section 2.6. Integrating the optimization part the computational algorithm may be schematically given in Figure 2.7.

If the computational algorithm is to be summarized, it starts with evaluating the thermophysical properties of R-134a according to the saturation temperature, pressure and the inlet vapor quality. At the same time, the code reads the main parameters and dimensions. Then, for a particular combination of the channel width and fin thickness, under constant mass flow rate, the hydrodynamic and thermal calculations are performed segment by segment and results are recoded in the optimization (entropy generation rate) matrix. The calculation procedure to find the entropy generation rate for just one element (specific combination of channel width and fin thickness) is discussed in detail in Section 2.6. After forming the optimization matrix, the combination yielding the minimum entropy generation rate and optimum dimensions is found.

It should be noted that the optimization procedure and speed may be improved using a meta-heuristic optimization algorithm such as tabu search, however, for a single objective function with only two design variables, grid search performs sufficiently well (Okutucu and Türkakar [55]).

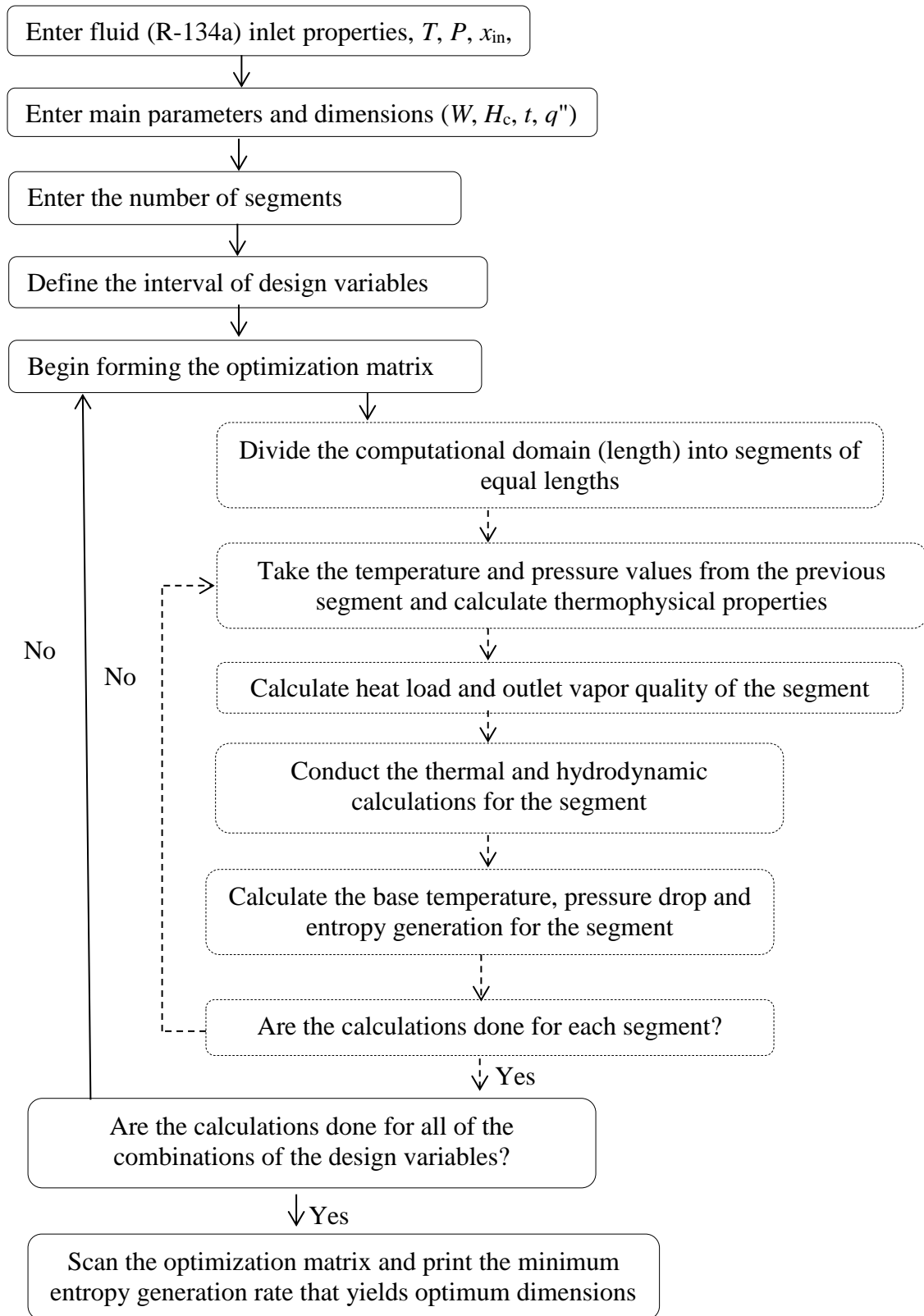


Figure 2.7 Computational algorithm for evaporator design calculations.

2.8 Evaporator Results

2.8.1 Entropy Generation Rate Analysis

In evaporator design entropy generation rate has an important role. A low entropy generation rate indicates effective heat transfer and low pressure loss. With this motivation, the effects of various parameters on entropy generation rate have been investigated. These parameters are mainly, the channel height, heat flux, channel width, mass flow rate, mass flux, outlet vapor quality and the saturation temperature.

Figure 2.8 shows the variation of entropy generation rate with the mass flow rate for various heat and mass flux values. Three combinations of heat and mass fluxes are selected such that the vapor quality varies from 0.72 to 0.95 approximately for each data series. For a constant mass flux, the mass flow rate varies as the channel width changes from 200 to 400 μm with 10 μm increments. That is, each data corresponds to a particular w_c (channel width) which is proportional to the mass flow rate. On the other hand, the channel wall thickness is the same for all cases, 250 μm . Working with low heat fluxes and mass flow rates seems to be reasonable as entropy generation rate level is low. Otherwise, thermal and hydrodynamic performance will be poor for higher mass flow rates and heat fluxes.

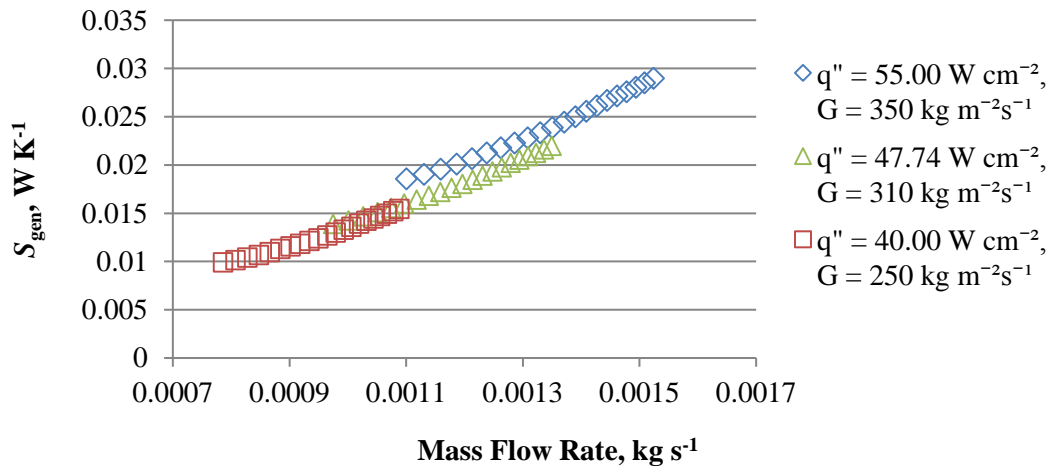


Figure 2.8 Effect of mass flow rate on entropy generation rate for various heat and mass fluxes, $H = 500 \mu\text{m}$, $T_{\text{sat}} = 20^\circ\text{C}$, $w_w = 250 \mu\text{m}$, $x_{\text{out}} \cong 0.72\text{-}0.95$, $w_c = 200\text{:}10\text{:}400 \mu\text{m}$.

It can be observed from Figure 2.8 that under constant mass flux, an increase in the channel width, hence mass flow rate, results in increase in the entropy generation rate. Then, the use of narrower channels is favorable under constant mass flux conditions. In addition, it is observed that higher heat fluxes resulted in higher entropy generation rates. Although increased mass flow rates are used for higher heat fluxes, the entropy generation rate, therefore, the temperature at the base is also higher.

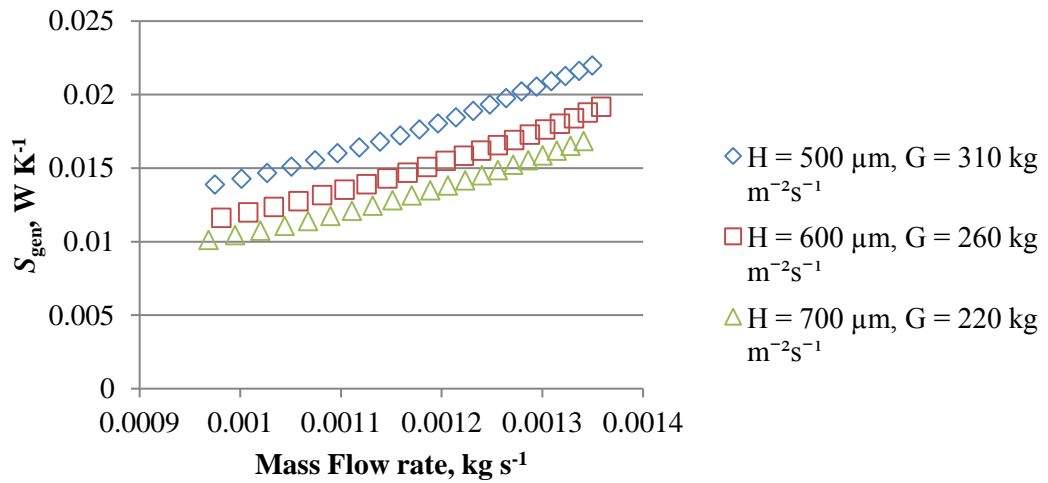


Figure 2.9 Effect of mass flow rate on entropy generation rate for various mass flux and channel height values, $q'' = 47.74 \text{ W cm}^{-2}$, $T_{\text{sat}} = 20^\circ\text{C}$, $w_w = 250 \text{ μm}$, $x_{\text{out}} \cong 0.72$ - 0.93 , $w_c = 200:10:400 \text{ μm}$.

Figure 2.9 is plotted to examine the effect of channel height on entropy generation rate. Similar trends to those in Figure 2.8 can be observed regarding the effects of mass flux. Additionally, smaller channel heights produced higher entropy values. This behavior is basically attributed to the heat transfer area. In the case of 500 μm channel height, the heated area, the two side walls and the bottom wall, is the smallest among the three cases, in other words, the heat flux (based on heated area) value is the highest. This causes higher channel wall temperatures and results in higher entropy generation rates in the control volume.

In Figure 2.10 and Figure 2.11, the channel width and the wall thickness are kept constant, and the effects of the heat flux and the channel height, respectively, on

entropy generation rate are examined by varying the mass flow rate. These figures give an insight into proper outlet vapor qualities in evaporator design. This is an important matter because after a critical local vapor quality, the local heat transfer coefficient decreases sharply which may result in burn out of the electronic equipment to be cooled as the temperature of the base reaches the limits of safe operation.

The discussion made on the effects of heat flux on entropy generation rate for Figure 2.8 and Figure 2.9 are also valid for Figure 2.10. Although there is not a considerable variation in the entropy production with the mass flow rate, careful inspection indicates that it decreases first and then increases slightly.

The outlet vapor qualities yielding the minimum entropy generation rates for heat fluxes of 55, 47.74 and 40 W cm⁻² are found to be 0.856, 0.846 and 0.828, respectively. The results are expected as the local heat transfer coefficient decreases sharply after the outlet vapor quality of 0.85 at which the base temperature rises to critical values. Similarly, outlet vapor qualities providing the lowest entropy generation rates for channel heights of 700, 600 and 500 μm are 0.878, 0.847 and 0.847, respectively.

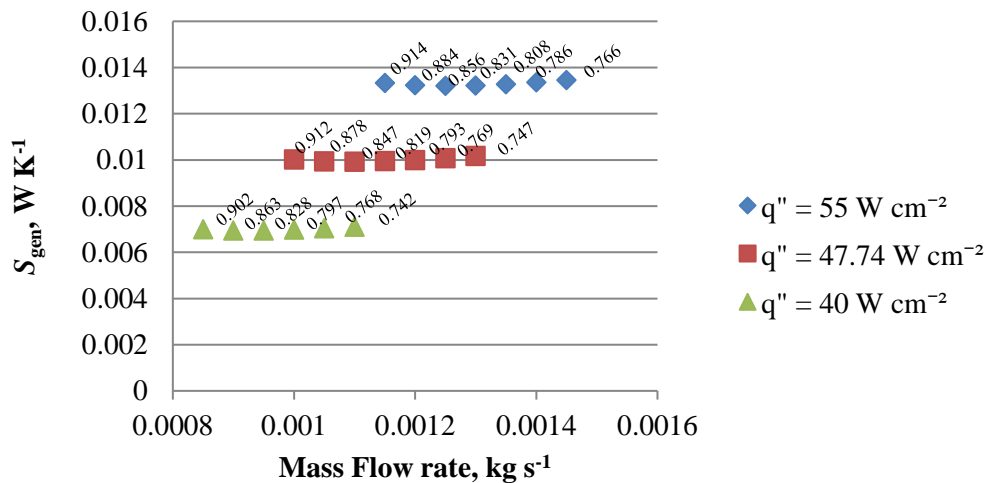


Figure 2.10 Effect of mass flow rate on entropy generation rate at constant channel width and wall thickness for various heat flux values, $H = 700 \mu\text{m}$, $T_{\text{sat}} = 20^\circ\text{C}$, $w_c = 200$, $w_w = 250 \mu\text{m}$, $x_{\text{out}} \cong 0.74\text{-}0.91$.

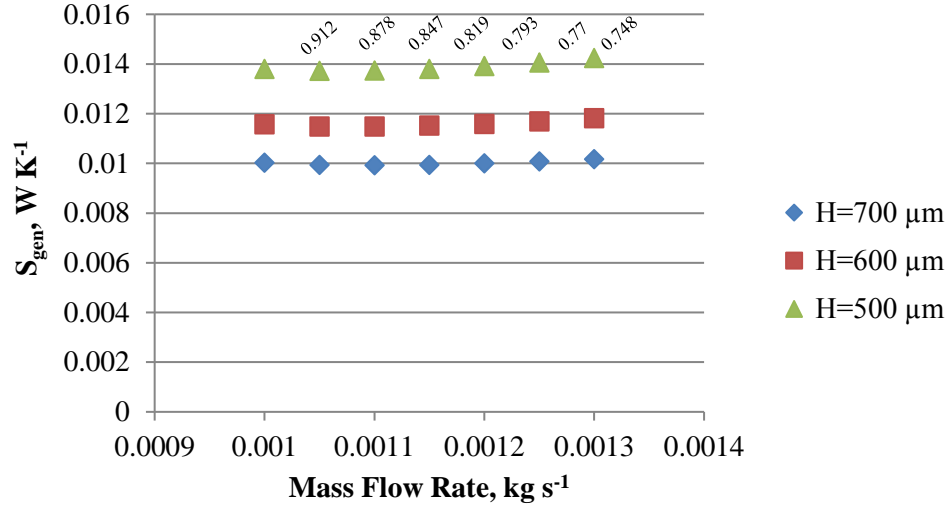


Figure 2.11 Effect of mass flow rate on entropy generation rate at constant channel width and wall thickness for various channel height values, $q'' = 47.74 \text{ W cm}^{-2}$, $T_{sat} = 20^\circ\text{C}$, $w_c = 200 \text{ μm}$, $w_w = 250 \text{ μm}$, $x_{out} \cong 0.74\text{-}0.91$.

In Figure 2.12, the mass flow rate is kept constant for all data series to fix the outlet vapor quality at 0.9. While the channel wall thickness is kept at 250 μm, the channel width varied from 400 to 200 μm with 10 μm intervals for two successive data sets. As mass flow rate is constant for each data series while the channel width was changing, the mass flux also varied. In Figure 2.12, the effect of heat flux on entropy generation rate for different channel widths, hence mass fluxes, is observed.

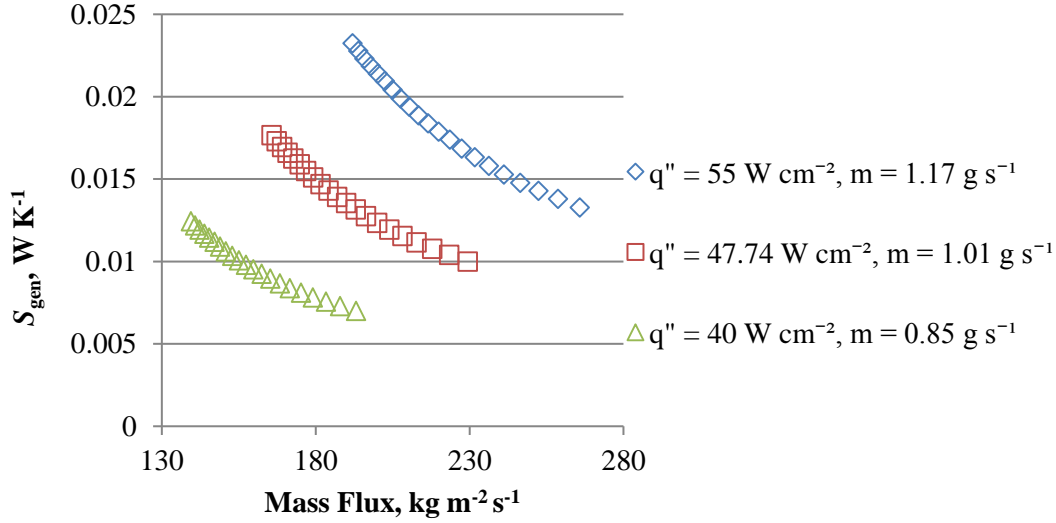


Figure 2.12 Effect of mass flux on entropy generation rate for various heat fluxes, and flow rates, $H = 700 \mu\text{m}$, $T_{\text{sat}} = 20^\circ\text{C}$, $w_c = 400:10:200 \mu\text{m}$, $w_w = 250 \mu\text{m}$, $x_{\text{out}} \cong 0.90$

For each data series in Figure 2.12, higher entropy generation rates correspond to greater channel widths as it was in previous figures. Hence, it can be concluded that independent from the conditions of constant mass flow rate or mass flux, the entropy generation rate tends to decrease for decreasing channel widths. The effect of heat flux on entropy generation rate is similar for the case of constant mass flux. It can also be inferred from Figure 2.12 that, at the same vapor outlet quality, higher heat fluxes produce more entropy. The variation of entropy generation rate with mass flux for a variety of channel heights has also been inspected and similar results, not shown here for brevity, to those in Figure 2.11 have been obtained.

The saturation temperature is another important parameter in evaporator design as the channel surface and fluid temperature difference affects the convective heat transfer. In Figure 2.13, four different saturation temperatures are inspected.

As can be seen from Figure 2.13, although entropy generation rates deviate slightly for the examined range of mass fluxes, the saturation temperature does not seem to have a substantial effect on entropy generation rate. This result is in agreement with the

conclusion of Bertsch et al. [10] stating that the saturation temperature has almost no effect on heat transfer coefficient. Besides, variation in the thermophysical properties did not cause any significant change in the entropy generation rate. In the figure, the mass flow rates are equal for all cases, however, as the latent heat for different saturation temperatures are different, the outlet vapor qualities are different.

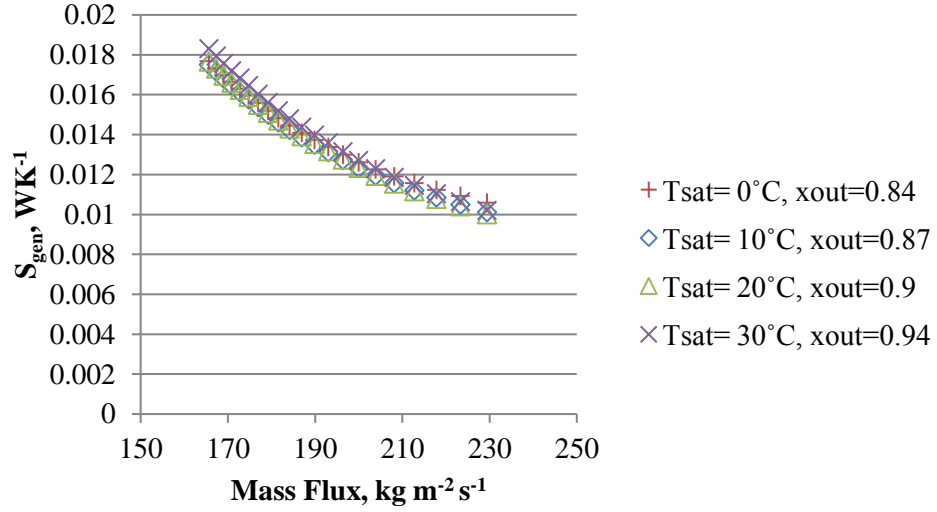


Figure 2.13 Variation of entropy generation rate with mass flux for various saturation temperatures, $\dot{m} = 1.01 \text{ g s}^{-1}$, $H = 700 \text{ }\mu\text{m}$, $q'' = 47.74 \text{ W cm}^{-2}$, $w_c = 400:10:200 \text{ }\mu\text{m}$, $w_w = 250 \text{ }\mu\text{m}$, x_{out} : varies.

Finally, when the contributions of heat transfer and pressure drop on entropy generation rate are analyzed, it has been observed that the entropy generation rate is dominantly due to heat transfer, and the effect of pressure drop is almost negligible. As an example, among the cases for 1.1 g s^{-1} mass flow rate, the entropy generation rate due to heat transfer is approximately at least twenty one times higher than that due to pressure drop for 47.74 W cm^{-2} heat flux and $600 \text{ }\mu\text{m}$ channel height.

2.8.2 Optimization Results

Optimum channel width and wall thickness combinations have been obtained for a mass flow rate range of $0.95\text{-}1.35 \text{ g s}^{-1}$ which is determined based on the capacity of a

micro compressors provided by Embraco Inc. that is being used in the experimental part of the study. The results are provided in Table 2.4-Table 2.6, for channel heights of 500, 600 and 700 μm , respectively.

Table 2.4 Optimization Results for $H = 500 \mu\text{m}$, $q'' = 47.74 \text{ W cm}^{-2}$

Mass flow rate, g s^{-1}	S_{gen} , W K^{-1}	Optimum w_c , μm	Optimum w_w , μm	$S_{\text{gen,ht}}$	$S_{\text{gen,pd}}$	x_{out}	T_{max} , $^{\circ}\text{C}$	Pressure drop, Pa
0.95	0.0034547	63	50	0.00227	0.00118	0.95	21.5	10043
1	0.0036105	66	50	0.00237	0.00124	0.91	21.5	9986
1.05	0.0037764	70	50	0.00252	0.00126	0.88	21.6	9668
1.1	0.0039552	73	50	0.00263	0.00132	0.85	21.7	9682
1.15	0.0041347	74	50	0.00268	0.00145	0.82	21.6	10168
1.2	0.0043238	79	50	0.00288	0.00144	0.79	21.8	9670
1.25	0.0045118	80	50	0.00294	0.00157	0.77	21.8	10121
1.3	0.0047080	81	50	0.00300	0.00171	0.75	21.8	10570
1.35	0.0049116	82	50	0.00306	0.00185	0.73	21.8	11016

Table 2.5 Optimization Results for $H = 600 \mu\text{m}$, $q'' = 47.74 \text{ W cm}^{-2}$

Mass flow rate, g s^{-1}	S_{gen} , W K^{-1}	Optimum w_c , μm	Optimum w_w , μm	$S_{\text{gen,ht}}$	$S_{\text{gen,pd}}$	x_{out}	T_{max} , $^{\circ}\text{C}$	Pressure drop, Pa
0.95	0.0029496	64	50	0.00211	0.00084	0.95	21.5	7112
1	0.0030544	65	50	0.00214	0.00092	0.91	21.4	7395
1.05	0.0031690	67	50	0.00220	0.00097	0.88	21.4	7429
1.1	0.0032889	69	50	0.00227	0.00102	0.85	21.4	7460
1.15	0.0034131	71	50	0.00235	0.00107	0.82	21.5	7490
1.2	0.0035449	71	50	0.00236	0.00118	0.79	21.4	7967
1.25	0.0036915	72	50	0.00241	0.00128	0.77	21.4	8284
1.3	0.0038440	75	50	0.00252	0.00132	0.75	21.5	8209
1.35	0.0040002	76	50	0.00257	0.00143	0.73	21.5	8528

Optimization results revealed that except for a few cases belonging to 700 μm channel height, the optimum fin thickness is equal to the minimum limit, 50 μm . This way the number of channels for a fixed total width may be increased for increased heat transfer

area, and the channel width, which influences the pressure drop for a fixed channel height, may be adjusted to a value that is wide enough to reduce the pressure drop, and narrow enough to increase the heat sink area for enhanced heat transfer. It should be noted that the pressure drop in two-phase flow is lower compared to that in single phase liquid flow. As indicated in Table 2.4, Table 2.5 and Table 2.6, the pressure drop value is only around 6 kPa, hence, the entropy generation rate due to pressure drop is lower than that due to heat transfer. It may be observed that the entropy generation rate due to pressure drop is less than half of that due to heat transfer for most of the cases. Thus, heat transfer dominates the optimization characteristics. Having relatively low pressure drop values, the optimization code tends to yield lower the channel widths. If the pressure drop values were higher, the code would reduce the pressure drop by widening the channels. The use of minimum fin thickness reduced the maximum temperature in the substrate and entropy generation rate due to heat transfer. The optimum fin thickness is slightly greater than the lower bound for $H = 700 \mu\text{m}$ and $\dot{m} = 0.95, 1$ and 1.05 g s^{-1} . In these cases, the pressure drop is not a major concern as the channels are sufficiently tall, and the mass flow rate is low. The maximum temperature in the heat sink is evaluated based on the maximum base temperature in the microchannel using the conductive resistance of the copper substrate ($t = 200 \mu\text{m}$). The maximum temperatures in the substrate are calculated to be far below the critical values of operation. As the inlet saturation temperature is 20°C , the thermal performance of the heat sink is as desired.

The variation of entropy generation rate with the channel width and fin thickness in the design interval is given as a 3D plot in Figure 2.14. It is illustrated in Figure 2.14 that away from the optimum dimensions, the entropy generation rate increases. Variations at H and \dot{m} combinations other than those used for plotting Figure 2.14 show similar characteristics.

Table 2.6 Optimization Results for $H = 700 \mu\text{m}$, $q'' = 47.74 \text{ W cm}^{-2}$

Mass flow rate, g s^{-1}	S_{gen} , W K^{-1}	Optimum w_c , μm	Optimum w_w , μm	$S_{\text{gen,ht}}$	$S_{\text{gen,pd}}$	x_{out}	T_{max} , $^{\circ}\text{C}$	Pressure drop, Pa
0.95	0.0028644	71	61	0.00226	0.00060	0.95	21.8	5121
1	0.0028437	73	53	0.00226	0.00058	0.91	21.7	4700
1.05	0.0028472	68	51	0.00211	0.00074	0.88	21.4	5689
1.1	0.0029198	66	50	0.00205	0.00087	0.85	21.3	6377
1.15	0.0030252	67	50	0.00209	0.00093	0.82	21.3	6565
1.2	0.0031334	69	50	0.00216	0.00097	0.79	21.3	6541
1.25	0.0032419	72	50	0.00226	0.00098	0.77	21.4	6331
1.3	0.0033525	74	50	0.00234	0.00102	0.75	21.4	6320
1.35	0.0034652	76	50	0.00241	0.00105	0.73	21.5	6312

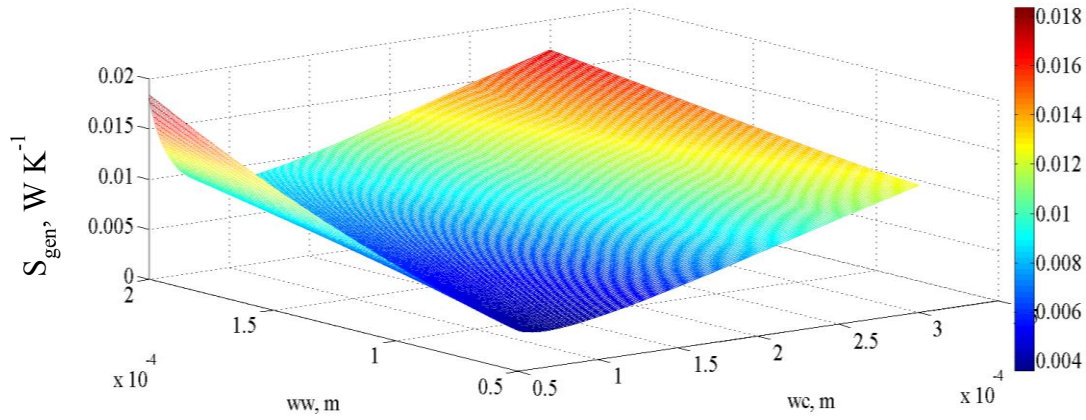


Figure 2.14 Contour plot of entropy generation rate for $H = 500 \mu\text{m}$, $\dot{m} = 1 \text{ g s}^{-1}$, $q'' = 47.74 \text{ W cm}^{-2}$.

In Figure 2.15, the optimized conditions given in Table 2.4, Table 2.5 and Table 2.6 are expressed in terms of entropy generation rate due to heat transfer and pressure drop separately. The heat transfer sourced entropy generation rates are approximately three or four times higher than the pressure drop sourced ones. In the entropy generation rate analysis part of the study (Section 2.8.1), the contribution of heat transfer was substantially greater compared to that of the pressure drop as the investigated channel widths were in the range of 200-400 μm . On the other hand, in the optimization part (Section 2.8.2), the optimum channel widths are found to be much smaller than the mentioned range. The optimization results reveal that narrower channels considerably

increased the pressure drop based entropy generation rate and it should be accounted for in the total entropy production.

The variation of entropy generation rate with respect to mass flow rate (from 0.92 to 1.35 g s⁻¹ with 0.01 g s⁻¹ increments) has been investigated in Section 2.8.1 for greater channel and fin widths. After the optimization, the same analysis has been performed for 70 µm channel width and 50 µm fin width which are approximate optimum dimensions for the considered cases. The main goal of the repeated analysis is to have an idea about the optimum outlet vapor quality. While increasing the mass flow rate resulted in slight increase in the entropy generation rate for 500 and 600 µm channel heights, first a slight decrease and then an increase is observed for 700 and 800 µm tall channels. In fact, a slight decrease in the entropy generation rate due to heat transfer is observed for low mass flow rates for all channel heights (Figure 2.16), however, the entropy generation rate due pressure drop turns out to be effective with increasing mass flow rate. Thereby, the lowest total entropy generation rate corresponds to the minimum mass flow rate for 500 and 600 µm channel heights. The optimum vapor qualities corresponding to the minimum entropy generation rates are 0.878 and 0.803 for 700 and 800 µm channel heights, respectively. The optimum vapor qualities are found as 0.878 for both 900 and 1000 µm channel heights which are not depicted in Figure 2.16.

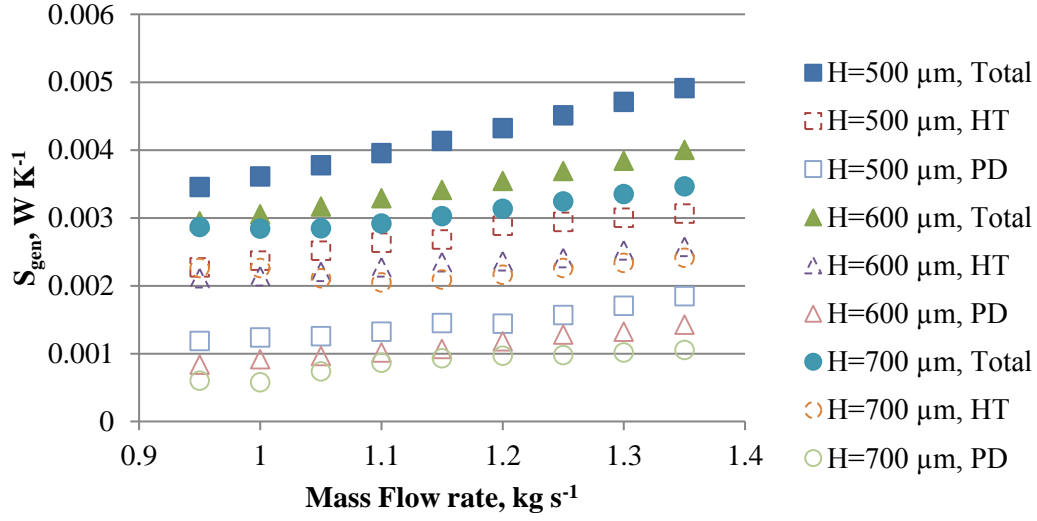


Figure 2.15 Contribution of heat transfer (HT) and pressure drop (PD) to the entropy generation rate of the optimized channels

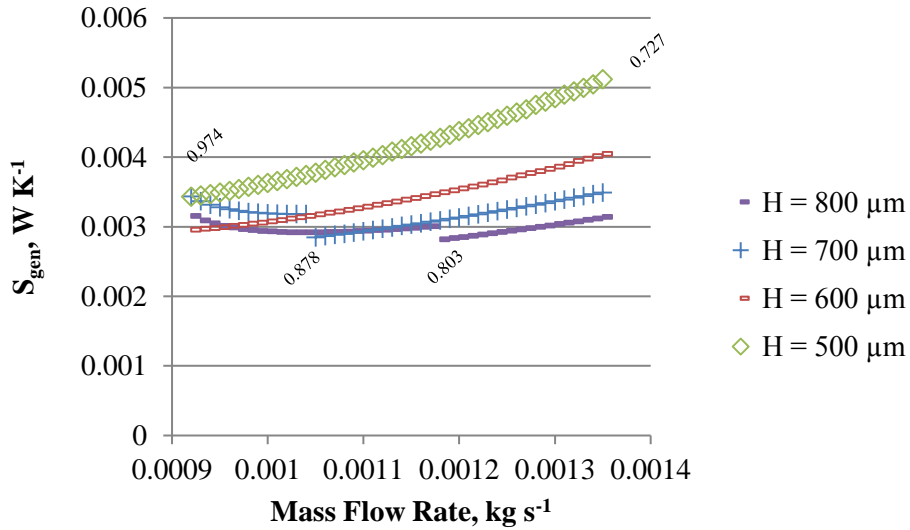


Figure 2.16 Effect of mass flow rate on entropy generation rate at constant channel width and wall thickness for various channel height values, $q'' = 47.74 \text{ W cm}^{-2}$, $T_{\text{sat}} = 20^\circ\text{C}$, $w_c = 70 \text{ μm}$, $w_w = 50 \text{ μm}$, $x_{\text{out}} \cong 0.727\text{-}0.974$.

The entropy generation minimization study presented in this chapter can be used to optimize the dimensions and vapor qualities for a micro-evaporator so that the best hydrodynamic and thermal performance could be yielded.

CHAPTER 3

CONDENSER DESIGN

3.1 Problem Definition

For the condenser type, an air cooled brazed aluminum parallel flow heat exchanger is considered. The fins are multilouvered. The refrigerant side is also considered as aluminum with rectangular microchannels. The refrigerant side microchannels and the air fins are usually assembled together with a brazing process. The refrigerant (R-134a) flows through three tube series and makes three passes as shown in Figure 3.1. The fixed parameters in the entropy generation rate analysis are provided in Table 3.1. The condenser design is unique in literature as it carries out an entropy generation minimization for two phase flow in a microchannel condenser.

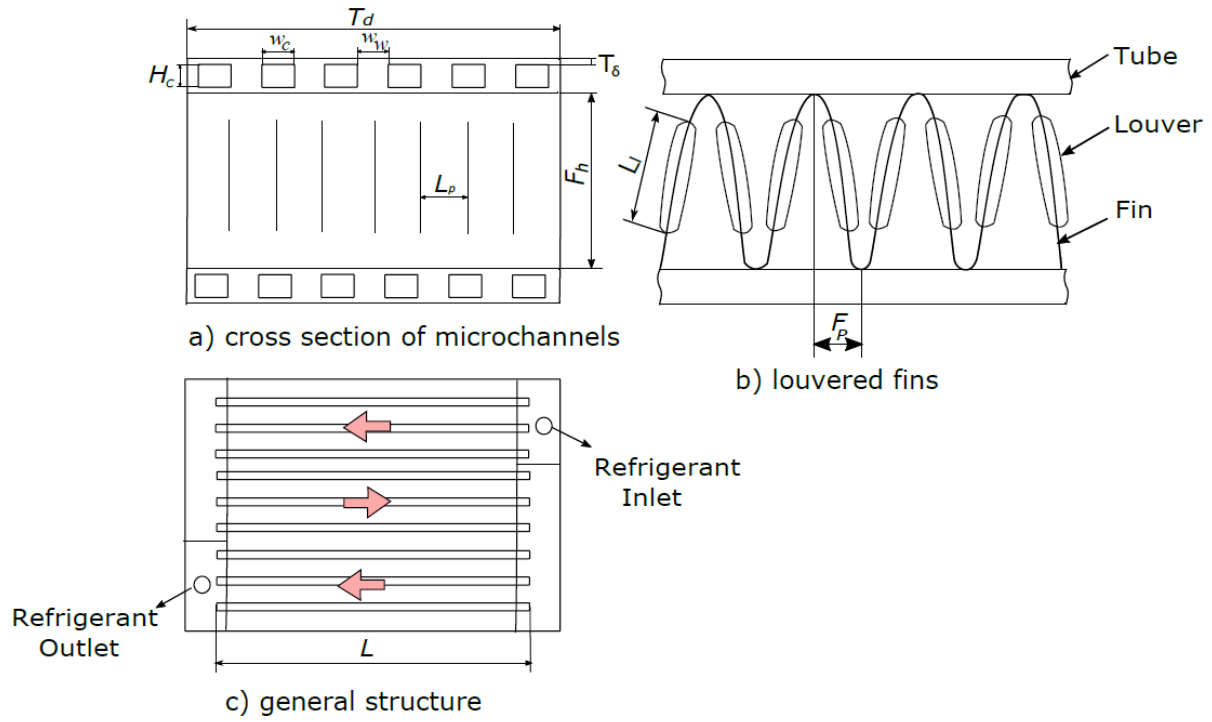


Figure 3.1 Air cooled aluminum condenser geometry [56]

Table 3.1 Fixed parameters of the condenser

\dot{m}_r	$1.73611 \times 10^{-3} \text{ kg s}^{-1}$
\dot{Q}_{tot}	$\cong 354 \text{ W}$
\dot{Q}_{sp}	$\cong 76.7 \text{ W}$
\dot{Q}_{tp}	$\cong 276 \text{ W}$
\dot{Q}_{sc}	$\cong 1.5 \text{ W}$
$P_{r,\text{in}}$	$\cong 1.16 \cdot 10^6 \text{ Pa}$
$T_{r,\text{in}}$	85°C
$T_{r,\text{sat}}$	$\cong 45^\circ\text{C}$
$T_{a,\text{in}}$	300 K
n_{tube}	3
n_{pass}	3
$L_{\text{seg,sp}}$	0.5 mm
$L_{\text{seg,tp}}$	5 mm

The subcooled region cooling load is around 1.5 W. This is determined based on the inlet state of the evaporator. The exit enthalpy of the condenser is equal to evaporator inlet enthalpy. The vapor quality at the evaporator inlet is chosen as 0.2 at 20°C evaporator saturation temperature as heat transfer coefficient is higher at lower vapor qualities (Türkakar and Okutucu-Özyurt [3]). Refrigerant mass flow rate is chosen according to Embraco Inc's data sheet at 20°C evaporating and 45°C condensing temperature. Compressor's power consumption is reported to be 72.2 W at that temperature and superheating temperature is given as 35°C in the evaporator. Inlet state of the condenser is determined according to this information. Although it is known that not all of the consumed power is transferred to the fluid, condenser load is desired to be kept at maximum. The segment lengths for each region are given in Table 3.1. These lengths should not be confused with the heat exchanger length. After the calculation of the total length of the segments, this length is divided into three to determine the heat exchanger length (given as L in the plots) as the heat exchanger tubes make three passes as shown in Figure 3.1, b.

Table 3.2 Fixed dimensions of the condenser

Tube depth, T_d	16 mm
Fin thickness, F_δ	0.1 mm
* Fin height, F_h	8 mm
* Fin pitch, F_p	1.3 mm
* Louver angle, L_α	29°
Louver pitch, L_p	0.1 mm
Louver length, L_l	5.4 mm
Tube wall thickness, T_δ	2 mm
Tube pitch, T_p	12.5 mm
* Microchannel height, H_c	0.5 mm
* Microchannel width, w_c	0.5 mm
Microchannel wall thickness, w_w	0.5 mm

* Marked parameter's fixed values are used in the calculations unless otherwise specified in figure captions. Unmarked parameters are fixed for all cases.

The fixed dimensions of the condenser are given in Table 3.2. These dimensions are used throughout the calculations unless otherwise specified. In the second law analyses, some dimensions such as the fin pitch, fin height and the louver angle are varied within the range given in Table 3.3.

Table 3.3 Ranges of examined parameters

F_p	1.0-1.6 mm
F_h	7-10 mm
\dot{m}_a	0.025-0.13 kg s ⁻¹
L_α	20-35°
D_h	300-800 μ m

A T-s diagram is given in Figure 3.2,

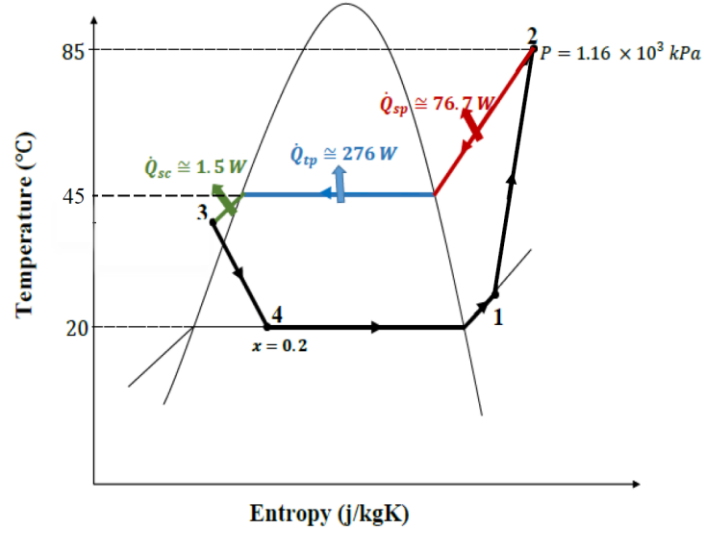


Figure 3.2 T-s diagram for the condenser

3.2 Second Law Modeling

In the present work, a second law analysis has been applied to a single segment of the heat exchanger using the control volume depicted in Figure 3.3. Sarkar et al. [42] developed a similar model for minimizing the irreversibility of heat exchangers for transcritical CO₂ systems for macroscale systems and made the calculations segment by segment as in the present study.

In general, entropy generation rate for a control volume can be written as

$$\frac{dS}{dt} = \sum \dot{m} s_{in} - \sum \dot{m} s_{out} + \sum \frac{\dot{Q}}{T} + \dot{S}_{gen}. \quad (3.1)$$

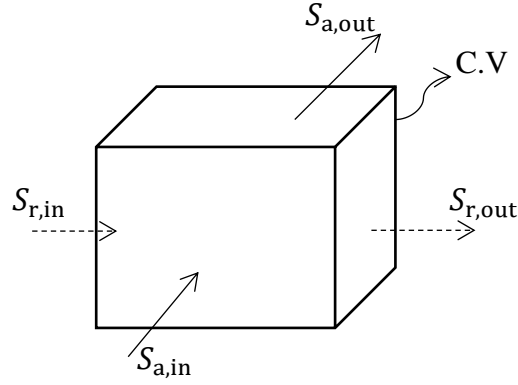


Figure 3.3 Control volume for a segment of the heat exchanger

In the derivation of the entropy generation rate formulas, the following assumptions are made:

- Kinetic and potential energy changes are neglected;
- Constant properties averaged between the inlet and the outlet (for each segment);
- No heat transfer between the heat exchanger and the environment (on top, bottom and side surfaces);
- No axial conduction through the solid parts of the heat exchanger (In the segment drawn, there is a little amount of heat conduction to/from the neighbour segments which could be neglected as the temperature difference is also low);
- Uniform air flow, with air being considered as an ideal gas.

The total entropy generation rate may be expressed for steady state conditions as

$$\dot{S}_{\text{gen,tot}} = \sum_{\text{segment}} [\dot{m}_a(s_{a,\text{out}} - s_{a,\text{in}}) + \dot{m}_r(s_{r,\text{out}} - s_{r,\text{in}})] \quad (3.2)$$

The air can be assumed as an ideal gas and its entropy change assuming constant specific heats can be substituted as,

$$\dot{S}_{\text{gen,a}} = \dot{m}_a(s_{a,\text{out}} - s_{a,\text{in}}) = \dot{m}_a \left[c_{p,a} \ln \left(\frac{T_{a,\text{out}}}{T_{a,\text{in}}} \right) - R \ln \left(\frac{P_{a,\text{out}}}{P_{a,\text{in}}} \right) \right]. \quad (3.3)$$

Hence, the total entropy generation rate may be given as

$$\begin{aligned} \dot{S}_{\text{gen,tot}} = \sum_{\text{segment}} \left[\dot{m}_a \left(c_{p,a} \ln \left(\frac{T_{a,\text{out}}}{T_{a,\text{in}}} \right) - R \ln \left(\frac{P_{a,\text{out}}}{P_{a,\text{in}}} \right) \right) \right. \\ \left. + \dot{m}_r(s_{r,\text{out}} - s_{r,\text{in}}) \right] \end{aligned} \quad (3.4)$$

Eq. (3.4) gives the total entropy generation rate. Entropy generation rate due to the pressure drop for the refrigerant can be derived from Gibbs relation,

$$T_r ds = di - v dP_r. \quad (3.5)$$

The entropy change for the refrigerant may be evaluated as

$$ds = \frac{di}{T_r} - \frac{v dP_r}{T_r} = \frac{di}{T_r} - \frac{dP_r}{\rho T_r} \quad (3.6)$$

The entropy generation rate due to pressure drop is the second term in Eq. (3.6). The entropy generation rate due to the pressure drop for the air and the refrigerant in total may then be stated as

$$\dot{S}_{\text{gen},\Delta P} = \dot{m}_r \sum_{\text{segment}} \left(\frac{\Delta P_r}{T_r \rho_r} \right) - \dot{m}_a \sum_{\text{segment}} R \ln \left(\frac{P_{a,\text{out}}}{P_{a,\text{in}}} \right). \quad (3.7)$$

Similarly, the entropy generation rate due to heat transfer for both the air and the refrigerant is given in Eq. (3.8).

$$\dot{S}_{\text{gen,ht}} = \sum_{\text{segment}} \left(\dot{m}_a c_{p,a} \ln \left(\frac{T_{a,\text{out}}}{T_{a,\text{in}}} \right) + \dot{m}_r (s_{\text{out}} - s_{\text{in}}) - \frac{\dot{m}_r \Delta P_r}{T_r \rho_r} \right) \quad (3.8)$$

The first term on the right hand side of Eq. (3.8) is the entropy generation rate due to heat transfer for the air side and the remaining terms represent the refrigerant side. For the refrigerant side, $\dot{m}_r (s_{\text{out}} - s_{\text{in}})$ represents the entropy change (a negative term due to heat loss) for the refrigerant and the pressure drop source term is extracted from it to obtain the entropy generation rate due to heat transfer for the heat exchanger. In order to prevent a possible confusion, ΔP_r is the pressure drop for the refrigerant side and it is considered as positive in Eq. (3.8).

In entropy generation minimization studies for heat exchangers, the entropy generation rate term is non-dimensionalized. The most commonly used non dimensional form (entropy generation number) is

$$N_S = \frac{\dot{S}_{\text{gen}}}{(\dot{m}c_p)_{\text{min}}} = \frac{\dot{S}_{\text{gen}}}{(\dot{m}c_p)_a}. \quad (3.9)$$

As the refrigerant is condensing, the air side is considered as the one with the minimum heat capacity.

3.3 Computational Algorithm

The computational algorithm is summarized in Figure 3.4. Firstly, the fixed geometric parameters, the operating conditions, and the correlations used are defined. For example, the air velocity, the refrigerant mass flow rate, the main dimensions of the heat exchanger and the segment length are defined. Calculations start in the superheated region. Consecutively, the two phase and subcooled region calculations are carried out. The correlations used in these three regions are different. As ε -NTU method is adopted in the heat exchanger calculations, an iterative procedure is

followed. Therefore, initial guesses are made for the outlet temperatures of the air and the refrigerant. The iterations are repeated until the error between two successive results is reduced below 1%. Next, the calculations for the following segment is started. At the end of the individual segment calculations, several performance parameters such as the pressure drop, entropy generation rate on the air and refrigerant sides, heat transfer rate, and effectiveness of the heat exchanger are calculated and recorded. Once the calculations for the superheated region are completed, the two phase calculations are performed. The two phase calculation procedure is similar to that for the superheated region. However, this time, the air outlet temperature and the segment's outlet vapor quality are guessed to obtain more accurate results at the end of the iterative process. For each segment, the vapor quality is taken as the average value of the inlet and the outlet vapor qualities. The pressure drop for each segment is calculated and the new saturation pressure is used for the following segments. The calculation procedure for the subcooled region is similar to that for the superheated region. The thermophysical properties are taken from the Matlab files working together with the main code. These files are developed by the first author and are based on the data of ASHRAE 1997. Matlab 2011b is used as the computational tool.

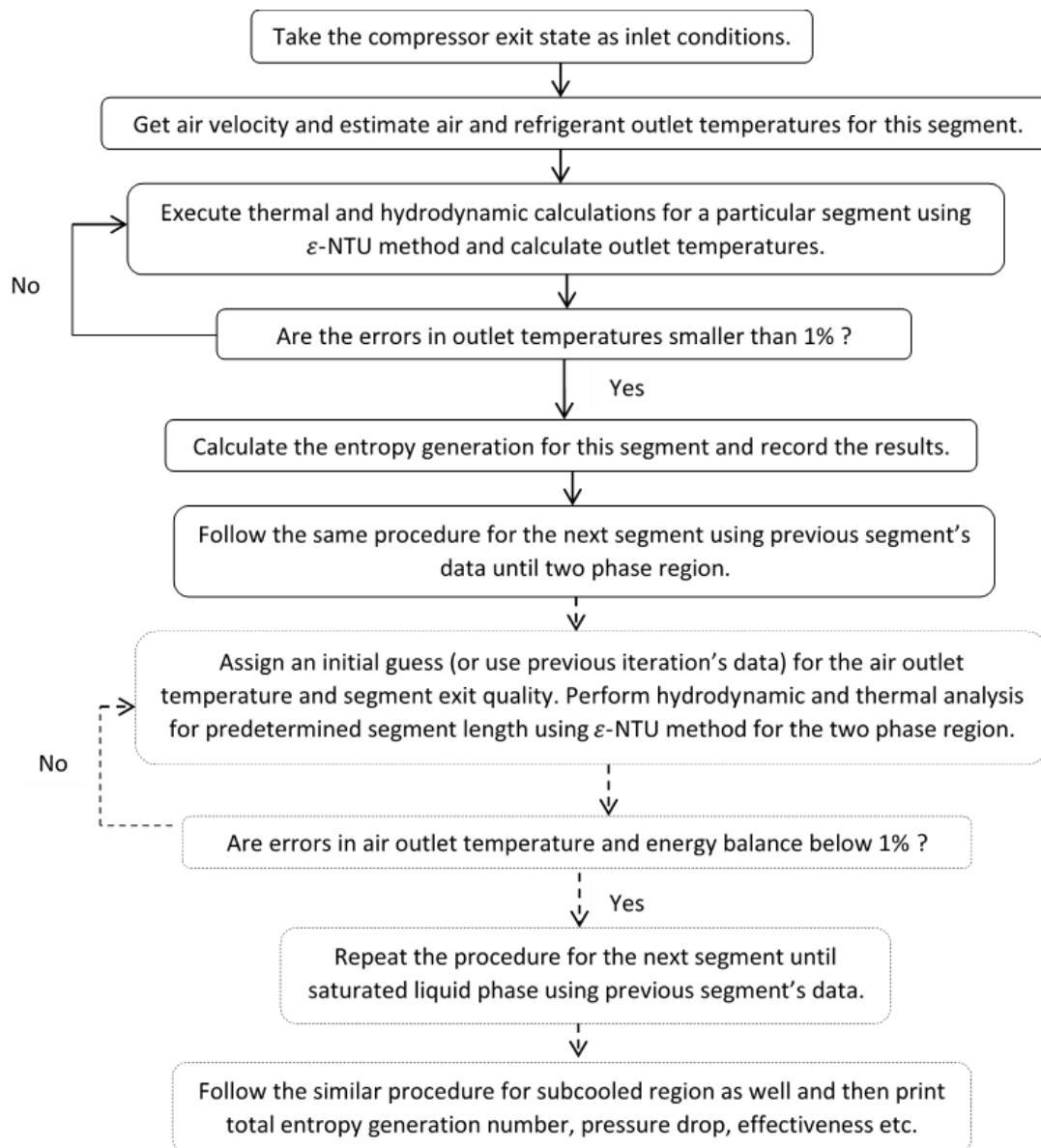


Figure 3.4 Computational algorithm of the heat exchanger design

3.4 Thermal Analysis

The heat exchanger type in the present study is air cooled, cross flow, aluminum brazed, parallel flow (ref side) heat exchanger. In this type of heat exchangers, for superheated and subcooled regions, ε –NTU relation is given by Eq. (10) (Kim and Bullard [57])

$$\varepsilon = 1 - \exp\left(\frac{NTU^{0.22}}{C_r} \{ \exp(-C_r NTU^{0.78}) - 1 \}\right) \quad (3.10)$$

where the effectiveness is defined as

$$\varepsilon = \frac{\dot{Q}}{\dot{Q}_{\max}} \quad (3.11)$$

and C_r is the ratio of the minimum heat capacity to the maximum one. Q is the heat transferred between two fluids and Q_{\max} is the maximum possible heat transfer rate.

In heat exchanger calculations, ε -NTU method is commonly applied. It is an iterative method in which the outlet temperatures of the air and the refrigerant are evaluated with successive iterations. After the iterations, the energy balance is also satisfied.

In the superheated region of the refrigerant, Eq. (3.10) may be used, however in the two phase region, as there is condensation, ε –NTU relation of Eq. (3.12) should be used ($C_r = 0$).

$$\varepsilon = 1 - \exp(-NTU) \quad (3.12)$$

After calculating the air and refrigeration side heat transfer coefficients, the overall heat transfer coefficient may be calculated as

$$\frac{1}{U_o A_o} = \frac{1}{\eta_o h_o A_o} + \frac{1}{h_i A_i} + \frac{T_\delta}{k_w A_w}. \quad (3.13)$$

The overall heat transfer coefficient in Eq. (3.13) is composed of three thermal resistances in total: the convection thermal resistances in the air and refrigeration sides and the conduction resistance of the tube wall. T_δ in Eq. (3.13) is the tube wall thickness and $k_w=k_f$ is the thermal conductivity of the tube wall material, aluminum.

Areas for each segment are defined as,

$$A_i = 2 n_{\text{channel}} n_{\text{tube}} L_{\text{seg}} (w_c + H_c) \quad (3.14)$$

A_i is the microchannels internal surface area.

$$A_o = [2 (L_{\text{seg}} - F_\delta n_{\text{fin}} + F_{h,\text{real}} n_{\text{fin}}) T_d + 2 n_{\text{fin}} F_\delta F_{h,\text{real}}] n_{\text{tube}} \quad (3.15)$$

n_{fin} is number of fins per segment and calculated as

$$n_{\text{fin}} = \frac{L_{\text{seg}}}{F_p} \quad (3.16)$$

A_o is total outer surface area of the heat exchanger.

$$A_f = [2 F_{h,\text{real}} n_{\text{fin}} T_d + 2 n_{\text{fin}} F_\delta F_{h,\text{real}}] n_{\text{tube}} \quad (3.17)$$

A_f is the fin surface area. $F_{h,\text{real}}$ is defined as

$$F_{h,real} = \sqrt{F_p^2 + F_h^2} \quad (3.18)$$

A_w is area where conduction heat transfer occurs and related to conduction thermal resistance. It is defined as

$$A_w = 2 L_{seg} T_d n_{tube} \quad (3.19)$$

η_o and η_f are the overall surface and fin efficiencies which are defined in Eqns. (3.20) and (3.21), respectively as

$$\eta_o = 1 - \frac{A_f}{A_o} (1 - \eta_f), \quad (3.20)$$

$$\eta_f = \frac{\tanh(ml)}{ml}, \quad (3.21)$$

and m is defined as

$$m = \sqrt{\frac{2 h_o}{k_f F_\delta} \left(1 + \frac{F_\delta}{T_d}\right)}, \quad l = \frac{F_h}{2} - F_\delta \quad (3.22)$$

The heat transfer coefficient for the air side is given in (Kim and Bullard 2002 [57]) as

$$h_a = \frac{j \rho_m u c_p}{Pr^{2/3}} \quad (3.23)$$

where u is the air velocity between the fins and j factor is given as (Kim and Bullard [57])

$$j = Re_{Lp}^{-0.487} \left(\frac{L_\alpha}{90} \right)^{0.257} \left(\frac{F_p}{L_p} \right)^{-0.13} \left(\frac{F_h}{L_p} \right)^{-0.29} \\ \times \left(\frac{L_l}{L_p} \right)^{0.68} \left(\frac{T_d}{L_p} \right)^{-0.235} \left(\frac{F_\delta}{L_p} \right)^{-0.05} \left(\frac{T_p}{L_p} \right)^{-0.279} \quad (3.24)$$

$$T_p = F_h + 2 T_\delta + H_c \quad (3.25)$$

The Reynolds number is defined based on the louver pitch as

$$Re_{Lp} = \frac{u L_p}{\nu} \quad (3.26)$$

The heat transfer coefficient for the superheated single phase region is calculated by the correlation of Adams et al. [58] who modified the Gnielinski equation for non-circular microchannels.

$$h_{sp} = \frac{k_r}{D_h} \left\{ 1 + 7.6 \times 10^{-5} Re \left[1 - \left(\frac{D_h}{0.001167} \right)^2 \right] \right\} \\ \times \frac{f/8 (Re - 1000) Pr}{1 + 12.7 (f/8)^{0.5} (Pr^{2/3} - 1)} \quad (3.27)$$

Re in Eqns. (3.27) and (3.28) is Reynolds number and defined as $(G D_h)/(\mu_g)$. G is mass flux, D_h is the hydraulic diameter of the channels in refrigerant side and μ_g is

dynamic viscosity of the refrigerant for gas phase. For the friction factor f , Filonenko's equation is advised to be used.

$$f = 1/(0.79 \ln(Re) - 1.64)^2 \quad (3.28)$$

Yuan et al. [5] used Moser [36]'s correlation for the two phase heat transfer coefficient for their microscale vapor compression refrigeration cycle. The same correlation is used in the present study and heat exchanger length results agree with Yuan et al. [5]'s dimension with less than 10% error. In addition, Koyama et al. [37]'s results agree with Moser et al. [36]'s for high mass fluxes. Koyama et al. [37] conducted experiments with R134a for rectangular microchannels having diameters ranging from 0.8 to 1.11 mm. Moser [36]'s correlation for two phase flow is given in Eq. (3.29).

$$Nu_{tp} = \frac{0.0994^{C_1} Re_1^{C_2} Re_{eq}^{1+0.875 C_1} Pr_1^{0.815}}{(1.58 \ln(Re_{eq}) - 3.28) + (2.58 \ln(Re_{eq}) + 13.7 Pr_1^{\frac{2}{3}} - 19.1)} \quad (3.29)$$

In Eq. (3.29) Re_1 is the liquid phase Reynolds number and is given as

$$Re_1 = \frac{G D_h (1 - x)}{\mu_1}, \quad (3.30)$$

$$C_1 = 0.126 Pr_1^{-0.448}, \quad (3.31)$$

$$C_2 = -0.113 Pr_1^{-0.563}. \quad (3.32)$$

Re_{eq} is the equivalent Reynolds number and is defined as

$$Re_{eq} = \phi_{lo}^{8/7} Re_{lo} \quad (3.33)$$

where Re_{lo} is all liquid flow Reynolds number and can be obtained if Eq. (3.30) is divided by $(1 - x)$,

$$\phi_{lo}^2 = C_3 + \frac{3.24 C_4}{Fr^{0.045} We^{0.035}}, \quad (3.34)$$

$$C_3 = (1 - x)^2 + x^2 \left(\frac{\rho_l}{\rho_g} \right) \left(\frac{C_{f,go}}{C_{f,lo}} \right), \quad (3.35)$$

$C_{f,go}$ and $C_{f,lo}$ are Fanning friction factors for vapor only and liquid only flows calculated based on $Re_{go} = (G D)/(\mu_g)$ and Re_{lo} , respectively (Moser [36]);

$$C_4 = x^{0.78} + (1 - x)^{0.24} \left(\frac{\rho_l}{\rho_g} \right)^{0.91} \left(\frac{\mu_g}{\mu_l} \right)^{0.19} \left(1 - \frac{\mu_g}{\mu_l} \right)^{0.7}, \quad (3.36)$$

with x referring to the vapor quality and g representing the vapor phase. The Fanning friction factor, C_f , is given as (Yuan [5]) and the Re classification is from (Lee and Mudawar [48])

$$f = \begin{cases} 16/Re & Re < 2000 \\ 0.079 Re^{-0.25} & 2000 < Re < 20000 \\ 0.046 Re^{-0.2} & Re > 20000 \end{cases} \quad (3.37)$$

The Weber and Froude numbers in Eq. (28) are defined as

$$We = \frac{G^2 D_h}{\sigma \rho_{tp}}, \quad (3.38)$$

$$Fr = \frac{G^2}{g D_h \rho_{tp}^2} \quad (3.39)$$

where

$$\rho_{tp} = \left(\frac{x}{\rho_g} + \frac{1-x}{\rho_l} \right)^{-1}. \quad (3.40)$$

For the subcooled region, Peng and Peterson [59]'s correlations are used for both laminar and turbulent flows. For laminar flow,

$$Nu_{sub} = 0.1165 \left(\frac{D_h}{b} \right)^{0.81} \alpha_c^{0.79} Re^{0.62} Pr^{1/3}, \quad (3.41)$$

and for turbulent flow,

$$Nu_{sub} = 0.072 \left(\frac{D_h}{b} \right)^{1.15} (1 - 2.421 (\alpha_c - 0.5)^2) Re^{0.8} Pr^{1/3} \quad (3.42)$$

where b is the center to center distance between two adjacent microchannels (not the channel width), and α_c is the aspect ratio defined as $\alpha_c = (\text{short side})/(\text{long side})$.

3.5 Hydrodynamic Analysis

Neglecting the pressure drops at the inlet and the outlet, and also the pressure change due to the density difference between the inlet and the outlet, the pressure drop for the air side multi-louvered fin geometry is given by Eq. (3.43) (Kim and Bullard [57]).

$$\Delta P_a = \frac{f_a \rho_a u_m^2}{2} \frac{A_{\text{tot}}}{A_{\text{free flow}}} \quad (3.43)$$

The friction factor f_a is correlated using 225 test data points by (Kim and Bullard [57]) as

$$f_a = Re_{Lp}^{-0.781} \left(\frac{L_\alpha}{90} \right)^{0.444} \left(\frac{F_p}{L_p} \right)^{-1.682} \left(\frac{F_h}{L_p} \right)^{-1.22} \left(\frac{T_d}{L_p} \right)^{0.818} \left(\frac{L_l}{L_p} \right)^{1.97} \quad (3.44)$$

For the single phase gas (superheated vapor) flow, the pressure drop is calculated from

$$\left(\frac{dP}{dz} \right)_g = \frac{\rho u_m^2 f}{2 D_h} \quad (3.45)$$

For the calculation of f , in Eq. (3.45), Eq. (3.28) is used.

For the pressure drop correlation in the two phase region, the correlations of Mishima and Hibiki [60] given with Eqs. (3.46-3.50) are used. Cavallini et al. [61] inspected the

pressure drop during condensation in minichannels having diameters ranging from 0.4 to 3 mm for different cross sections using refrigerant R134a. Mishima and Hibiki [60]'s correlation is reported to match the experimental results very well with standart and relative deviations noted as 11.6% and 1.2%.

$$\phi_L^2 = \frac{\Delta P_{tp,f}}{\Delta P_l} \quad (3.46)$$

$$\chi^2 = \left(\frac{dP_f}{dz} \right)_l / \left(\frac{dP_f}{dz} \right)_g \quad (3.47)$$

$$\phi_L^2 = 1 + \frac{C}{\chi} + \frac{1}{\chi^2} \quad (3.48)$$

The parameter C in Eq. (3.48) is defined for round tubes and rectangular channels in terms of the hydraulic diameter as (Mishima and Hibiki [60])

$$C = 21 (1 - e^{-0.319 \times 1000 D_h}). \quad (3.49)$$

The frictional pressure drop per length for liquid phase is given as

$$\left(\frac{dP_f}{dz} \right)_l = \frac{2 C_{f,l} G^2 (1 - x)^2}{D_h \rho_l} \quad (3.50)$$

where $C_{f,l}$ is the liquid phase friction factor and for Re_l or $Re_g < 2000$,

$$\begin{aligned} Po &= C_{f,l} \times Re \\ &= 24 \times (1 - 1.3553 \alpha_c + 1.94677 \alpha_c^2 - 1.7012 \alpha_c^3 \\ &\quad + 0.9564 \alpha_c^4 - 0.2537 \alpha_c^5). \end{aligned} \quad (3.51)$$

For turbulent conditions, Eq. (3.37) can be used with appropriate Reynolds numbers.

The accelerational pressure drop may be calculated using (Lee and Mudawar [48])

$$\Delta P_{\text{acc}} = G^2 \left\{ \left[\frac{v_g x_{\text{out}}^2}{\alpha_{\text{out}}} + \frac{v_l (1 - x_{\text{out}})^2}{(1 - \alpha_{\text{out}})} \right] - \left[\frac{v_g x_{\text{in}}^2}{\alpha_{\text{in}}} + \frac{v_l (1 - x_{\text{in}})^2}{(1 - \alpha_{\text{in}})} \right] \right\}. \quad (3.52)$$

The void fraction α is given by Zivi [62] as

$$\alpha = \left[1 + \left(\frac{1 - x}{x} \right) \left(\frac{v_l}{v_g} \right)^{\frac{2}{3}} \right]^{-1}. \quad (3.53)$$

It is important to note that the accelerational pressure drop in condensation causes pressure recovery. Then the total pressure drop $\Delta P_{\text{tot,tp}}$ is determined using

$$\Delta P_{\text{tot,tp}} = \Delta P_{\text{tp,f}} - \Delta P_{\text{acc}}. \quad (3.54)$$

Finally, the pressure drop in the subcooled region is calculated using Eq. (3.50).

3.6 Validation of Computer Code

Validation process has been made by comparing the calculated length of a heat exchanger with experimentally tested condenser benefiting from experimental condenser data from the literature. By doing so, correlations used and calculation procedure are validated. It is expected that dimensions of the tested heat exchanger and theoretically calculated heat exchanger length match according to the experimental data given in the literature.

Studies related to miniature refrigeration cycles are summarized in introduction section. Most of these studies do not give detailed information about the states, condenser load dimensions of the heat exchanger etc. Only Yuan et al. [5] has provided enough information about the cycle parameters like COP, η_{rev} , \dot{Q}_{evap} and P_{evap} . Using these, the condensation heat load and the saturation temperature of the condensing region are calculated. However, the beginning and end states of the condenser are not known. For this reason, the refrigerant at the exit of the condenser is assumed to be saturated liquid. Based on this assumption, the mass flow rate of the refrigerant R134a is calculated as 2.15 g s^{-1} thanks to first law analysis on evaporator and condenser. For validation, a case study has been conducted for the same geometry of the heat exchanger, except the length of it. Input data and results for the validation study are given in Table 3.4.

Table 3.4 Input parameters and results of the validation case (Yuan et al. [5])

\dot{m}_r	$2.15 \times 10^{-3} \text{ kg s}^{-1}$
\dot{V}_a	$260 \text{ m}^3\text{h}^{-1}$
\dot{Q}_{sp}	97.44 W
\dot{Q}_{tp}	294.58 W
$\dot{Q}_{cond,tot}$	392 W
\dot{Q}_{evap}	236 W
COP	1.51
η_{rev}	0.32
L_{tot} (present study)	0.12125 m
L_{tot} (Yuan et al. [5])	0.135 m
Error	$\sim 10\%$

The length of the heat exchanger is calculated to be 0.121 m which involves approximately 10% deviation with the heat exchanger length used in Yuan et al. (2015) [5]'s experiments. Yuan et al. [5] did not report theoretical calculations related to heat transfer correlations; they only presented experimental results. An error of 10% seems reasonable when the deviations in heat transfer correlations for miniature systems in the literature are considered. There may be other sources of errors such as the assumptions made for determining the inlet and the outlet states of the condenser.

3.7 Condenser Results

In this section, the influence of parameters such as the fin pitch, fin height, air mass flow rate, microchannel hydraulic diameter and the louver angle on the entropy generation rate are examined. The parameters given in Table 3.1, and Table 3.2 are used in the calculations unless otherwise is specified.

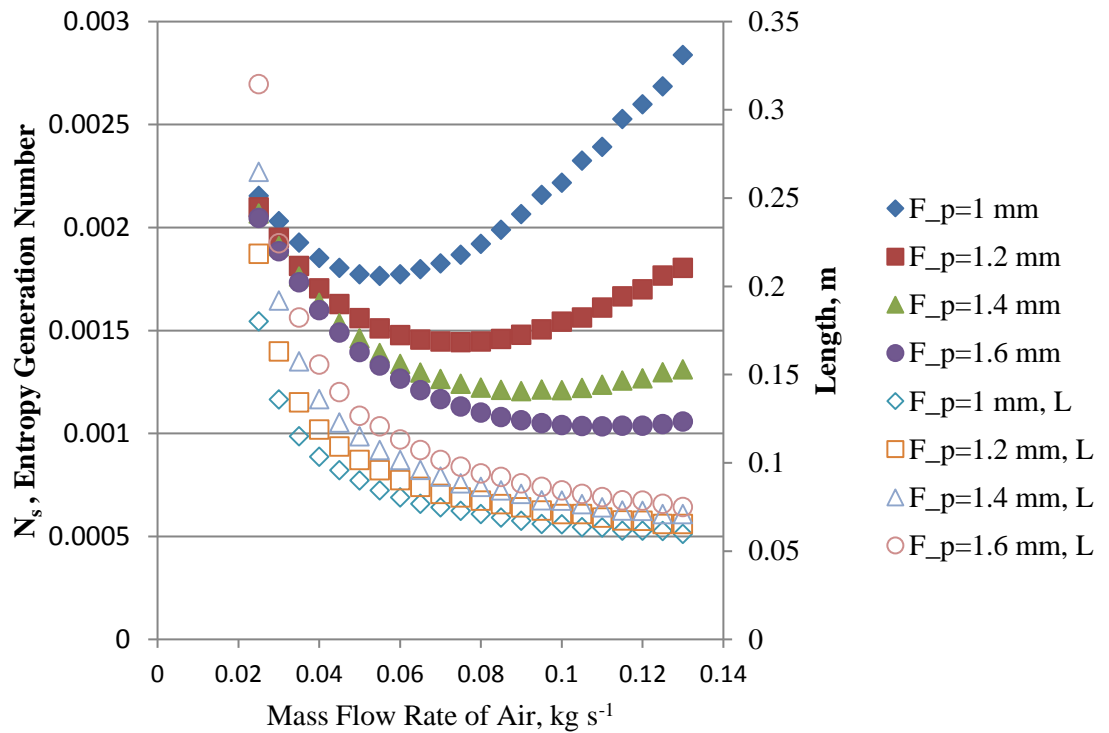


Figure 3.5 Fin pitch effect on entropy generation number and heat exchanger length for various mass flow rates

In Figure 3.5, the entropy generation number and the length of the heat exchanger are plotted against the air mass flow rate for various fin pitch values. It can be concluded

from the figure that higher fin pitch resulted in lower entropy generation number. This is because of the reduction in the pressure drop on the air side. After a certain mass flow rate the entropy generation number starts to increase for all cases. This may be explained by the increased air mass flow rate increasing the pressure drop severely and causing an increase in the entropy generation number. Although the heat exchanger gets smaller with higher air mass flow rates, it is neither thermally nor hydrodynamically efficient to use the system in the mentioned ranges. It may be noticed that for low mass flow rates, the required heat exchanger length becomes significantly shorter even for differential increases in the air mass flow rates. However, after an optimum mass flow rate, the length of the heat exchanger does not decrease significantly. Although it is hard to report an exact optimum air mass flow rate, an interval may be provided. The results in Figure 3.5 suggests an optimum mass flow rate interval of $0.55\text{--}0.11 \text{ kg s}^{-1}$ for different fin pitches. This interval is within the working range of air fans in the market. The optimal air mass flow rate giving the optimal entropy generation number depends on the selected geometry. In the present paper, 0.08 kg s^{-1} is considered as a reference mass flow rate as working with higher flow rates may not be reliable in terms of the fan usage. Air mass flow rates greater than 0.08 kg s^{-1} for a corresponding fin pitch value of 1.3 mm do not cause a tremendous increase in the entropy generation number. Whereas the entropy generation number sharply increases after the optimum mass flow rate for low fin pitches, it slightly increases for higher ones. It should be noted that the entropy generation number keeps increasing for each case with the increase of air mass flow rate after the optimal point as well, however, the dimensionless entropy generation number which is obtained by dividing the entropy generation rate by $(m_a c_p)_{\min}$ depicts almost a horizontal behavior for the mentioned case.

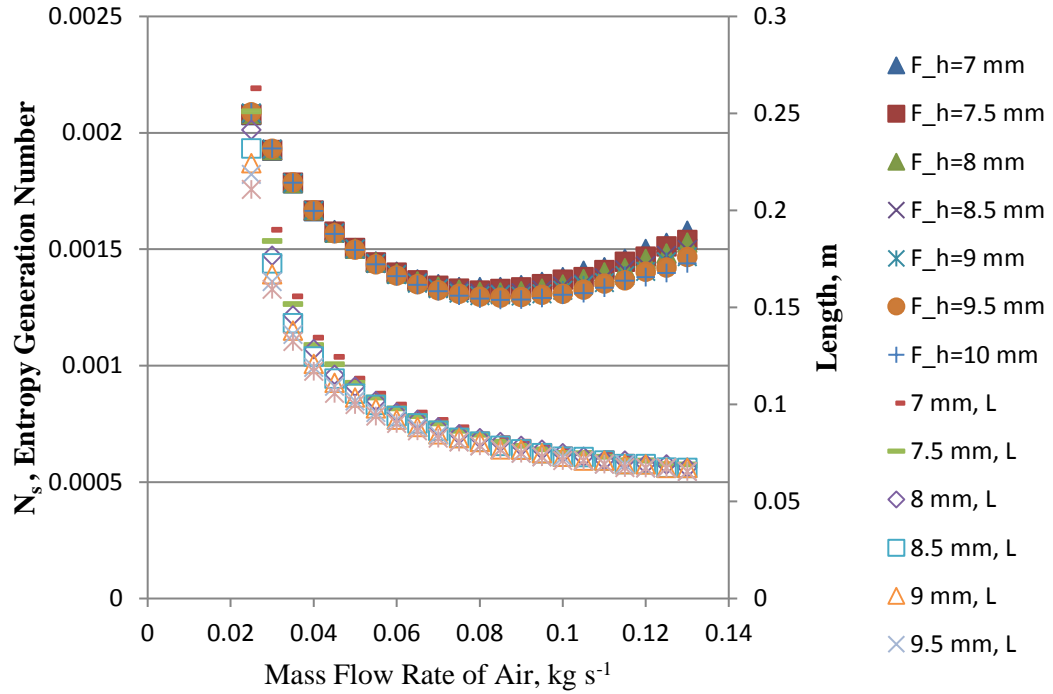


Figure 3.6 Fin height effect on entropy generation number and heat exchanger length for various mass flow rates

The fin height effect on entropy generation number is given in Figure 3.6. The optimum air mass flow rate is found to be between $0.08\text{--}0.085\text{ kg s}^{-1}$ for each fin height case. Although there is no major deviation in the optimum air mass flow rate, the entropy generation number is lower for larger fin heights especially for higher mass flow rates. In this high mass flow rate region, the change in the heat exchanger length does not yield a change in entropy generation number. Even though it seems logical to use higher fin heights due to low entropy generation numbers at low flow rates, it is important to note that it increases the height of the heat exchanger (1 mm increase in the fin height corresponds to a 9 mm increase in the total height).

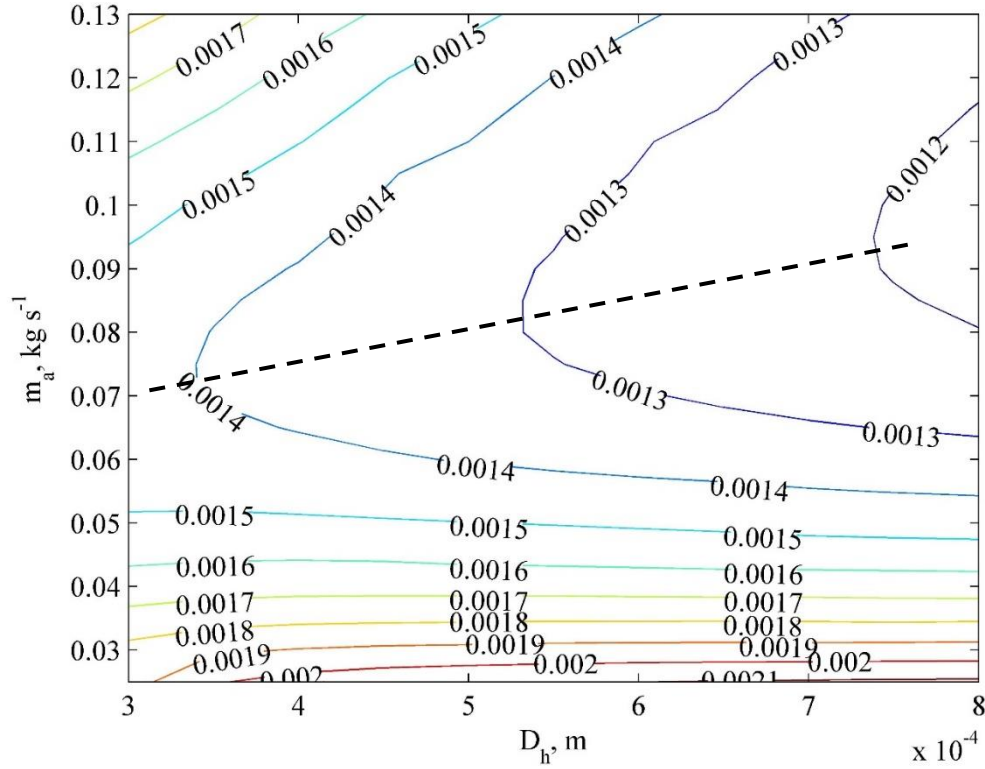


Figure 3.7 Entropy generation number map for the air mass flow rate and the hydraulic diameter ($\alpha_c = 1$)

The combined effects of the air mass flow rate and the hydraulic diameter on entropy generation number are mapped in Figure 3.7. For lower mass flow rates of air, the entropy generation number is quite high. A dashed line showing the minimum entropy generation number is drawn for convenience. Using this line, the optimal mass flow rate can be determined for a specific hydraulic diameter. In the inspected range of hydraulic diameter, optimal mass flow rate is approximately between 0.07-0.1 kg s⁻¹. Working with low air mass flow rates does not seem to be logical due to higher entropy generation numbers.

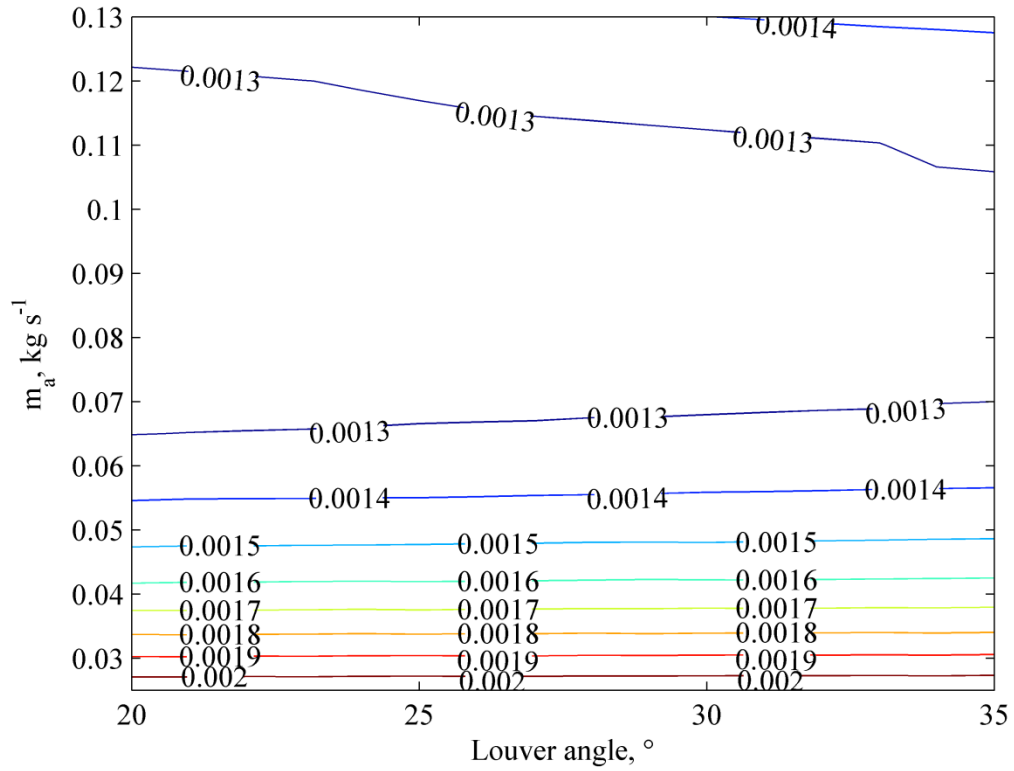


Figure 3.8 Entropy generation number map for the air mass flow rate and the louver angle

The combined effects of the louver angle and air mass flow rate on entropy generation number are mapped in Figure 3.8. As can be observed from the figure, the entropy generation number lines follow horizontal trends generally. This means that the louver angle does not have significant effect on the entropy generation number for a specific air mass flow rate. There is a remarkable area between the two entropy generation number lines of 0.0013. In this region which corresponds to an air mass flow rate interval between approximately 0.07-0.11 kg s⁻¹, the entropy generation number is the

minimum. Regardless of the louver angle, the entropy generation number is at a minimum in this range.

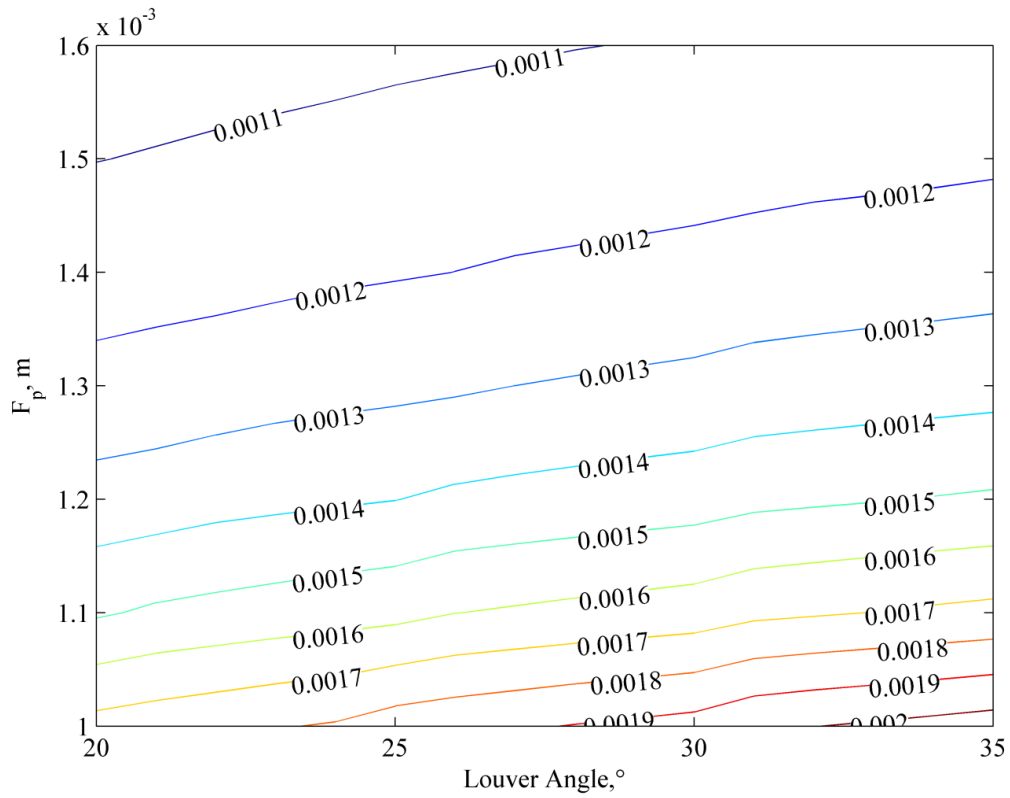
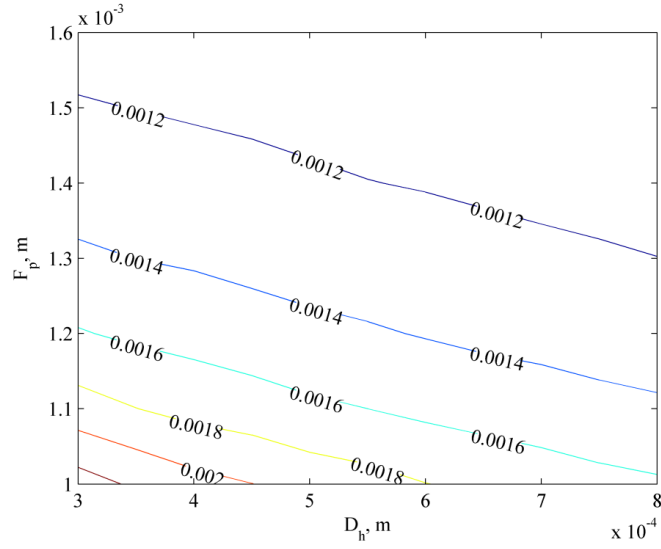


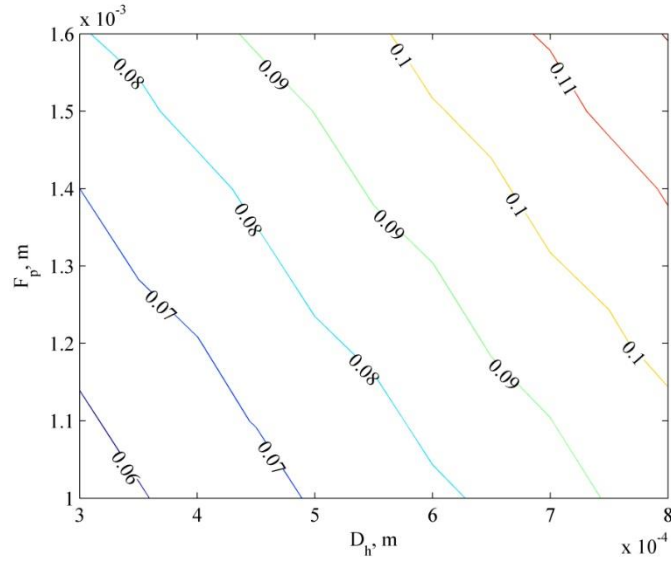
Figure 3.9 Entropy generation number map for the fin pitch and the louver angle at a constant air mass flow rate of $\dot{m}_a = 0.08 \text{ kg s}^{-1}$

In Figure 3.9, the in pitch and the louver angle entropy generation number map is presented. It may be observe from the figure that there is a slight increase in the entropy generation number for the increment of louver angle for a constant fin pitch. On the other hand, the fin pitch has a substantial influence on the entropy generation number.

As observed from the previous figures too, for higher fin pitch the entropy generation number decreases.



(a) Entropy generation number



(b) Heat exchanger length, m

Figure 3.10 Entropy generation number (a) and heat exchanger length (b) maps for the fin pitch and the hydraulic diameter ($\alpha_c = 1$) at the constant air mass flow rate of $\dot{m}_a = 0.08 \text{ kg s}^{-1}$

The entropy generation number and heat exchanger length maps considering the effects of the fin pitch and the hydraulic diameter at the constant air mass flow rate of $\dot{m}_a = 0.08 \text{ kg s}^{-1}$ are given in Figure 3.10. It is observed that the entropy generation is lower when the hydraulic diameter and the fin pitch increase. However, this decrease brings about the increase in the heat exchanger length as well. For a fixed heat exchanger length, it is observed that the entropy generation is lower for low hydraulic diameters and for high fin pitch.

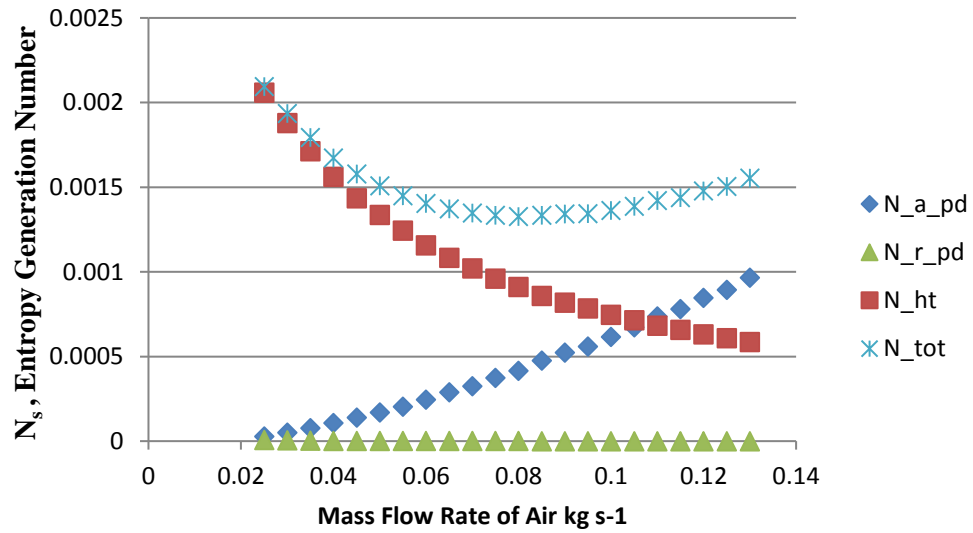


Figure 3.11 Entropy generation number due to pressure drop and heat transfer

The contributions of heat transfer and pressure drop to the entropy generation number for both air and refrigerant sides are presented in Figure 3.11. As may be realized from the figure, the total entropy generation number increases after a certain air mass flow rate. The reason is that the air side pressure drop increases due to high mass flow rates. Although the entropy generation number due to heat transfer decreases in the mentioned region, the air side pressure drop overcomes this decrease in the entropy

generation number. As the refrigeration mass flow rate is fixed, the change in the entropy generation number due to refrigerant pressure drop is almost constant for all air mass flow rates.

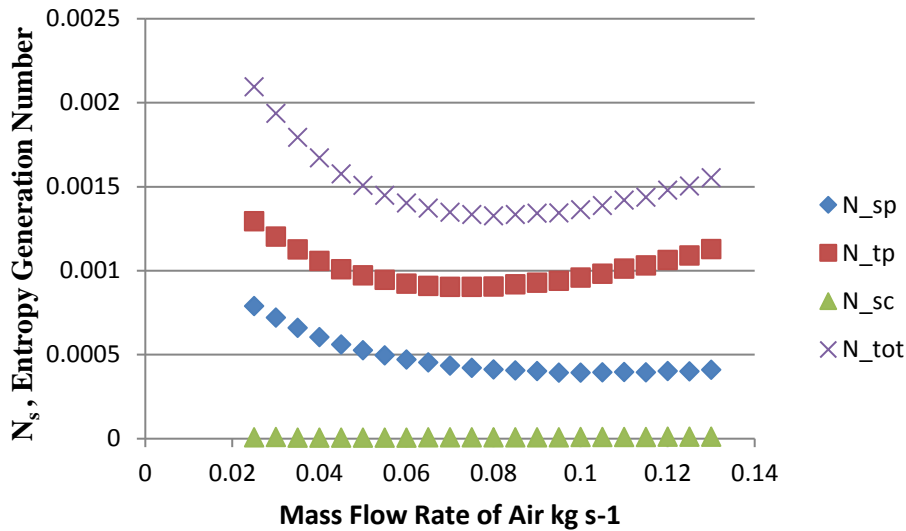


Figure 3.12 Entropy generation number distribution for superheated, two phase and subcooled parts

The variation of the entropy generation number with the phase of the refrigerant is depicted in Figure 3.12. The entropy generation number in the two phase region is the dominant factor in the total entropy generation number as the major part of the heat is transferred in the two phase region. The superheated region is shorter compared to the two phase region, and hence, has a minor effect on the total entropy generation number. An important remark about this plot is that while the entropy generation number in the two phase region increases with the pressure drop on the air side after a certain air mass flow rate, a similar behavior is not observed in the superheated region (it is almost constant in the superheated region). It can be inferred that the pressure

drop effect of the air side is balanced with the decrease in the entropy generation number due to heat transfer in the superheated region.

An important parameter in heat exchanger design, NTU is calculated for $\dot{m}_a = 0.08 \text{ kg s}^{-1}$ conditions stated in Table 3.1 and Table 3.2. As segmentation procedure is followed in the calculations, NTU varies. For the superheated region, it is calculated to be around 0.17. On the other hand, it is calculated as 0.3 for high vapor quality region and reduces up to 0.22 for low vapor quality region.

As a final remark, the provided entropy generation number maps may be useful in designing microchannel heat exchangers for similar operation.

CHAPTER 4

EXPERIMENTS

In the experimental part of the study, some performance tests have been conducted. The tested refrigeration cycle is composed of four main parts, evaporator (microchannel heat sink), compressor, condenser (microchannel heat exchanger) and throttling valve. The maximum possible cooling load given to the evaporator without any burnout or instability in the cycle has been explored. Coefficient of performance, COP, average heat transfer coefficient and second law efficiency, η_{II} , of the cycle have been estimated for various conditions. Performance tests have been conducted for different evaporator cooling loads, refrigerant loads and air side fan speeds, and compressor powers.

Table 4.1 Experiments matrix

Examined parameter	Figure number	Horizontal axis	Varied parameter	Conditions
COP, η_{II} vs Q_{evap}	Figure 4.7	Q_{evap} : 50 – 90 W	CP : 50, 60, 70 %	RC= 64 g, FS = 1
COP, η_{II} vs T_{sat}	Figure 4.8	T_{sat} : 19.8-23.6°C	Q_{evap} : 80, 85, 86 W	CP= 50%, RC= 64 g, FS=1
T_{base} , h_{av} vs T_{sat}	Figure 4.9	T_{sat} : 19.8-23.6°C	Q_{evap} : 80, 85, 86 W	CP = 50%, RC = 64 g, FS= 1
T_{base} , h_{av} vs Q_{evap}	Figure 4.10	Q_{evap} : 80 – 90 W	FS: 1,2	$T_{sat} \cong 21.5^\circ\text{C}$, CP = 50%, RC = 64 g
COP, η_{II} vs Q_{evap}	Figure 4.11	Q_{evap} : 80 – 95 W	FS: 1,2	CP = 50%, RC = 64 g

\dot{m}_{ref} changes between 1-1.34 g s⁻¹ in the experiments. It varies case by case but it is around 1.2 g s⁻¹ for most of the cases.

4.1 Experimental Setup

4.1.1 Components of the Cycle and Measuring Devices

Schematic of the experimental set up is given in Figure 4.1. The evaporator in the test section is a microchannel heat sink. It is made of oxygen free copper. Rectangular microchannels are manufactured on a copper block which is embedded in a PEEK (a very good thermal insulator, $k \cong 0.25$ W/m K at 300 K) casing. Two cartridge heaters are mounted in these copper blocks to simulate the chip dissipating the heat. In order to provide visibility of the flow, the top surface is made of plexiglass material. After the test section, a post heater is implemented to obtain vapor phase before the compressor inlet. In order to prevent liquid entrance to the compressor inlet, an accumulator is used just before the compressor. It is designed such that it holds the liquid and only allows the vapor phase to pass. An oil free, hermetic linear compressor is used. It is called a microcompressor by its manufacturer Embraco Inc from Brasil. Pressurized refrigerant enters the condenser which is basically an air cooled aluminum brazed microchannel heat exchanger. It's structure is similar to the one depicted in Figure 3.1 but the fins do not have louvers, they are just plain fins. Dimensions are also different. More information will given in this chapter about the condenser dimensions. In order to remove any contamination and moisture in the cycle, a liquid filter drier has been mounted.

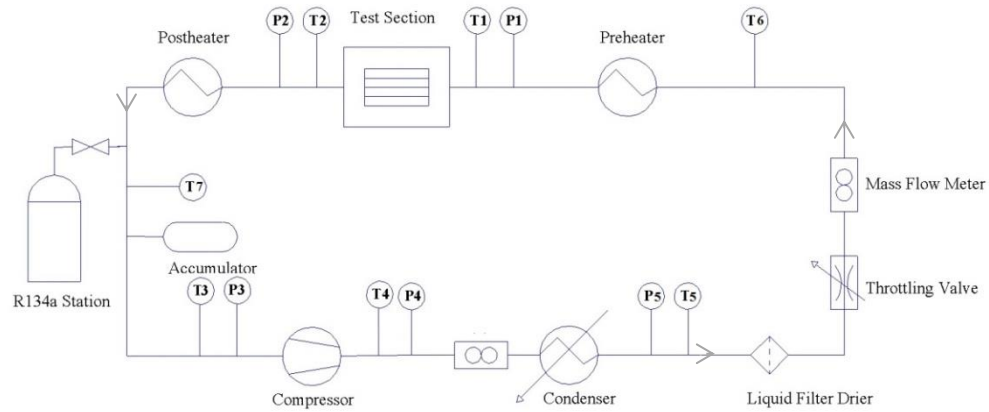


Figure 4.1 Schematic diagram of the test setup [4]

A throttle valve is used for the expansion process. If the evaporator is desired to be tested independently, a preheater is used to obtain desired vapor quality before the evaporator. Its use is optional and it is not used in the present study.

As measuring devices, two digital Coriolis type mass flowmeters, pressure transducers and thermocouples are used. The mass flowmeters are implemented after the throttling valve and the compressor to measure the mass flowrate of the working fluid. Pressure transducers are mounted at the inlet and outlet of the condenser and evaporator so that the pressure drop can be measured. Temperature is measured by means of thermocouples from many different locations. Three thermocouples in the copper block of the evaporator are implemented 2 mm beneath the base. Two of them are placed close to inlet and outlet and the last one is placed at the middle. In order to be able to measure the refrigerant's temperature in the evaporator, two thermocouples are placed at the inlet and the outlet. For the air side of the condenser, two thermocouples at the inlet and outlet of the air duct are used. On the refrigerant side, again two thermocouples at the inlet and outlet of the condenser are used.

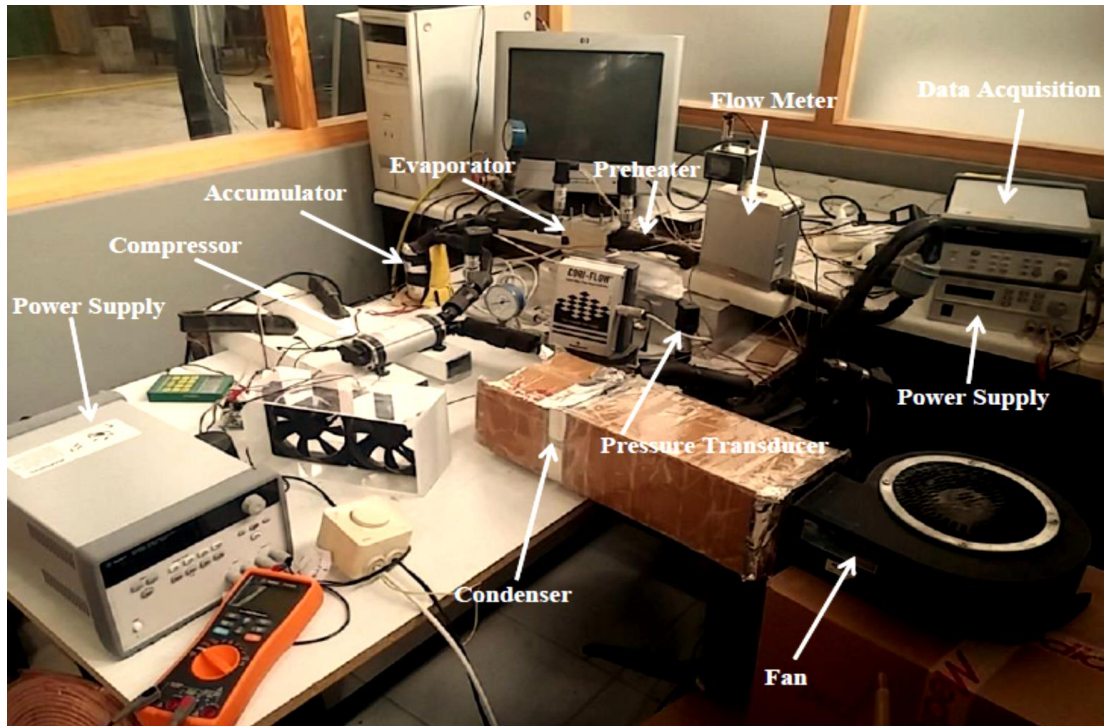


Figure 4.2 Photograph of the test setup

An anemometer is used to measure the air velocity across the condenser. For obtaining hydrodynamically fully developed air flow, a rectangular duct is utilized. Air velocity is measured at the end of the duct from 9 different locations and the average of these values is taken as the mean air velocity. Specifications and properties of the cycle components and measuring devices are given in Table 4.2.

Table 4.2 Application and specifications of the components used in the test setup.

Some information is obtained from [4]

Component	Application	Specification
Micro-compressor	Pressurize the refrigerant.	Hermetic Linear compressor manufactured by EMBRACO
Condenser	Dissipates the heat from the hot side of the cycle thanks to air.	Air cooled aluminum brazed heat exchanger.
Accumulator	By letting only gas phase to flow, it prevents damaging the compressor.	Material: stainless steel, dimension: Dia. 5 mm, Height: 10 mm
Throttling valve	Provides expansion.	Manufactured by NUPRO company
Digital mass flow meter	Measures the mass flow at the inlet of the evaporator.	Mini CORI-FLOW Manufactured by Bronkhorst
Anemometer	Measures air velocity in the air side of the condenser.	KM 4003
Gas station	Provides R134a refrigerant.	
Liquid drier filter	Adsorbs system contaminations.	lett DFS-052S
Pressure transducer	Measures the pressure at the inlets and outlets of the evaporator and the condenser.	PX4201 Manufactured by OMEGA Pressure range: 0-600 psig
Cartridge heaters	Apply uniform heat flux to the evaporator.	Power range: 0-200 W
Wire heater (postheater)	Guarantees that only vapor inputs the compressor.	Power range: 0-10 W
Wire heater (preheater)	Adjusts the inlet vapor quality.	Power range: 0-10 W
DC power supplies	Provides power for microcompressor, heaters and pressure transducers	Manufactured by Agilent Technologies
Data acquisition	Gathers temperatures and pressures.	Agilent 34972A
Thermocouples	Measures temperatures at the inlet and outlet of the evaporator and condenser (air side also), and temperatures just 2 mm under the bottom wall of the microchannels.	T-type
Test section (Micro-evaporator)	Will be described in the next section.	
Fan	Provides and adjusts air flow across the condenser.	

4.1.2 Microchannel Evaporator

Forty microchannels are manufactured on an oxygen free copper block. Rectangular cross section channels have dimensions of $700\ \mu\text{m} \times 250\ \mu\text{m} \times 19\ \text{mm}$ ($H_c \times w_c \times L$). Total width of the channels is 14.44 mm. Heat is supplied to the evaporator through cartridge heaters which are mounted on two holes drilled in the copper block. In order to estimate heat transfer coefficient, thermocouples are mounted on just 2 mm under the microchannels. Three tiny holes are drilled to implement the thermocouples. These thermocouples are positioned at the evaporator inlet, outlet and right in the middle of the two. Figure 4.3 presents the fabricated microchannels and the copper block.

A zoomed side view of the microchannels is given in Figure 4.4.

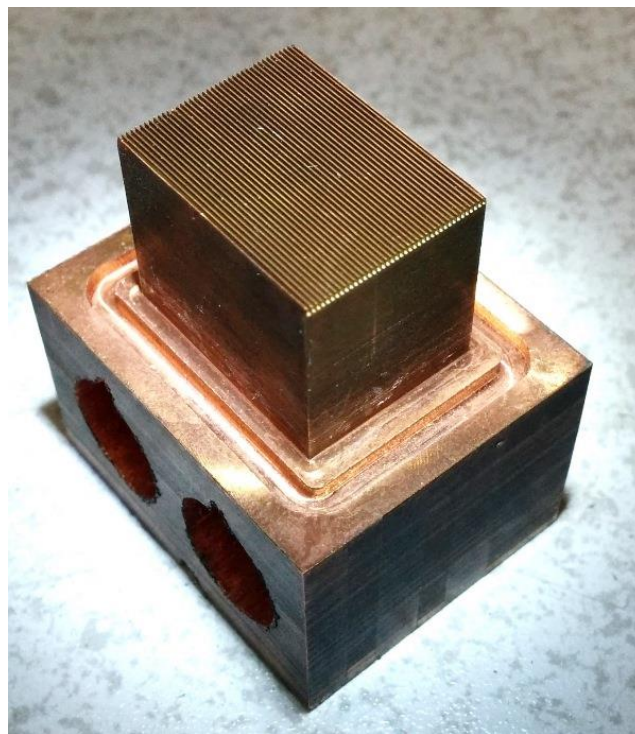


Figure 4.3 Evaporator test piece [4]

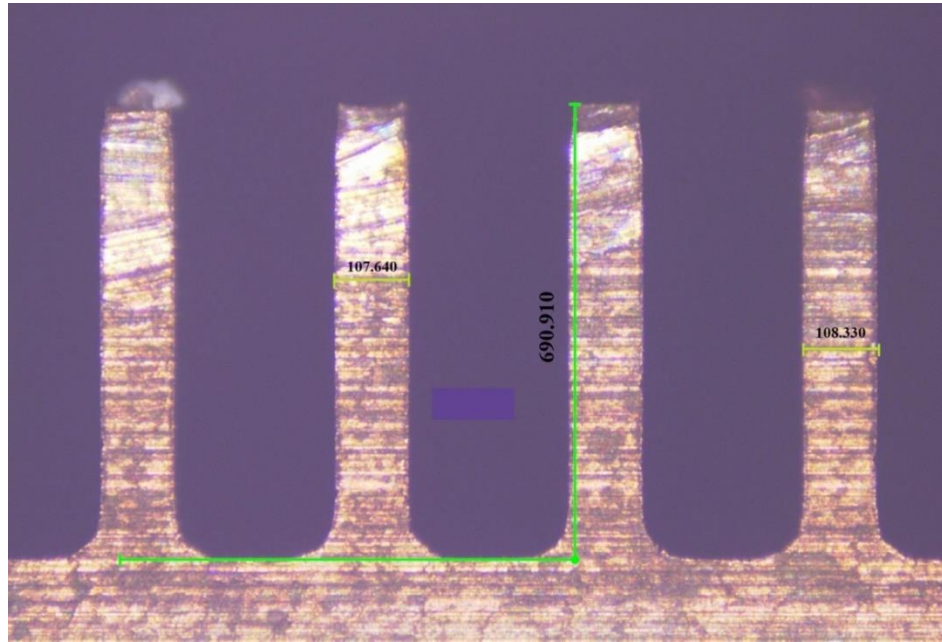


Figure 4.4 Side view of the fabricated microchannels (dimensions in μm) [4]

The copper block is enclosed by PEEK (Polyether ether ketone) cover material as shown in Figure 4.5. This covering is essential both for sealing and thermal insulation. Leakage from the copper test piece is prevented using this coverage. It also serves as thermal insulator. The refrigerant inlet and outlet manifolds are formed on this transparent covering which enables the observation of refrigerant flow.

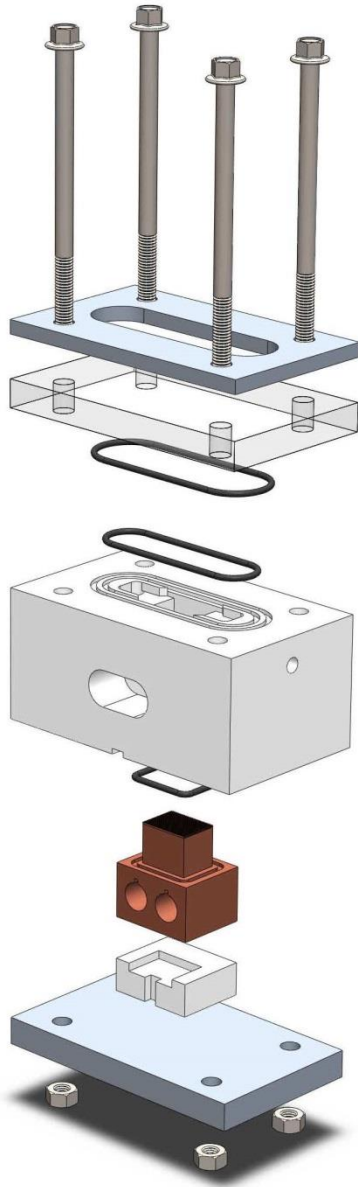


Figure 4.5 Evaporator test section [4]

4.1.3 Microchannel Condenser

In the hot side of the cycle, an air cooled microchannel heat exchanger has been used. In the experiments, a variable speed fan is employed on the air side of the heat exchanger. On the refrigerant side, microchannel dimensions are $500\text{ }\mu\text{m} \times 500\text{ }\mu\text{m}$. There are 25 microchannels in each row (there are 8 rows in total). The total width, T_d , of the heat exchanger is 30 mm. On the air side plain fins are used. The distance between two fins is 2.7 mm. The fin height is 10 mm. The total heat exchanger height is 120 mm, while tube length is 131 mm, and the overall heat exchanger length is 160 mm. Tube side microchannels and fin side of the heat exchanger can be seen from Figure 4.6. This is not the final state of the heat exchanger.

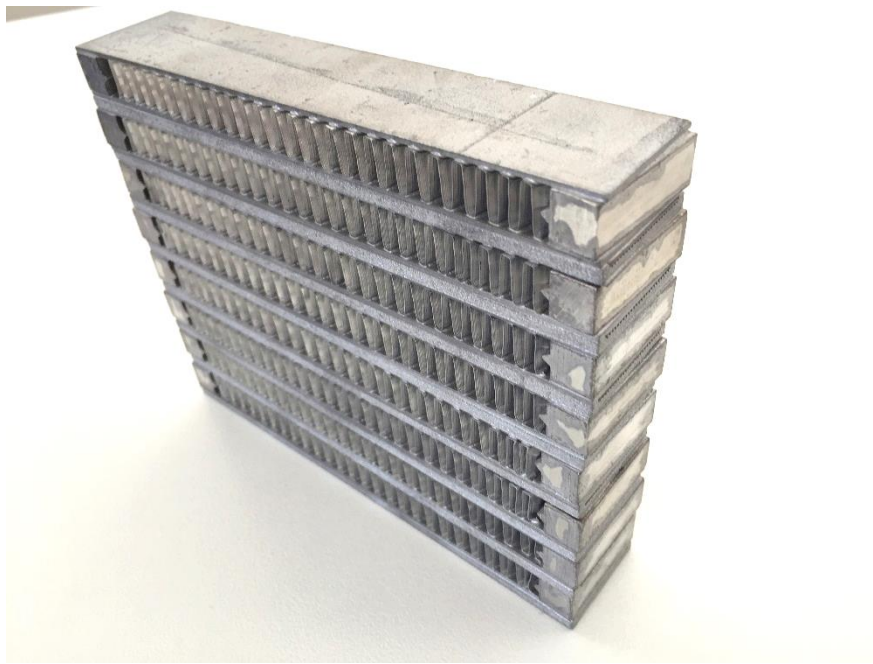


Figure 4.6 Condenser test piece [4]

Condenser dimensions used in the experiments are summarized in Table 4.3,

Table 4.3 Condenser dimensions used

Tube depth, T_d	30 mm
Fin thickness, F_δ	0.1 mm
Fin height, F_h	10 mm
Fin pitch, F_p	2.7 mm
Tube wall thickness, T_δ	2 mm
Tube pitch, T_p	14.5 mm
n_{tube}	2
n_{pass}	4
Microchannel height, H_c	0.5 mm
Microchannel width, w_c	0.5 mm
Microchannel wall thickness, w_w	0.5 mm

The refrigerant (R-134a) flows through two tube series $n_{\text{tube}} = 2$ and makes four passes, $n_{\text{pass}} = 4$.

4.1.4 Analysis of the Experimental Data

Experimental data is taken with three second intervals. After reaching steady state, the average of the data collected within the last 30 seconds is used.

The total cooling load provided to the evaporator can be estimated by multiplying the voltage and current values supplied to the cartridge heaters.

$$\dot{Q}_{\text{evap}} = \dot{Q}_c = V \cdot I \quad (4.1)$$

For the performance evaluation of the cycle COP and second law efficiency are checked. The COP is defined as the ratio of the cooling load to the compressor power.

$$\text{COP} = \frac{\dot{Q}_{\text{evap}}}{\dot{W}_{\text{comp}}} \quad (4.2)$$

The second law efficiency of a refrigeration cycle is defined as the ratio of availability out in product to availability in [63]

$$\eta_{\text{II}} = \frac{\text{Availability out in product}}{\text{Availability in}} = \left[\frac{[-\int (1 - \frac{T_0}{T_A}) \delta \dot{Q}_{\text{evap}}]}{\dot{W}_{\text{comp}}} \right] \quad (4.3)$$

In Eq. (4.3), T_0 is the reference temperature (dead state) and T_A is the temperature that the cycle receives the energy. If the T_A is taken as evaporating temperature and T_0 as condensing temperature assumed to be equal to environment temperature for ideal cycle, second law efficiency can be defined as the ratio of COP of the cycle to the COP of ideal vapor compression refrigeration cycle.

$$\eta_{\text{II}} = \frac{\text{COP}}{\text{COP}_{\text{rev}}} = \frac{-\dot{Q}_{\text{evap}}}{\dot{W}_{\text{comp}}} \left(1 - \frac{T_h}{T_c} \right) \quad (4.4)$$

COP_{rev} can be estimated using the cold (evaporating) and hot side (condensing) temperatures and defined as $\text{COP}_{\text{rev}} = T_c / (T_h - T_c)$.

Another important performance criterion in the data analysis is the heat transfer coefficient. It is estimated as,

$$h_{av} = \frac{\dot{Q}_{evap}}{(2 \eta_{fin} H_c + w_c) n L (T_{base} - T_{sat})} \quad (4.5)$$

T_{base} is estimated using Fourier's law from the readings of three thermocouples located 2 mm beneath the base. When estimating the base temperature, the average of the three temperature of the three temperature readings is considered and a single base temperature is used.

$$\dot{Q}_{evap} = -k A \frac{dT}{dx} = -k (L \times W) 10^{-3} m \frac{T_{base} - T_{meas}}{2 \times 10^{-3} m} \quad (4.6)$$

η_{fin} is fin efficiency defined as,

$$\eta_{fin} = \frac{\tanh(m H_c)}{m H_c} \quad (4.7)$$

where m is defined as

$$m = \left(\frac{h P}{k_{fin} A_c} \right)^{\frac{1}{2}} = \left(\frac{2 h}{k_{fin} w_w} \right)^{\frac{1}{2}}. \quad (4.8)$$

4.2 Energy Balance for the Refrigeration Cycle

A simple energy balance calculation is conducted for the complete cycle. Principles of the first law of thermodynamics is applied to check the validity of the measurements. An evaporator cooling load of 70 W is considered for energy balance analysis. The summation of the evaporator, and post heater cooling loads and work applied to the

compressor must be equal to the heat dissipated from the condenser. The states throughout the cycle are given in Table 4.4.

Table 4.4 Temperatures and pressures at various states of the cycle at $\dot{Q}_{\text{evap}} = 70 \text{ W}$

State	Location	Pressure (bar)	Temperature (°C)
1	Evaporator-inlet	6.05	20.89
2	Evaporator-outlet	6.07	21.01
3	Condenser-inlet	7.51	32.93
4	Condenser-outlet	7.17	27.51
5	Compressor-inlet	6.07	30.61

Heat applied to the evaporator is known as $\dot{Q}_{\text{evap}} = 70 \text{ W}$. Mass flow rate of the refrigerant is measured to be 1.34 g/s. The work done on the cycle by the compressor is calculated by multiplication of voltage and current values applied on the compressor. Power of the fans to cool down the compressor is included in this value so the fan power should be subtracted from this value.

$$W_{\text{comp}} = W_{\text{comp, tot}} - W_{\text{cooling fans}}$$

Current and voltage values exerted on the compressor are 1.59 A and 24 V, respectively.

$$\dot{W}_{\text{comp-tot}} = 24 \text{ V} \times 1.59 \text{ A} = 38.16 \text{ W}$$

$$\dot{W}_{\text{cooling fans}} = 13 \text{ W}$$

$$\dot{W}_{\text{comp}} = 25.16 \text{ W}$$

$$\dot{Q}_{\text{post heater}} = 46.86 \text{ W}$$

If the energy balance is written for steady state conditions,

$$\dot{W}_{\text{comp}} + \dot{Q}_{\text{evap}} + \dot{Q}_{\text{post heater}} \stackrel{?}{=} \dot{Q}_{\text{cond},a}$$

$$\dot{W}_{\text{comp}} + \dot{Q}_{\text{evap}} + \dot{Q}_{\text{post heater}} = 25.6 \text{ W} + 70 \text{ W} + 46.86 \text{ W} = 142.46 \text{ W}$$

Hence, the condenser heat load has been found as 142.46 W. This value can be compared with the heat transfer calculated from the air side. The mean velocity in the duct of the condenser is measured to be 2.65 m/s as a result of measuring the velocities at 9 different locations and taking the average of them. During the experiments, air velocity is changed and three different velocities have been tested which are tabulated in Table 4.5.

Table 4.5 Fan stages and corresponding velocities

Fan Stage	$u_{m,a}$, m/s (in duct)	V_a , m ³ /h	\dot{m}_a , kg/s
1	2.65	171.72	0.049422
2	4.44	287.71	0.082805
3	6.67	432.22	0.124374

*** Air properties are evaluated at 296 K and 90 kPa**

$$\dot{m}_a = \rho A u_m = 1.0361 \frac{\text{kg}}{\text{m}^3} (0.15 \times 0.12) \text{m}^2 \left(2.6555 \frac{\text{m}}{\text{s}} \right) = 0.0495245 \text{ kg/s}$$

$$\begin{aligned}
\dot{Q}_{\text{air}} &= \dot{m}_a c_{p,a} (T_{\text{out}} - T_{\text{in}}) \\
&= 0.0495245 \frac{\text{kg}}{\text{s}} 1006.873 \frac{\text{J}}{\text{kgK}} (24.52643 - 21.67786)^\circ\text{C} \\
&= 142.0436 \text{ W}
\end{aligned}$$

When the heat transferred to the environment is compared,

$$\begin{aligned}
\dot{W}_{\text{comp}} + \dot{Q}_L + \dot{Q}_{\text{post heater}} - \dot{Q}_{\text{cond,a}} &= \\
142.46 - 142.0436 \text{ W} &= 0.4163934 \text{ W} \\
\text{Deviation} &= \frac{|142.46 - 142.0436| \text{ W}}{142.46 \text{ W}} = 0.29228\%
\end{aligned}$$

The deviation is found surprisingly low because air velocity measurements involve uncertainty and depend on the assumption of average temperature. Similarly temperature readings involve uncertainty. As the temperature difference between air inlet and outlet is 2.85°C , and if the sensitivity of thermocouples is considered, this deviation is quite small.

4.3 Uncertainty Analysis

Uncertainty analysis is based on expected uncertainty method. It is basically, taking the square root of summation of squares of relative uncertainties of each variable.

$$\delta Q = \left[\left(\frac{\partial Q}{\partial x_1} \delta x_1 \right)^2 + \left(\frac{\partial Q}{\partial x_2} \delta x_2 \right)^2 + \dots \right]^{1/2} \quad (4.9)$$

In Eq. (4.9), Q is the symbol of the parameter whose uncertainty is being calculated. Symbols x_1 and x_2 are the variables.

Uncertainty in the measured parameters are presented in Table 4.6.

Table 4.6 Uncertainty of direct measurements. Some data is obtained from [4]

Measurement	Uncertainty
V (V)	$\pm 0.01\%$
I (A)	$\pm 0.01\%$
W (μm)	± 10
L (μm)	± 20
H_c (μm)	± 20
w_c (μm)	± 20
T_{base} ($^{\circ}\text{C}$)	± 0.5
T_{sat} ($^{\circ}\text{C}$)	± 0.5
u_{air} (m s^{-1})	$\pm 5\%$
P_{in} (bar)	± 0.1
P_{out} (bar)	± 0.1

In the present study, uncertainties in T_{base} , h_{av} , COP , COP_{rev} and η_{II} are calculated.

For calculating average heat transfer coefficient in the channels, the base temperature, T_{base} should be calculated as the measured temperature is 2 mm under the base. Uncertainty related to the distance between base and the thermocouple is thought to be important as the distance is very small and may cause big deviations in calculating the base temperature. Using Fourier's law equation and assuming uniform heat flux, uncertainty of δT_{base} is calculated.

$$\delta T_{\text{base}} = \left[(\delta T_{\text{m}})^2 + \left(\frac{-x}{k} \delta q'' \right)^2 + \left(\frac{-q''}{k} \delta x \right)^2 \right]^{1/2} \quad (4.10)$$

After calculating the uncertainty δT_{base} , the uncertainty in h_{av} can be calculated.

$$\begin{aligned} & \delta h_{\text{av,a}} \\ &= \left[\left(\frac{-\dot{Q}_{\text{evap}} (2 \eta_{\text{f}}) \delta H_{\text{c}}}{(T_{\text{base}} - T_{\text{sat}}) n_{\text{channel}} L (2 \eta_{\text{f}} H_{\text{c}} + w_{\text{c}})^2} \right)^2 \right. \\ &+ \left(\frac{-\dot{Q}_{\text{evap}} \delta w_{\text{c}}}{(T_{\text{base}} - T_{\text{sat}}) n_{\text{channel}} L (2 \eta_{\text{f}} H_{\text{c}} + w_{\text{c}})^2} \right)^2 \\ &+ \left(\frac{-\dot{Q}_{\text{evap}} \delta T_{\text{base}}}{(T_{\text{base}} - T_{\text{sat}})^2 n_{\text{channel}} L (2 \eta_{\text{f}} H_{\text{c}} + w_{\text{c}})} \right)^2 \\ &+ \left(\frac{\dot{Q}_{\text{evap}} \delta T_{\text{sat}}}{(T_{\text{base}} - T_{\text{sat}})^2 n_{\text{channel}} L (2 \eta_{\text{f}} H_{\text{c}} + w_{\text{c}})} \right)^2 \\ &+ \left(\frac{\delta \dot{Q}_{\text{evap}}}{(T_{\text{base}} - T_{\text{sat}}) n_{\text{channel}} L (2 \eta_{\text{f}} H_{\text{c}} + w_{\text{c}})} \right)^2 \\ &\left. + \left(\frac{-\dot{Q}_{\text{evap}} \delta L}{(T_{\text{base}} - T_{\text{sat}}) n_{\text{channel}} L^2 (2 \eta_{\text{f}} H_{\text{c}} + w_{\text{c}})} \right)^2 \right]^{1/2} \quad (4.11) \end{aligned}$$

In uncertainty calculations of h_{av} , η_{f} is taken as constant. The main uncertainty sources are temperatures, this is why relative uncertainty effect of η_{f} is neglected.

$$\begin{aligned}
\delta COP = & \left[\left(\frac{\delta \dot{Q}_{\text{evap}}}{I V - \dot{W}_{\text{fan,comp}}} \right)^2 + \left(\frac{\dot{Q}_{\text{evap}} V \delta I}{(I V - \dot{W}_{\text{fan,comp}})^2} \right)^2 \right. \\
& + \left(\frac{\dot{Q}_{\text{evap}} I \delta V}{(I V - \dot{W}_{\text{fan,comp}})^2} \right)^2 \\
& \left. + \left(\frac{-\delta \dot{W}_{\text{fan,comp}}}{(I V - \dot{W}_{\text{fan,comp}})^2} \right)^2 \right]^{1/2}
\end{aligned} \tag{4.12}$$

I and V are current and voltage values read for cartridge heaters. $\dot{W}_{\text{fan,comp}}$ is the fan power used to cool down the compressor.

$$\delta \dot{W}_{\text{fan,comp}} = \sqrt{(V \delta I)^2 + (I \delta V)^2} \tag{4.13}$$

$$\begin{aligned}
\delta \text{COP}_{\text{rev}} = & \left[\left(\delta T_c \left(\frac{1}{T_h - T_c} + \frac{T_c}{(T_h - T_c)^2} \right) \right)^2 \right. \\
& \left. + \left(\frac{-T_c \delta T_h}{(T_h - T_c)^2} \right)^2 \right]^{1/2}
\end{aligned} \tag{4.14}$$

$$\delta \eta_{\text{II}} = \left[\left(\frac{\delta \text{COP}}{\text{COP}_{\text{rev}}} \right)^2 + \left(\frac{-\text{COP} \delta \text{COP}_{\text{rev}}}{\text{COP}_{\text{rev}}^2} \right)^2 \right]^{1/2} \tag{4.15}$$

The air velocity through the condenser is another important parameter in terms of performing energy balance for the cycle. Air velocity is measured at 9 different locations at the cross section of the duct.

$$\delta u_a = \left[\frac{\sum_{n=1}^9 (\delta u_{a,n})^2}{81} \right]^{1/2} \quad (4.16)$$

The heat loss from the condenser is critical for checking the energy balance for the cycle. Its uncertainty can be calculated as

$$\begin{aligned} \delta \dot{Q}_{\text{cond}} = & \left[(A_c \rho C_{p,a} (T_{\text{out}} - T_{\text{in}}) \delta u_a)^2 \right. \\ & + (u_a A_c \rho C_{p,a} \delta T_{\text{out}})^2 \\ & \left. + (-u_a A_c \rho C_{p,a} \delta T_{\text{in}})^2 \right]^{1/2} \end{aligned} \quad (4.17)$$

Pressure drop uncertainty is related to pressure measurements at the inlet and outlet of the evaporator or condenser.

$$\delta \Delta P = \sqrt{\delta P_{\text{in}} - \delta P_{\text{out}}} \quad (4.18)$$

q''_{base} is based on the area of ($L \cdot W$) and its uncertainty is reported to be 0.1% [4].

The measurement uncertainty for the sensors, measuring devices and the reported results were listed in Table 4.6. The uncertainty in some calculated parameters are given in Table 4.7.

Table 4.7 Uncertainty results of calculated parameters. Some data is obtained from [4]

Parameter	Uncertainty
q''_{base}	0.1%
\dot{W}_{fan}	$\pm 0,002 \text{ W}$
h	for $\dot{Q}_{\text{evap}} = 10 \text{ W}$, $\delta h = 109\%$
	for $\dot{Q}_{\text{evap}} = 20 \text{ W}$, $\delta h = 60\%$
	for $\dot{Q}_{\text{evap}} = 30 \text{ W}$, $\delta h = 15.14\%$
	for $\dot{Q}_{\text{evap}} = 40 \text{ W}$, $\delta h = 4.6 - 20\%$
	for $\dot{Q}_{\text{evap}} = 50 \text{ W}$, $\delta h = 9.31\%$
	for $70 \text{ W} > \dot{Q}_{\text{evap}} > 60 \text{ W}$, $7 \leq \delta h \leq 10.25\%$
	for $80 \text{ W} \geq \dot{Q}_{\text{evap}} \geq 70 \text{ W}$, $3.9 \leq \delta h \leq 8.6\%$
	for $80 \text{ W} > \dot{Q}_{\text{evap}} > 90 \text{ W}$, $4.4 \leq \delta h \leq 8\%$
ΔP	for $\dot{Q}_{\text{evap}} \geq 90 \text{ W}$, $3.66 \leq \delta h \leq 7.27\%$
	1.4 kPa
COP	$\leq 0.11\%$
COP_{rev}	for $\dot{Q}_{\text{evap}} \leq 40 \text{ W}$, $\delta \text{COP}_{\text{rev}} \leq 26\%$
	for $\dot{Q}_{\text{evap}} > 40 \text{ W}$, $9 \leq \delta \text{COP}_{\text{rev}} < 15\%$
η_{II}	for $\dot{Q}_{\text{evap}} \leq 40 \text{ W}$, $\delta \eta_{\text{II}} \leq 26\%$
	for $\dot{Q}_{\text{evap}} > 40 \text{ W}$, $11 \leq \delta \eta_{\text{II}} < 21\%$

Maximum value of uncertainties are given among many data points for the specified condition.

4.4 Experimental Results

In the experimental part of the study, it is aimed to test the performance of the cycle. COP, COP_{rev} , and η_{II} are calculated. Individual parts of the cycle are examined as well. Average heat transfer coefficient of the cycle has been calculated in the evaporator

part. Effects of the refrigerant load, condenser fan speed, saturation temperature, compressor power on the cycle and heat transfer performance are investigated.

In Figure 4.7, COP and second law efficiency are depicted for various compressor and cooling loads.

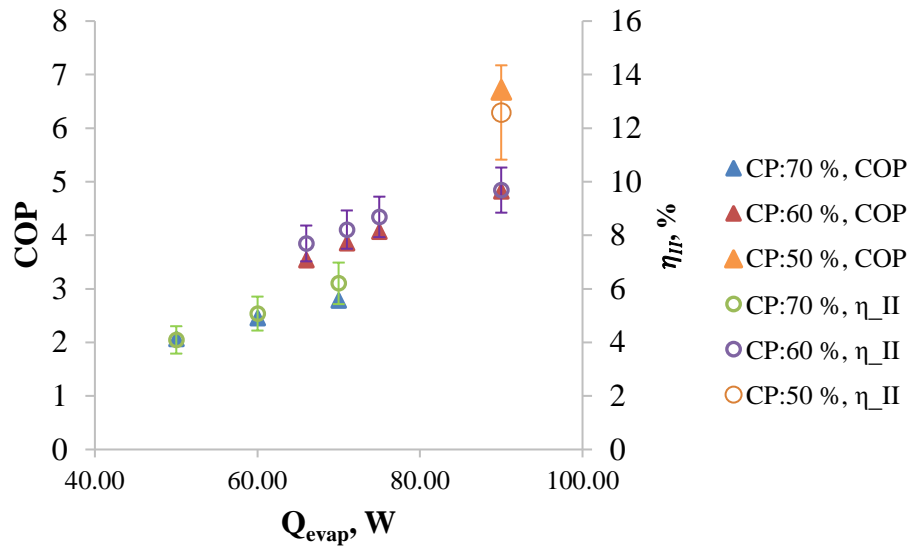


Figure 4.7 Variation of COP and η_{II} with \dot{Q}_{evap} at different CP, RC= 64 g, FS = 1

In Figure 4.7, with the increase of \dot{Q}_{evap} , COP also increases. The reason is that while the compressor power stays the same heat removed from the cold side increases. Similar performance characteristics have been observed for η_{II} as well. The hot and cold side temperatures do not show significant difference with the increase of \dot{Q}_{evap} so COP is the important factor when calculating the second law efficiency. Another important thing to be inferred from Figure 4.7 is that increasing the compressor power does not result in increase in COP. Although the refrigerant mass flow rate increase with the increased compressor power, heat removal from the cold side cannot be increased so much because of the instabilities in the cycle. For this reason, the results

for compressor powers higher than 70% have not been presented. The cycle performs the best for the compressor power of 50%. At high compressor powers compressor struggles to pressurize the fluid and fluctuations in mass flow rate have been observed also. Increasing the compressor power reduces the COP and also causes instabilities in the cycle. Because of these reasons, most of the experiments have been conducted at 50% compressor power. COP and second law efficiency are inspected in terms of saturation temperature and results are given in Figure 4.8.

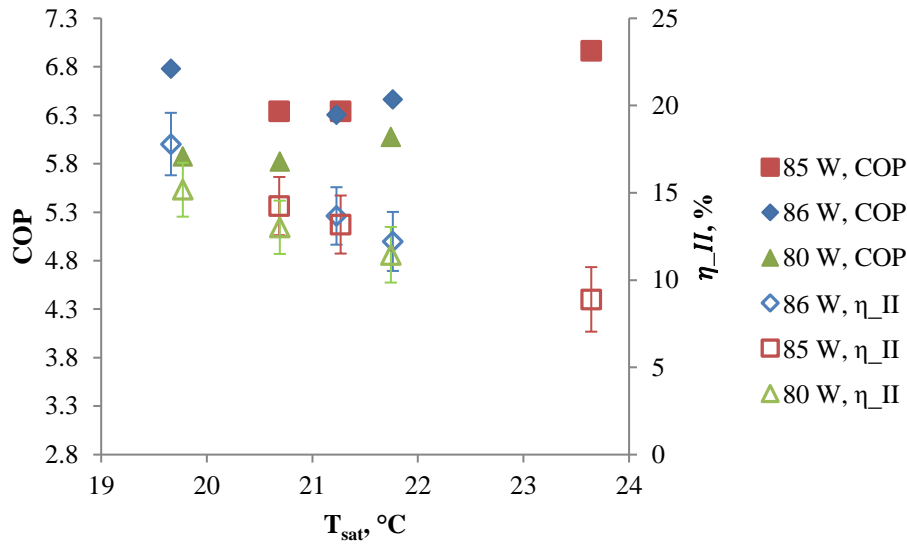


Figure 4.8 Variation of COP and η_{II} with T_{sat} at different \dot{Q}_{evap} , CP = 50%, RC = 64 g, FS = 1

Each data series in Figure 4.8, has almost constant COP. Deviation in COP is due to the small changes in the compressor power. Although the compressor power is adjusted to be constant from the software, electricity consumption of the compressor may show small fluctuations depending on the flow characteristics for different cases. It has been observed that for higher saturation temperatures, lower second law efficiencies are obtained. The reason why the second law efficiency decreases is that

while the hot side temperature stays almost constant, saturation temperature increases for the cold side. The same data have been demonstrated in terms of base temperature and average heat transfer coefficient in Figure 4.9.

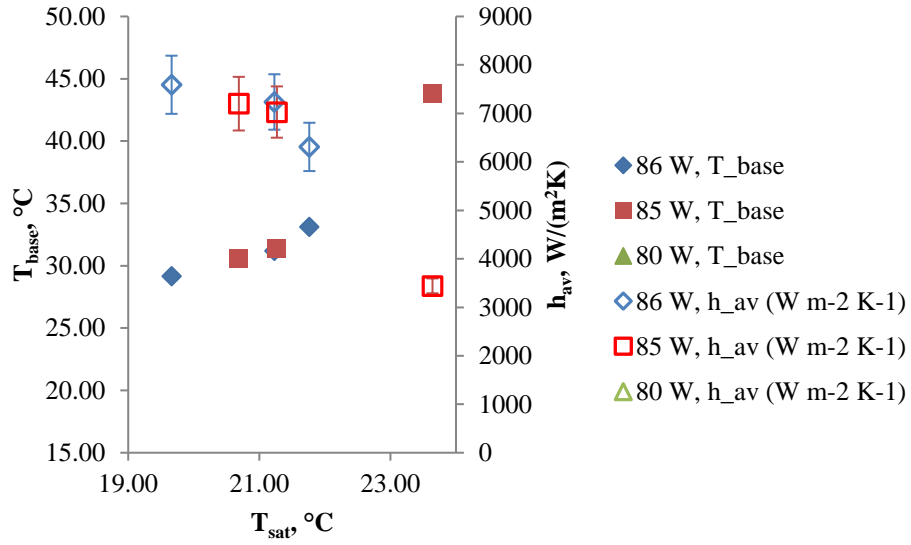


Figure 4.9 Variation of T_{base} and h_{av} with T_{sat} for different \dot{Q}_{evap} , CP = 50%, RC = 64 g, FS = 1.

Nothing surprising is observed in Figure 4.9. The base temperature increased with the increase in saturation temperature but the base temperature increases sharply for the saturation temperature of 23.6°C. Similarly, the average heat transfer coefficient decreases dramatically for that saturation temperature. It has been observed during the experiments that the cycle has a tendency to result in burnout when the saturation temperature is high. It was more preferable to work in lower saturation temperatures in the evaporator. This situation might stem from higher inlet vapor qualities for higher saturation temperatures.

The base temperature and average heat transfer coefficient variation at different cooling loads are given in Figure 4.10.

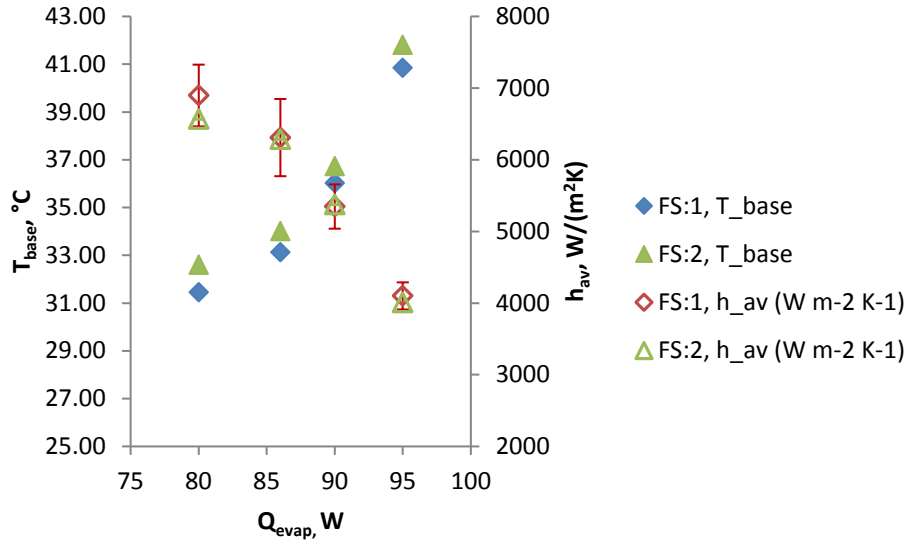


Figure 4.10 Variation of T_{base} and h_{av} with \dot{Q}_{evap} at different FS, $T_{sat} \cong 21.5^{\circ}\text{C}$, CP = 50%, RC = 64 g

Independent of the fan speed, the base temperature increased with an increase in the cooling load. Although the saturation temperature is desired to be constant, it is not possible to fix it at a constant value. It is around 21.5°C and only deviates $\pm 0.5^{\circ}\text{C}$ for all cases in Figure 4.10. It was expected to have higher average heat transfer coefficients for higher fan speeds but they are almost constant for both fan speeds at constant cooling loads. With increased fan speed, the refrigerant should have lower vapor qualities at the condenser inlet compared to the other case. This means lower inlet vapor qualities at the evaporator inlet. However, having lower vapor quality at the evaporator inlet has not lead to higher heat transfer coefficients. We can conclude that the evaporator outlet vapor qualities are not at critical levels for both of the fan speeds. Otherwise, the average heat transfer coefficient would deviate between the two cases. However, higher cooling loads than 95 W could not be reached. If it is tried, the base temperature starts to increase suddenly and has tendency to experience

burnout quickly. This burnout happens due to the rapid growth of vapor bubble and the thin liquid film between the channel surface and the vapor bubble disappears. As vapor bubble dominates the channel cross section, heat transfer coefficient reduces abruptly and the base temperature increases. Although the vapor quality is not at a critical level, evaporator is likely to experience burnout. The reason behind this is stability. Stability is a very important issue in microchannels because parallel channels create an effect similar to upstream compressibility for each channel [46]. In order to stabilize the flow, a pressure drop element might be implemented at the inlet of the channels or a needle valve might be placed before the channels. By doing so, reverse flow can be prevented and a more stable flow is obtained. The present experimental set up can be improved in that sense. If the experimental set up were stabilized, it is likely to remove 150 W from the evaporator with the current configuration.

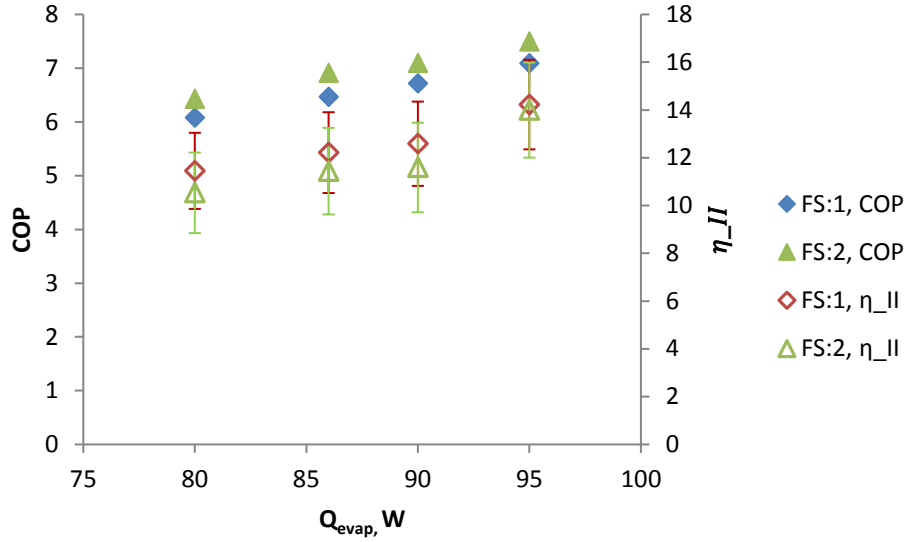


Figure 4.11 Variation of COP and η_{II} with \dot{Q}_{evap} for different FS, CP = 50%, RC = 64 g

If Figure 4.11 is examined, a small variation is observed between the COP's for the fan speeds at constant cooling load. Although the compressor power is the same, there is a small deviation in its electricity consumption. Varying the fan power changes the inlet and outlet vapor qualities of the evaporator. The variation in the electricity consumption of the compressor can be attributed to the state of the refrigerant. It is most likely related to the temperature and density of the superheated refrigerant at the compressor inlet. For the higher fan speed (FS=2), compressor's power consumption is lower so the condensation temperature is lower than the other case. Therefore, the second law efficiency is lower for the cases with high air mass flow rate.

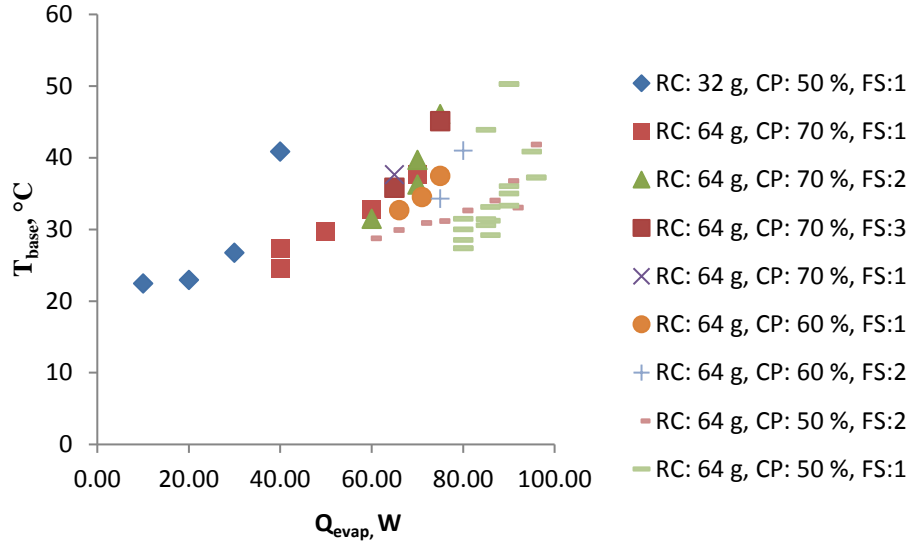


Figure 4.12 Variation of T_{base} with \dot{Q}_{evap} for different cases

Almost all of the experimented cases are presented in Figure 4.12. The maximum base temperature has been observed as 50°C. The temperature around the cartridge heaters easily reaches 65°C if the base temperature is considered to be 50°C (Distance between the base and the closest point of the cartridge heater is 19 mm). In Figure 4.12, experiment results for 32 g gas load are given. Higher cooling loads could not be reached at that charge at that charge. The refrigerant pressure in the tank allowed 64 g gas charge in the cycle. It might be possible to charge the cycle with more refrigerant by heating the refrigerant tank but caution should be taken to avoid possible danger. Results show that more heat can be removed from the evaporator with more refrigerant charges. At higher compressor speeds (CP: 70%), a maximum of 75 W heat could be removed and the base temperature was at critical levels at that load as can be seen from Figure 4.12. Increasing the fan speed could not help on removing more heat from the evaporator but it was beneficial to increase the COP and keeping the base temperature

at lower levels. Similarly, the heat transfer coefficient variation is depicted for many cases in Figure 4.13.

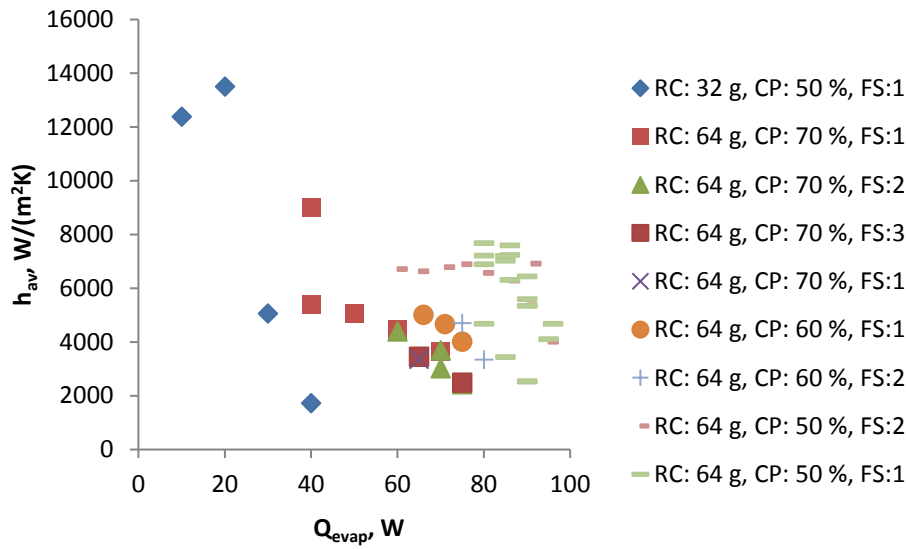


Figure 4.13 Variation of h_{av} with Q_{evap} for different cases

Although the heat transfer coefficient seems to be relatively high for lower cooling loads, the expected uncertainty is quite high. As the temperature difference is very small between base and the refrigerant, error in temperature readings leads to high uncertainties.

4.5 Performance Comparison of the Present Study with the Literature

Current literature was summarized in Table 1.1. In this part, more information is going to be presented in terms of the performance of the cycles available in the literature. Although it is hard to make reasonable comparison as each miniature vapor compression refrigeration cycles has its own design and characteristics, some parameters are going to be compared and discussed. The main parameters to be discussed are, the cooling capacity, COP of the cycle, second law efficiency and

evaporator dimensions. Table 4.8 compares the performance parameters of the present study and available MVCRC's available in the literature.

Table 4.8 Performance parameters of MVCRC's available in the literature and present study

	$\dot{Q}_{\text{evap}}, \text{ W}$	COP	η_{II}	Evaporator Dimensions
Yuan et al. [5]	260	1.61	0.324	$H_c = 0.35 \text{ mm}$, $w_c = 0.35 \text{ mm}$ $n_{\text{channel}} = 39 \times 26$, $L = 22.3 \text{ mm}$,
Wu and Du [6]	200	8.6	0.3	$H_c = 4 \text{ mm}$, $w_c = 0.5 \text{ mm}$ $n_{\text{channel}} = 60$, $L = 57 \text{ mm}$.
Mongia et al. [8]	45	3.65, at 35 W, 2.25 at 45 W	0.31	$w_c = 0.08 \text{ mm}$ $L \cong 3 \text{ mm}$.
Yu-Ting, et al. [2]	300	2.3		Not a microchannel structure.
Trutassnavin et al. [7]	121-268	2.8-4.7	0.33- 0.52	$H_c = 2.3 \text{ mm}$, $w_c = 0.8 \text{ mm}$ $n_{\text{channel}} = 41$, $L = 19 \text{ mm}$.
Mancin et al. [9]	37-374	1.04-5.08		$L = 4 \text{ mm}$.
Present Study	96	7.71, at 96 W	0.136	$H_c = 0.7 \text{ mm}$, $w_c = 0.25 \text{ mm}$ $n_{\text{channel}} = 40$, $L = 19 \text{ mm}$.

When the present study is compared with the other MVCRC's, the cooling load seems to be lower. This is related to the evaporator heat transfer area. If the microchannel dimensions are compared, Yuan et al. [5], Mongia et al. [8] and present study can be accounted as "micro" because other evaporators have greater dimensions than 1 mm for the channel height, H_c and channel width w_c . The length of the channel is also

important in terms of cooling load but the cross sectional dimensions are so critical to provide the stability. Smaller hydraulic diameters lead to burnout more easily. If the channel dimensions in the present study are considered, dissipated heat seems to be reasonable. For the maximum cooling load of 96 W, the mass flow rate is measured to be 1.2 g/s. This correspond to approximately 0.44 vapor quality increase between the evaporator inlet and outlet. As the inlet vapor quality is around 0.2, this corresponds to an outlet vapor quality of 0.64. After improvements regarding stability, the outlet quality may reach the value of 0.8 with increased cooling load. On the other hand, the present MVCRC performs pretty well in terms of its high COP of 7.71.

4.6 Comparison of Experiment Results with Theory

Experimental results have been compared with theoretical calculations based on the evaporator and condenser design chapters. Pressure-enthalpy diagram is given in Figure 4.14 for the inspected case in this part. Evaporator, condenser and compressor powers are presented in Figure 4.14.

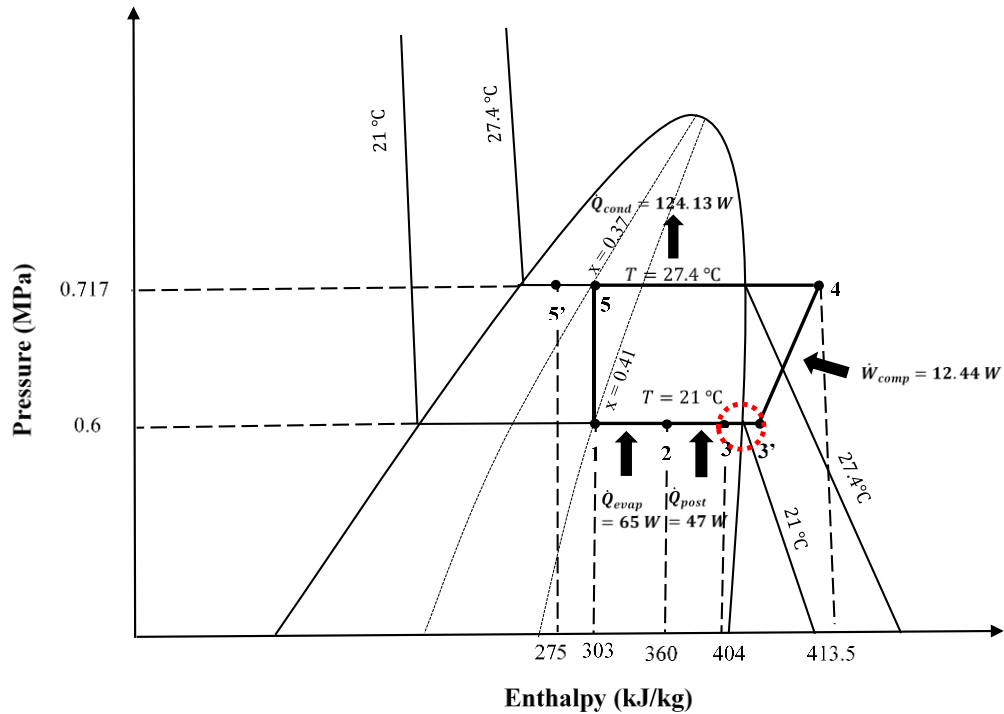


Figure 4.14 P-h diagram of the refrigeration cycle for this part

Diagram is drawn by fixing state 4, and by performing an energy balance, state 5 is found. State 5' is the state found according to the condenser air side heat transfer rate. Condenser load according to the air side energy balance is approximately 154 W. As the heat dissipated in condenser cannot exceed the summation of work and heat sources in the cycle, summation of these sources is used, 124.13 W. State 1 is found with the assumption of constant enthalpy through the expansion valve. Other states are determined according to evaporator, post heater and compressor powers. Mass flow rate through the cycle is measured as 1.1 g/s. According to the calculations, compressor entrance is state 3 though it should be in the gas phase. Therefore, there might be error in mass flow rate or energy balance due to heat gains. The possible compressor inlet state is therefore within the region marked by a red dashed circle. The deviation is just

a few watts. The cycle is examined component by component and results are compared with theoretical calculations.

T-s diagram is given in Figure 4.15 for the same states given in Figure 4.14.

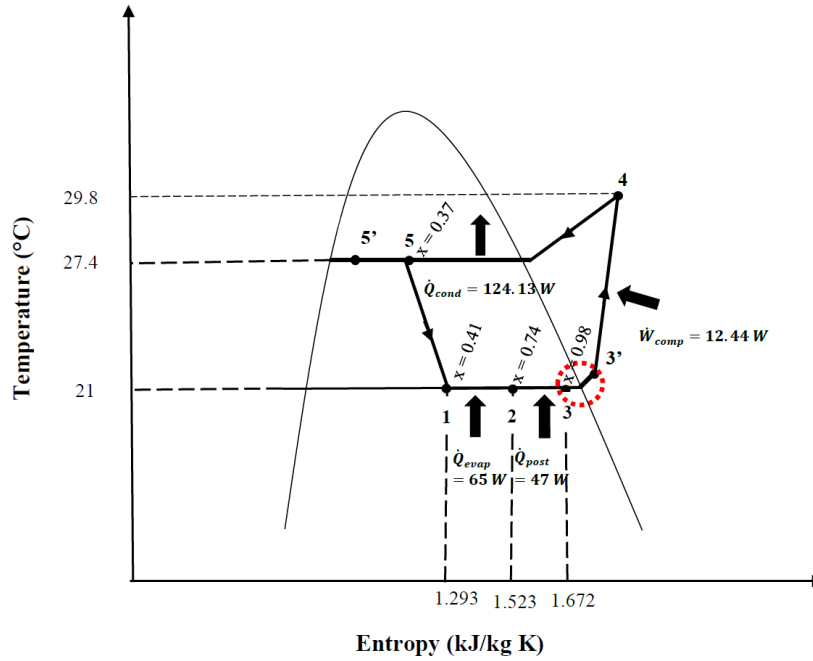


Figure 4.15 T-s diagram of the refrigeration cycle for this part

Firstly, the evaporator results are compared for a specific case. The inspected case is summarized in Table 4.9,

Table 4.9 Input parameters for the inspected case

\dot{Q}_{evap}	65 W
$T_{\text{sat, evap}}$	21°C
x_{in}	0.4103
x_{out}	0.736
\dot{m}_{ref}	1.1 g s ⁻¹

According to the case stated in Table 4.9, some important parameters such as the, average heat transfer coefficient and base temperatures are compared. Theoretical calculations are conducted according to the correlations and methodologies mentioned in Evaporator Design (Chapter 2).

Table 4.10 Comparison of theoretical and experimental results for the evaporator

	Experimental	Theoretical
$h_{av}, \text{Wm}^{-2}\text{K}^{-1}$	6923.327	13093.58
$T_{\text{base,av}}, ^\circ\text{C}$	28.72	25.34
$S_{\text{gen}}, \text{W K}^{-1}$	0.0078323	0.00342303

According to the comparison in Table 4.10, the theoretical average heat transfer coefficient overestimates the experimental result. In association with heat transfer coefficient, base temperature of experimental case is approximately 3.4°C higher than the theoretical calculation. Uncertainty of heat transfer coefficient for this case is reported to be 9.42% when the uncertainty of T type thermocouple reading is 0.5°C. If the uncertainty of thermocouple reading is considered to be 1°C, uncertainty is found to be 18.21%. In addition thermocouples are mounted 2 mm underneath the base. In uncertainty analysis for the average heat transfer coefficient, thermocouple placement error has been put into account. Error in this distance is considered as 5% but this error might be optimistic. Other than uncertainty, reason in the deviation of the average heat transfer coefficients between the two cases is thought to be instabilities in the experimental set up. It is important to note that heat transfer coefficient has also its own uncertainty. All of the heat provided by cartridge heaters may not reach the channels. Although heat loss to the ambient is very small, it should be noted as an error

source. Entropy generation rate is also compared according to the experimental measurements and theoretical calculation. Entropy generation rate is found to be approximately two times higher than the theoretical calculation mentioned in Chapter 2. Main reason of this is the base temperature. Segmentation calculation procedure in the theoretical calculation may lead to this deviation as well. Entropy generation rate calculation for experimental case has been made by using only one segment. That is only one base temperature is used in the calculations and pressure drop effect is neglected which is found to be 5% of the total entropy generation rate as a result of the theoretical calculation.

Present experimental results have been compared with Bertsch et al. [12]. Under almost the same mass flux, saturation temperature, hydraulic diameter and refrigerant, average heat transfer results are compared. Comparison is depicted in Figure 4.16.

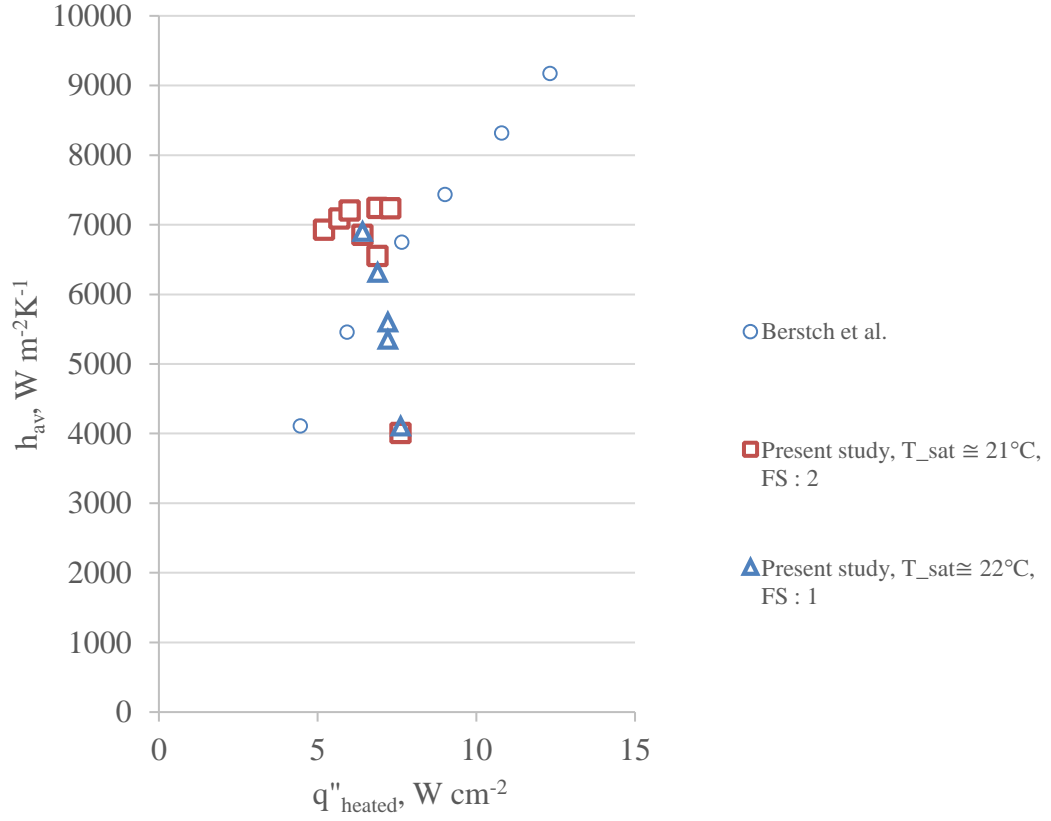


Figure 4.16 Comparison of Bertsch et al. [12] and experimental results of present study, Experimental conditions, [12], $P_{sat} = 550$ kPa, $T_{sat} \cong 20^{\circ}C$, $G = 167$ kg m⁻² s⁻¹.
Experimental conditions of the present study, CP : 50%, RC : 64 g.

In Figure 4.16, very good agreement is obtained for high heat fluxes but deviation increases for lower heat fluxes. As the uncertainty is very high for low cooling loads, lower values than 65 W for cooling loads is not presented. The lowest heat flux corresponds to $\dot{Q}_{evap} = 65$ W and the highest one corresponds to $\dot{Q}_{evap} = 95$ W for experimental results of the present study. A sudden decrease in the average heat transfer coefficient for the highest heat flux are observed for two cases of the present study. This means that for the maximum cooling load, 95 W, the system is unstable

and has a tendency to end up with burnout. It is observed that for an cooling load of 100 W the base temperature increased rapidly. Saturation temperature is very critical for the present study. Working with lower saturation temperatures is better in terms of stability and base temperature. However, the main reason behind why the results with fan stage: 1 underestimate Bertsch et al. [12]'s results is high vapor quality at the evaporator inlet. It should be noted that heat transfer is more favorable for lower vapor qualities. This can proved that when the base temperature along the channel is inspected. Base temperature difference between the inlet and outlet thermocouples reached 7°C for some cases. This created significant local heat transfer coefficient differences along the channel. Lower air mass flow rate in the condenser means higher vapor quality at the evaporator inlet. Experimental results may get excellent match if the inlet vapor qualities are equaled to those of with Bertsch et al. [12]. Local heat transfer coefficient variation may be found in Figure 4.17. Bertsch et al. [12] reached higher heat fluxes however the present study was able to dissipate 7.62 Wcm^{-2} as maximum. Stability is the main reason for the lower heat flux. Bertsch et al. [12]'s experimental set up is designed for examining only the evaporator part. They did not built a system for electronics cooling. It is not considered as a compact and portable cycle. They have subcooler and preheater section. Hence, they have more controllable set up and they can easily control evaporator inlet quality. They can adjust refrigerant's inlet quality at evaporator test section and they use a gear pump. It is much more difficult to provide stability for compact MVCRC. The hydraulic diameter in [12] was 0.54 mm, on the other hand, the evaporator in the current study has 0.368 mm hydraulic diameter. The present cycle has one of the smallest hydraulic diameters among the studies in the literature related to two phase flow boiling. Such a small diameter makes the things difficult regarding especially the stability. The liquid film inside the channel disappears earlier compared to high diameter channels. If higher outlet vapor qualities were reached, more heat could be dissipated. When considering the uncertainties in

the calculation of the average vapor quality, results depicted in Figure 4.16 are very promising.

Bertsch et al. [12] compared their experimental results with Kandlikar and Balasubramanian [50]'s. In Chapter 2 the correlation given in [50] is used and theoretical results were depicted in Table 4.10. According to the comparison between theoretical and experimental results, Kandlikar and Balasubramanian [50]'s correlation overestimates the experimental results of the present study. Bertsch et al. [12] did a similar comparison for a specific case similar to the one inspected in the present work. A comparison of the variation of heat transfer coefficient with local vapor quality is given in Figure 4.17.

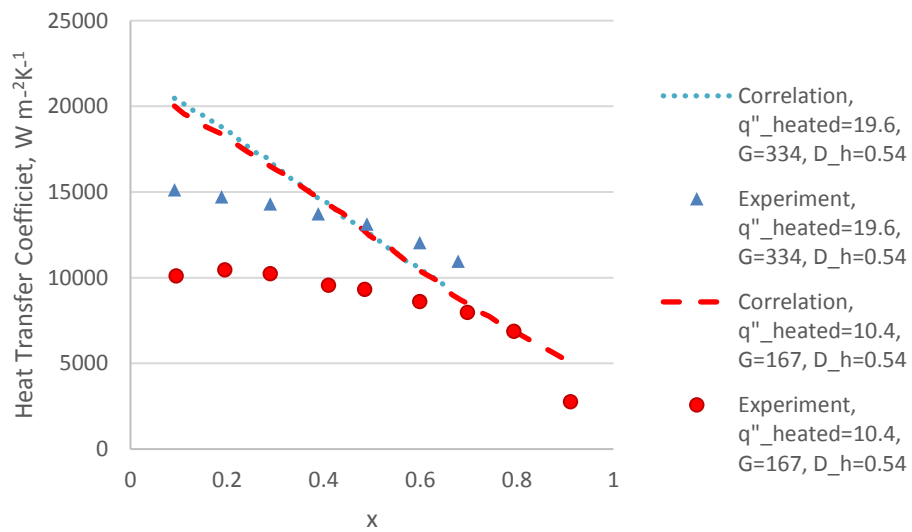


Figure 4.17 Comparison of the experimental [12] and theoretical [50] results,
units q''_{heated} : W cm $^{-2}$, G : kg m $^{-2}$ s $^{-1}$, D_h : mm

If Figure 4.17 is examined closely, the lower heat flux value ($q''_{\text{heated}} = 10.4$ W cm $^{-2}$) is very close to the experimental data of the present study. For that case, theoretical correlation overestimates experimental results of Bertsch et al. [12].

However, for the higher heat flux case a better agreement is obtained. If the results in Figure 4.16 and Figure 4.17 are examined, Bertsch et al. [12] has better agreement with the present experimental results. Kandlikar and Balasubramanian [50] overestimated present experimental data and Bertsch et al. [12]'s experimental data in the heat flux range of the present study. As the $q''_{heated} = 20.8 \text{ W cm}^{-2}$, and $\dot{Q}_{\text{evap}} = 130 \text{ W}$ which correspond to higher heat flux in Figure 4.17, the use of Kandlikar and Balasubramanian [50]'s study in evaporator design is justified.

For the condenser component, experimental results are compared with theoretical calculations as well. In theoretical calculations, multilouvered fin structure heat transfer correlation is used. However, the structure of the heat exchanger is similar to the one given in Figure 3.1. The main difference is that there are no louvers on fins of the heat exchanger used in the experiments. The fins can therefore be considered as plain fins. Dimensions are given in Table 4.3. As the multilouvered fin geometry is used in theoretical calculations, dimensions only related to louvers (L_α , L_p , L_l) are taken from Table 3.2. Condenser heat load given in Table 4.11 has been calculated according to the energy balance for the cycle ($\dot{W}_{\text{comp}} + \dot{Q}_{\text{evap}} + \dot{Q}_{\text{post heater}}$). This value should be equal to the air side heat transfer rate of the condenser. On the other hand, the air side heat transfer rate has been calculated as 154.57 W. As the uncertainty is lower for the evaporator, compressor and post heater loads, the condenser load calculated from energy balance 124.13 W is considered.

Table 4.11 Condenser parameters for comparison

\dot{m}_r	$1.1 \times 10^{-3} \text{ kg s}^{-1}$
\dot{Q}_{tot}	$\cong 124.13 \text{ W}$
\dot{Q}_{sp}	$\cong 2.59 \text{ W}$
\dot{Q}_{tp}	$\cong 121.54 \text{ W}$
$x_{\text{out,cond}}$	0.371
$P_{r,\text{in}}$	$\cong 0.717 \cdot 10^6 \text{ Pa}$
$T_{r,\text{in}}$	29.74°C
$T_{r,\text{sat}}$	$\cong 27.4^\circ\text{C}$
* $T_{a,\text{in}}$	22.12°C
* $T_{a,\text{out}}$	23.97°C
\dot{m}_a	$0.082805 \text{ kg s}^{-1}$
$\dot{Q}_{a,\text{exp}}$	154.57 W
n_{tube}	2
n_{pass}	4
$L_{\text{seg,sp}}$	0.5 mm
$L_{\text{seg,tp}}$	5 mm

*Experimental measurement, \dot{Q}_{tot} has been found from energy balance for the cycle.

Table 4.12 Comparison of the condenser length used in the experiments and found by louvered fin model.

$L_{\text{tot,multilouvered}}$ (theoretical)	115.5 mm
$L_{\text{tot,exp}}$	131 mm
Deviation	$\sim 11.83\%$

According to the length comparison in Table 4.12, theoretical calculation estimates 11.83% shorter length. The main reason behind this deviation is thought to be the multilouvered fin heat transfer coefficient used in the calculations for the air side. In Kim and Bullard [57], it is reported that for multilouvered fin geometry, heat transfer coefficient 25% higher compared to plain fin geometry. While the condenser heat load is calculated from cycle energy balance ($\dot{W}_{\text{comp}} + \dot{Q}_{\text{evap}} + \dot{Q}_{\text{post heater}}$) 124.13 W, it is calculated as 154.57 W from the air side energy balance. This difference originates from the temperature readings at the inlet and outlet of the condenser (Measurements are taken at the center of the cross section of the air duct. As the temperature difference is 3.7°C, and thermocouples have $\pm 1^\circ\text{C}$ uncertainty, this deviation is expected.

Another comparison is made between the experimental results and therefore results based on plain fin geometry using the same inputs given in Table 4.11. Plain fins are considered for simplicity (as there is no other suitable correlation) and the fins are assumed to be not tilted (air flows through rectangular channels). The onset of transition is assumed to occur at $Re_a \cong 2000$ for the air side. As there is no long calming section before the heat exchanger and because of the tube side structure in the heat exchanger, air does not enter the heat exchanger with fully developed velocity profile. Therefore, the use of turbulent flow heat transfer correlations is more reasonable. Dittus Boelter's equation is used to estimate Nusselt number.

$$Nu_D = 0.023 Re_a^{4/5} Pr_a^{0.4} \quad (4.19)$$

This correlation is valid for hydrodynamically and thermally fully developed, turbulent flow and smooth circular tubes. However, it is noted in [64] that use of this correlation for rectangular ducts is reasonable and can be used as an approximation for turbulent

flows and for $Pr_a \gtrsim 0.7$. Dittus Boelter equation has been developed for fully developed conditions $\left(\frac{L}{D} \gtrsim 10\right)$ and this ratio is approximately equal to 7. Hence, a correlation for the mean Nusselt number for thermally developing flow [65] is used.

$$\frac{Nu_m}{Nu_\infty} = 1 + \frac{C}{x/D_h} \quad (4.20)$$

and C is defined as

$$C = \frac{\left(\frac{x}{D_h}\right)^{0.1}}{Pr_a^{\frac{1}{6}}} \left(0.68 + \frac{3000}{Re^{0.81}} \right) \quad (4.21)$$

This correlation is valid for $x/D_h > 3$, $500 < Re < 10^5$ and $0.7 < Pr < 75$.

The heat exchanger length used in the experimental work and that estimated by the model with plain heat exchanger geometry are provided in Table 4.13.

Table 4.13 Comparison of the condenser length used in the experiments and found by plain fin model.

$L_{tot,plain}$ (plain fin geometry)	137.75 mm
$L_{tot,exp}$	131 mm
Deviation	~ 5.1%

According to the comparison depicted in Table 4.13, theoretical calculation overestimated the heat exchanger length by approximately 5% which is an excellent match. However, the theoretical result should be considered as an approximation

because there are some assumptions such as smooth surface, rectangular fin geometry, the onset of the transition regime. Although it is a rough estimation, experimental result and theoretical result match very well when the uncertainties in the experimental set up are considered. The major uncertainty is in the air mass flow rate with $\pm 5\%$. If the air mass flow rate given in the Table 4.11 were taken 5% higher, heat exchanger length is calculated to be 132 mm which almost the same value with the present configuration. Another important reason for the deviation is the condenser load. It is calculated as the summation of cooling load, post heater and compressor power. Even though it is very small, there should be heat loss from the system. Therefore, heat exchanger length may get closer if the calculations were conducted with lower condenser loads. Although fin surfaces can be assumed to be smooth, the surface that the fins are brazed is quite rough. As the most heat transfer surface area belongs to the fins, all surfaces that the air flows through are assumed to be smooth. Considering that the increase in friction factor increases the heat transfer coefficient, the present results may get closer if the surface roughness is taken into account. Results also show that it is necessary to consider developing flow effect, otherwise the results would deviate more. It should be noted that air does not enter the heat exchanger smoothly. Air hits the tube side of the heat exchanger and then enters the heat exchanger. This promotes turbulence [66]. In literature the constant, C in Eq. (4.20) is taken as 6 [66] (abrupt contraction entrance for circular tubes) and similar Nu_m is calculated (under 17% dev. in Nu_m). Although it is for circular tubes, this correlation also shows the importance of developing flow entrance configuration effect. To conclude, theoretical calculation for plain fins matches very well with the experimental results.

CHAPTER 5

CONCLUSIONS AND FUTURE RECOMMENDATIONS

5.1 Evaporator

An entropy generation rate analysis has been performed for a micro evaporator to be used in a MVCRC. Intel core i7 processor has been considered as a contemporary reference electronic device to be cooled, and the cooling load and main dimensions have been determined accordingly. The entropy production has been monitored while changing the channel height and width, the heat flux, the mass flow rate and mass flux, the outlet vapor quality, and the saturation temperature. In the given range of parameters, the entropy generation rate increased with increasing heat flux and also with the corresponding mass flow rate for constant outlet vapor quality. On the other hand, the increased channel height decreased the entropy generation rate. With lower channel heights, the heat transfer per unit area (sides and bottom surfaces) increases which results in increased wall temperatures (sides and bottom) and also high entropy generation rates. For this reason, the channel height should be kept as high as the available volume permits. In two-phase evaporation in microchannels, determining the outlet vapor quality is one of the major challenges because after a certain value of the vapor quality, the base temperature sharply increases and may cause dry out. A safe value of the vapor quality giving the minimum entropy generation rate may be provided to be around 0.85, keeping in mind that it is dependent on the channel height. For lower channel heights, the entropy generation rate due to pressure drop gains importance and the optimum outlet vapor quality drops to lower values. For taller

channels (800, 900 and 1000 μm), the optimum outlet vapor quality levels out at the value of 0.878. One of the most important findings from the analysis is that lower channel widths yield lower entropy generation rate.

The present study is the first application of dimensional optimization for two-phase flow in microchannels. Entropy generation rate has been the objective function with the channel width and the wall thickness being the design variables. The optimum channel width varied between 63-82 μm depending on the channel height and the flow rate. The optimum fin thickness has been evaluated as 50 μm except for the tallest channels ($H = 700 \mu\text{m}$) at low mass flow rates of 0.95, 1 and 1.05 g s^{-1} where relatively lower pressure losses enabled the use of thicker fins, and narrower channels. The maximum temperature has been kept safely far from the critical limits of operation. Heat transfer was found to be the major source of the total entropy production for 200-400 μm wide channels. On the other hand, the contributions of heat transfer and pressure drop become comparable for the optimized (narrower) channels. To conclude, the present entropy generation minimization study can conveniently be used for obtaining the optimum dimensions, and vapor outlet qualities of a micro evaporator to yield the best performance in terms of the heat transfer and the pressure drop.

5.2 Condenser

The entropy generation number in the microchannel condenser component of MVCRC has been investigated as a function of various parameters such as the air mass flow rate, fin pitch, fin height, louver angle, and hydraulic diameter. The effects of the investigated parameters on the heat exchanger length have also been presented.

The mass flow rate of air has been assessed to be the most important parameter in determining the entropy generation number, and also the length of the heat exchanger.

An air mass flow rate of 0.08 kg s^{-1} and a corresponding fin pitch of 1.3 mm have been determined as the optimal values yielding the minimum entropy generation number. Another reason for selecting this air mass flow rate is that it is a safe value in terms of fan reliability while still providing the flexibility of temporarily increasing the fan speed on demand. In addition, by using the suggested design, a moderate heat exchanger length has been obtained. On the other hand, it has been shown that the fin height did not have a significant effect on the entropy generation number compared to the fin pitch. An optimal path is offered for the refrigerant side hydraulic diameter ($\alpha_c = 1$) and the air mass flow rate. For the predetermined 0.08 kg s^{-1} air mass flow rate, the optimal hydraulic diameter has been found to be $500 \text{ }\mu\text{m}$ as used in the study. The louver angle did not have a substantial effect on the entropy generation number; however, it is appropriate to use it within the air mass flow rate range of $0.07\text{-}0.11 \text{ kg s}^{-1}$.

It has been observed that with the increase in the mass flow rate of air, while the entropy generation number due to air pressure drop increases, it decreases due to improved heat transfer. The heat exchanger length has been calculated to be shorter for higher air mass flow rates. In this case, the heat exchanger is more compact, the heat transfer is more effective, although the pressure drop due to air flow is higher. Beyond a certain mass flow rate of air, the total entropy generation number starts to increase because of the dominance of the contribution of the pressure drop on the air side. For the fixed dimensions given in the study, the optimum air mass flow rate has been found to be 0.08 kg s^{-1} .

The study is unique in the literature in carrying out an entropy generation minimization for two-phase flow in a microchannel condenser.

The entropy generation number maps provided in the present study are believed to be useful for researchers in designing microchannel heat exchangers for similar operation.

5.3 Experiments

Critical parameters, COP, η_{II} and \dot{Q}_{evap} , of MVCRC are assessed. A maximum COP value of 7.71 is obtained under 96 W cooling load which is the maximum load that 96 W could be removed from the cold side of the cycle. The base temperature of the evaporator increased rapidly when 100 W of heat is applied to the evaporator. More heat could be removed from the evaporator if the gas charge is increased. Pressure in the R134a gas tank allowed 64 g gas load in the cycle. If the gas pressure in the gas tank is increased, gas charge in the cycle might be increased. In most of the MVCRC's in the literature, evaporator channel diameter are higher than 1 mm. Only a few evaporators in the literature can be called micro evaporator. When the dimensions of the channel diameters is considered (rectangular $500 \times 500 \mu\text{m}$), the removed heat is quite satisfactory. More heat can be removed if the stability of the system is ensured. Some modifications on the geometry have been made for the sake of stability of the system in the literature. For example, by putting restriction in the evaporator inlet, small pressure fluctuations and back flows are prevented. If some modifications are done on the evaporator geometry, the cooling capacity can be increased easily. For example, under 96 W evaporator cooling load, refrigerant mass flow rate is measured to be 1.2 g s^{-1} . This case corresponds to 0.44 vapor quality increase. If the evaporator inlet quality is considered to be 0.2, outlet vapor quality is 0.64 with present configuration. After maintaining stability, heat transfer will be more effective at higher outlet qualities so vapor qualities 0.8 at the outlet can be reached. Increasing the diameter of the channels may help obtain a stable flow. The average heat transfer coefficient calculated according to experimental measurements is found to be lower ($\cong 47\%$) when compared to the results obtained by the results obtained by the correlation [50] used in Chapter 2. This deviation can be attributed to unstability of the flow. It is important to note that uncertainty of average heat transfer coefficient is calculated to be 18.8% for this case. Distance uncertainty related to the location of the

thermocouples is taken as 5% but it might be higher than that. If the 5% error (distance error) related to location of the thermocouples is increased, it will create additional uncertainty of average heat transfer coefficient which was reported to be 18.8%. The mentioned correlation has its own error as well.

Although Kandlikar and Balasubramanian [50]'s correlation overestimated the experimental results of the present study, a relatively good match is obtained with Bertsch et al. [12]'s experimental findings. Kandlikar and Balasubramanian [50]'s correlation matches well with Bertsch et al. [12]'s results for high heat fluxes but it overestimates the heat transfer coefficient for lower heat fluxes. As the operational conditions and the channel dimensions of the experiments are almost the same with those in Bertsch et al. [12], experimental results of the present study makes sense and the deviation is below the uncertainty range.

Heat exchanger lengths results have been also compared with theoretical calculations. The length estimated by the theoretical calculation based on multilouvered fin correlation is approximately 12% shorter than the condenser length used in the set up. This result was expected because multilouvered fin structure is more efficient in terms of heat transfer. In Kim and Bullard [57], it is reported that multilouvered fin geometry heat transfer coefficient has been found 25% higher than that for plain fin geometry. In addition, using plain fin correlations by assuming fins as rectangular ducts, the length of the heat exchanger is estimated once more. Theoretically calculated length has been found to be approximately 5% higher than the real condenser length. This result has a very good match when the experimental uncertainties are considered. It is inevitable to put into account developing turbulent flow effects. Actual condenser load is lower than the summation of the evaporator, post heater and compressor power. Air entrance structure in the heat exchanger and the air side surface roughness definitely affect heat transfer in a positive way.

5.4 Future Work

Entropy generation rate analysis for evaporator and condenser designs can be inspected for wider ranges. If compressor characteristics are fully known, an optimization algorithm might be developed instead of evaluating components separately.

There are many things to improve especially in the experimental part. Main struggle related to experimental set up is to maintain flow stability. In order to stabilize the flow, a pressure drop element might be implemented at the beginning of the channels or a needle valve might be placed before the channels. If some measuring devices are removed, it will reduce the pressure drop load of the condenser and help improve the stability. Although it will make the leakage issue more problematic, more thermocouples might be implemented on the evaporator. This way, the local heat flux can be calculated by Fourier's law, hence local heat transfer coefficients can be calculated and errors due to heat loss and the use of average temperatures are eliminated. Using this method, local heat transfer coefficients can be calculated instead of using an average heat transfer coefficient. More accurate pressure transducers can be used. In addition, an electronic expansion valve instead of a manual one can be used.

If custom made multilouvered fins could be implemented in the air cooled condenser, there will be a better chance of comparison between experimental and theoretical results.

A control algorithm might be developed and the cycle can be controlled automatically. With the help of such a control system, critical heat flux may be calculated and burnout in evaporator may be prevented by automatically regulating the mass flow rate and the cooling load.

REFERENCES

- [1] D. B. Tuckerman and R. F. W. Pease, “High-performance heat sinking for VLSI,” *IEEE Electron Device Lett.*, vol. 2, no. 5, pp. 126–129, 1981.
- [2] Y.-T. Wu, C.-F. Ma, and X.-H. Zhong, “Development and experimental investigation of a miniature-scale refrigeration system,” *Energy Convers. Manag.*, vol. 51, no. 1, pp. 81–88, Jan. 2010.
- [3] G. Türkakar and T. Okutucu-Özyurt, “Entropy generation analysis and dimensional optimization of an evaporator for use in a microscale refrigeration cycle,” *Int. J. Refrig.*, vol. 56, pp. 140–153, 2015.
- [4] R. Jafari, “Implementation of Metal-Based Microchannel Heat Exchangers in a Microrefrigeration Cycle, and Numerical and Experimental Investigation of Surface Roughness Effects on Flow Boiling,” Phd Thesis, METU, September 2015.
- [5] W. Yuan, B. Yang, Y. Yang, K. Ren, J. Xu, and Y. Liao, “Development and experimental study of the characteristics of a prototype miniature vapor compression refrigerator,” *Appl. Energy*, vol. 143, pp. 47–57, Apr. 2015.
- [6] Z. Wu and R. Du, “Design and experimental study of a miniature vapor compression refrigeration system for electronics cooling,” *Appl. Therm. Eng.*, vol. 31, no. 2–3, pp. 385–390, Feb. 2011.

- [7] Trutassanawin, S. E. a Groll, S. V Garimella and L. Cremaschi, “Experimental Investigation of a Miniature-Scale Refrigeration System for Electronics Cooling Experimental Investigation of a Miniature-Scale Refrigeration System for Electronics Cooling,” IEE Trabsactions on Components and Packaging Technologies., vol. 29, no. 3, pp. 678–687, 2006.
- [8] R. Mongia, K. Masahiro, E. DiStefano, J. Barry, W. Chen, M. Izenson, F. Possamai, a. Zimmermann, and M. Mochizuki, “Small scale refrigeration system for electronics cooling within a notebook computer,” *Therm. Thermomechanical Proc. 10th Intersoc. Conf. Phenom. Electron. Syst. 2006. ITherm 2006.*, pp. 751–758, 2006.
- [9] S. Mancin, C. Zilio, G. Righetti, and L. Rossetto, “Mini Vapor Cycle System for high density electronic cooling applications,” *Int. J. Refrig.*, vol. 36, no. 4, pp. 1191–1202, Jun. 2013.
- [10] S. S. Bertsch, E. a. Groll, and S. V. Garimella, “Refrigerant flow boiling heat transfer in parallel microchannels as a function of local vapor quality,” *Int. J. Heat Mass Transf.*, vol. 51, no. 19–20, pp. 4775–4787, Sep. 2008.
- [11] J. Lee and I. Mudawar, “Two-phase flow in high-heat-flux micro-channel heat sink for refrigeration cooling applications: Part II—heat transfer characteristics,” *Int. J. Heat Mass Transf.*, vol. 48, no. 5, pp. 941–955, Feb. 2005.
- [12] S. S. Bertsch, E. a. Groll, and S. V. Garimella, “Effects of heat flux, mass flux, vapor quality, and saturation temperature on flow boiling heat transfer in microchannels,” *Int. J. Multiph. Flow*, vol. 35, no. 2, pp. 142–154, Feb. 2009.

- [13] C.-C. Wang, C.-S. Chiang, and J.-G. Yu, "An experimental study of in-tube evaporation of R-22 inside a 6.5-mm smooth tube," *Int. J. Heat Fluid Flow*, vol. 19, no. 3, pp. 259–269, 1998.
- [14] Y. Yan and F. Lin, "Evaporation heat transfer and pressure drop of refrigerant R134a in a small pipe, *Int. J. Heat Mass Transf.*, 1998"
- [15] B. Sumith, F. Kaminaga, and K. Matsumura, "Saturated flow boiling of water in a vertical small diameter tube," *Exp. Therm. Fluid Sci.*, vol. 27, no. 7, pp. 789–801, 2003.
- [16] A. Greco, "Convective boiling of pure and mixed refrigerants: An experimental study of the major parameters affecting heat transfer," *Int. J. Heat Mass Transf.*, vol. 51, no. 3–4, pp. 896–909, 2008.
- [17] C. B. Tibiriçá and G. Ribatski, "Flow boiling heat transfer of R134a and R245fa in a 2.3mm tube," *Int. J. Heat Mass Transf.*, vol. 53, no. 11–12, pp. 2459–2468, May 2010.
- [18] X. Huo, L. Chen, Y. S. Tian, and T. G. Karayiannis, "Flow boiling and flow regimes in small diameter tubes," *Appl. Therm. Eng.*, vol. 24, no. 8–9, pp. 1225–1239, 2004.
- [19] M. W. Wambsganss, D. M. France, J. a. Jendrzejczyk, and T. N. Tran, "Boiling Heat Transfer in a Horizontal Small-Diameter Tube," *J. Heat Transfer*, vol. 115, no. 4, p. 963, 1993.
- [20] Z. Y. Bao, D. F. Fletcher, and B. S. Haynes, "Flow boiling heat transfer of Freon R11 and HCFC123 in narrow passages," *Int. J. Heat Mass Transf.*, vol. 43, no. 18, pp. 3347–3358, 2000.

- [21] R. Yun, Y. Kim, M. Soo Kim, and Y. Choi, "Boiling heat transfer and dryout phenomenon of CO₂ in a horizontal smooth tube," *Int. J. Heat Mass Transf.*, vol. 46, no. 13, pp. 2353–2361, 2003.
- [22] S. In and S. Jeong, "Flow boiling heat transfer characteristics of R123 and R134a in a micro-channel," *Int. J. Multiph. Flow*, vol. 35, no. 11, pp. 987–1000, Nov. 2009.
- [23] L. Wang, M. Chen and M. Groll, "Flow boiling heat transfer characteristics of R134a in a horizontal mini tube," *Journal of Chemical & Engineering Data.*, 54 (9), 2638-2645, DOI: 10.1021/je900140w, 2009.
- [24] R. Ali, B. Palm, and M. H. Maqbool, "Flow Boiling Heat Transfer Characteristics of a Minichannel up to Dryout Condition," *J. Heat Transfer*, vol. 133, no. 8, p. 081501, 2011.
- [25] J. B. Copetti, M. H. Macagnan, F. Zinani, and N. L. F. Kunsler, "Flow boiling heat transfer and pressure drop of R-134a in a mini tube: an experimental investigation," *Exp. Therm. Fluid Sci.*, vol. 35, no. 4, pp. 636–644, May 2011.
- [26] H.-K. Oh and C.-H. Son, "Evaporation flow pattern and heat transfer of R-22 and R-134a in small diameter tubes," *Heat Mass Transf.*, vol. 47, no. 6, pp. 703–717, 2011.
- [27] T. G. Karayiannis, M. M. Mahmoud, and D. B. R. Kenning, "A study of discrepancies in flow boiling results in small to microdiameter metallic tubes," *Exp. Therm. Fluid Sci.*, vol. 36, pp. 126–142, 2012.

- [28] M. Li, C. Dang, and E. Hihara, "Flow boiling heat transfer of HFO1234yf and R32 refrigerant mixtures in a smooth horizontal tube: Part I. Experimental investigation," *Int. J. Heat Mass Transf.*, vol. 55, no. 13–14, pp. 3437–3446, 2012.
- [29] R. Charnay, R. Revellin, and J. Bonjour, "Flow boiling heat transfer in minichannels at high saturation temperatures: Part II – Assessment of predictive methods and impact of flow regimes," *Int. J. Heat Mass Transf.*, vol. 87, pp. 653–672, 2015.
- [30] J. T. Oh, a. S. Pamitran, K. I. Choi, and P. Hrnjak, "Experimental investigation on two-phase flow boiling heat transfer of five refrigerants in horizontal small tubes of 0.5, 1.5 and 3.0 mm inner diameters," *Int. J. Heat Mass Transf.*, vol. 54, no. 9–10, pp. 2080–2088, 2011.
- [31] C. L. Ong and J. R. Thome, "Flow boiling heat transfer of R134a, R236fa and R245fa in a horizontal 1.030mm circular channel," *Exp. Therm. Fluid Sci.*, vol. 33, no. 4, pp. 651–663, Apr. 2009.
- [32] C. L. Ong and J. R. Thome, "Macro-to-microchannel transition in two-phase flow: Part 2 - Flow boiling heat transfer and critical heat flux," *Exp. Therm. Fluid Sci.*, vol. 35, no. 6, pp. 873–886, 2011.
- [33] C. Bigonha Tibiriçá, G. Ribatski, and J. Richard Thome, "Flow Boiling Characteristics for R1234ze(E) in 1.0 and 2.2 mm Circular Channels," *J. Heat Transfer*, vol. 134, no. 2, p. 020906, 2012.
- [34] Su, Q., Yu, G.X., Wang, H.S., Rose, J.W., 2008. Correlations and theory for microchannel condensation. In: Proceedings of ASME 6th International Conference on Nanochannels, Microchannels and Minichannels, Darmstadt, Germany, Paper no. ICNMM2008-62146, 23–25 June

- [35] E. Al-Hajri, A. H. Shooshtari, S. Dessiatoun, and M. M. Ohadi, "Performance characterization of R134a and R245fa in a high aspect ratio microchannel condenser," *Int. J. Refrig.*, pp. 1–13, Oct. 2012.
- [36] K. W. Moser, R. L. Webb, and B. Na, "A New Equivalent Reynolds Number Model for Condensation in Smooth Tubes," *J. Heat Transfer*, vol. 120, no. 2, pp. 410–417, 1998.
- [37] S. Koyama, K. Kuwahara, K. Nakashita, and K. Yamamoto, "An experimental study on condensation of refrigerant R134a in a multi-port extruded tube," *Int. J. Refrig.*, vol. 26, no. 4, pp. 425–432, Jun. 2003.
- [38] W. A. Khan, M. M. Yovanovich, and J. R. Culham, "Optimization of microchannel heat sinks using entropy generation minimization method," *Twenty-Second Annu. IEEE Semicond. Therm. Meas. Manag. Symp.*, pp. 78–86.
- [39] A. Jafari, N. M. Ghazali, M. a. Wahid, S. Samion, N. a. C. Sidik, and J. M. Sheriff, "Optimization of a Circular Microchannel With Entropy Generation Minimization Method," pp. 351–362, 2010.
- [40] H. Abbassi, "Entropy generation analysis in a uniformly heated microchannel heat sink," *Energy*, vol. 32, no. 10, pp. 1932–1947, Oct. 2007.
- [41] R. Revellin and J. Bonjour, "Entropy generation during flow boiling of pure refrigerant and refrigerant–oil mixture," *Int. J. Refrig.*, vol. 34, no. 4, pp. 1040–1047, Jun. 2011.
- [42] J. Sarkar, S. Bhattacharyya, and M. Ram Gopal, "Irreversibility minimization of heat exchangers for transcritical CO₂ systems," *Int. J. Therm. Sci.*, vol. 48, no. 1, pp. 146–153, Jan. 2009.

- [43] P. Saechan and S. Wongwises, "Optimal configuration of cross flow plate finned tube condenser based on the second law of thermodynamics," *Int. J. Therm. Sci.*, vol. 47, no. 11, pp. 1473–1481, Nov. 2008.
- [44] B. F. Pussoli, J. R. Barbosa, L. W. da Silva, and M. Kaviany, "Optimization of peripheral finned-tube evaporators using entropy generation minimization," *Int. J. Heat Mass Transf.*, vol. 55, no. 25–26, pp. 7838–7846, Dec. 2012.
- [45] G. Türkakar and T. Okutucu-Özyurt, "Dimensional optimization of microchannel heat sinks with multiple heat sources," *Int. J. Therm. Sci.*, vol. 62, pp. 85–92, Dec. 2012.
- [46] S. G. Kandlikar, S. Garimella, D. Li, S. Colin, and M. R. King, *Heat Transfer and Fluid Flow in Minichannels and Microchannels*. Elsevier, 2006.
- [47] G. Türkakar, "Numerical Simulation and Analytical Optimization of Microchannel Heat Sinks," MS Thesis, p. 133, August, 2010.
- [48] J. Lee and I. Mudawar, "Two-phase flow in high-heat-flux micro-channel heat sink for refrigeration cooling applications: Part I—pressure drop characteristics," *Int. J. Heat Mass Transf.*, vol. 48, no. 5, pp. 928–940, Feb. 2005.
- [49] Lockhart, R. W., and Martinelli, R. C., 1949, "Proposed Correlation of Data for Isothermal Two Phase Flow, Two Component Flow in Pipes," *Chem. Eng. Prog.*, 45, pp. 39–48.
- [50] S. G. Kandlikar and P. Balasubramanian, "An Extension of the Flow Boiling Correlation to Transition, Laminar, and Deep Laminar Flows in Minichannels and Microchannels," *Heat Transf. Eng.*, vol. 25, no. 3, pp. 86–93, Apr. 2004.

- [51] M. M. Mahmoud, T. G. Karayiannis, and D. B. R. Kenning, "Flow Boiling Pressure Drop of R134a in Microdiameter Tubes: Experimental Results and Assessment of Correlations," *Heat Transf. Eng.*, vol. 35, no. 2, pp. 178–192, Sep. 2013.
- [52] M. Asadi, G. Xie, and B. Sunden, "A review of heat transfer and pressure drop characteristics of single and two-phase microchannels," *Int. J. Heat Mass Transf.*, vol. 79, pp. 34–53, Dec. 2014.
- [53] W. Qu and I. Mudawar, "Measurement and prediction of pressure drop in two-phase micro-channel heat sinks," *Int. J. Heat Mass Transf.*, vol. 46, no. 15, pp. 2737–2753, Jul. 2003.
- [54] E. Costa-Patry, J. Olivier, B. A. Nichita, B. Michel, and J. R. Thome, "Two-phase flow of refrigerants in 85 μ m-wide multi-microchannels: Part I – Pressure drop," *Int. J. Heat Fluid Flow*, vol. 32, no. 2, pp. 451–463, Apr. 2011.
- [55] T. Okutucu, G. Türkakar, 2013. Optimization of microchannels for liquid cooling of electronic chips, 6 pp. In: Proceedings of 26th European Conference on Operational Research, Rome, Italy.
- [56] G. Türkakar, T. Okutucu-Özyurt, and S. G. Kandlikar, "Entropy generation analysis of a microchannel-condenser for use in a vapor compression refrigeration cycle," *Int. J. Refrig.*, vol. 70, pp. 71–83, 2016.
- [57] M. Kim and C. W. Bullard, "Air-side thermal hydraulic performance of multi-louvered fin aluminum heat exchangers / air des échangeurs de chaleur à Performance hydraulique côté persiennes ailettes en aluminium a," vol. 25, pp. 390–400, 2002.

- [58] T. M. Adams, M. F. Dowling, and S. M. Jeter, “Applicability of traditional turbulent single-phase forced convection correlations to non-circular microchannels,” vol. 42, pp. 4411–4415, 1999.
- [59] X.F. Peng, G.P. Peterson, Convective heat transfer and flow friction for water flow in microchannel structures, *International Journal of Heat and Mass Transfer*, Volume 39, Issue 12, 1996, Pages 2599-2608, ISSN 0017-9310, [http://dx.doi.org/10.1016/0017-9310\(95\)00327-4](http://dx.doi.org/10.1016/0017-9310(95)00327-4).
- [60] K. Mishima, T. Hibiki, Some characteristics of air-water two-phase flow in small diameter vertical tubes, *International Journal of Multiphase Flow*, Volume 22, Issue 4, 1996, Pages 703-712, ISSN 0301-9322, [http://dx.doi.org/10.1016/0301-9322\(96\)00010-9](http://dx.doi.org/10.1016/0301-9322(96)00010-9).
- [61] A. Cavallini, L. Doretto, M. Matkovic, and L. Rossetto, “Update on Condensation Heat Transfer and Pressure Drop inside Minichannels,” *Heat Transf. Eng.*, vol. 27, no. 4, pp. 74–87, May 2006.
- [62] T. Staff and T. Laboratories, “Estimation of Steady-State Steam,” pp. 4–8, 2015.
- [63] M.J. Moran, *Availability analysis: A guide to efficient energy use*, Prentice-Hall, Englewood Cliffs, N.J, 1982.
- [64] T. L. Bergman, A. S. Lavigne, F. P. Incropera, and D. P. Dewitt, *Fundamentals of Heat and Mass Transfer*. 2011.
- [65] S. Kakac, R.K. Shah, W. Aung, *Handbook of Single Phase Convective Heat Transfer*, John Wiley and Sons, New York, 1987.
- [66] W. M. Kays, and M. E. Crawford, 1987. *Convective Heat and Mass Transfer*, 2nd ed., McGraw-Hill, New York.

CURRICULUM VITAE

PERSONEL INFORMATION

GÖKER TÜRKAĞAR

Department of Mechanical Engineering, A-122

Middle East Technical University (METU)

06530 Ankara/TURKEY

+90 312 210 52 80

+90 505 721 62 85

turkakar@metu.edu.tr

EDUCATION

2010 – 2016 (expected)

Ph.D

Middle East Technical University, Ankara – Turkey

Mechanical Engineering

Thesis Title: ” Design, Optimization and Testing of Micro-Evaporator and Micro Condenser Components Used in a Miniature Vapor Compression Refrigeration Cycle”

Supervisor: Dr. Tuba Okutucu Özyurt

CGPA: 3.56/4.00

March-Dec 2015	<p>PhD Visiting Scholar</p> <p>Mechanical Engineering</p> <p>Rochester Institute of Technology, Rochester, NY, USA</p> <p>Supervisor: Dr. Satish G. Kandlikar</p>
2007 – 2010 August	<p>M.S.</p> <p>Middle East Technical University, Ankara – Turkey</p> <p>Mechanical Engineering</p> <p>Thesis Title:” Numerical simulation and analytical optimization of microchannel heat sinks ”</p> <p>Supervisor: Dr. Tuba Okutucu Özyurt</p> <p>CGPA: 3.00 /4.00</p> <p>Graduation Date: August 2010</p>
2002 – 2006 June	<p>B.S.</p> <p>Osmangazi University, Eskişehir – Turkey</p> <p>Mechanical Engineering</p> <p>CGPA: 3.18/4.00</p> <p>Graduation Date: June 2006</p>

PROFESSIONAL PROFILE

Research and Teaching Assistant, Middle East Technical University (METU), Ankara, Turkey, 2007- Present.

PROJECTS

Designing, Manufacturing and Testing of a Vapor Compression Cycle in Micro Scale, funded by The Scientific and Technological Research Council of Turkey, Project no: 112M168, (January 2012-November 2015)

ACADEMIC HONORS AND AWARDS

- METU Foundation for Amelioration (ODTÜ Geliştirme Vakfı). Award for International Publications, 2016
- Publication Incentive Award, TÜBİTAK (The Scientific and Technological Research Council of Turkey), 2015
- METU Foundation for Amelioration (ODTÜ Geliştirme Vakfı). Award for International Publications, 2015
- TUBITAK International Doctoral Research Fellowship Programme Scholarship, 9 months (March-December 2015)
- Publication Incentive Award, TÜBİTAK (The Scientific and Technological Research Council of Turkey), 2013
- METU Foundation for Amelioration (ODTÜ Geliştirme Vakfı). Award for International Publications, 2013

ACADEMIC/TEACHING EXPERIENCE

Graduate Teaching Assistant, Middle East Technical University, Mechanical Engineering Department, 2007-Present

- ME 203 - Thermodynamics 1
- ME 204 – Thermodynamics 2
- ME 311 – Heat transfer
- ME 312 – Thermal Engineering
- ME 351 – Thermodynamics of Heat Power
- ME 410 – Mechanical Engineering Systems Laboratory
- ME 423 – Gas Turbines and Jet Propulsion
- ME 424 – Steam Power Plant Engineering

PUBLICATIONS

Refereed Journal Publications

1. Göker Türkakar, Tuba Okutucu-Özyurt, Satish G. Kandlikar, Entropy generation analysis of a microchannel-condenser for use in a vapor compression refrigeration cycle, International Journal of Refrigeration, Volume 70, October 2016, Pages 71-83, ISSN 0140-7007, <http://dx.doi.org/10.1016/j.ijrefrig.2016.06.028>.
2. Türkakar, G., Okutucu-Özyurt, T. (2015). Entropy generation analysis and dimensional optimization of an evaporator for use in a microscale refrigeration cycle. International Journal of Refrigeration, 56, 140–153. doi:10.1016/j.ijrefrig.2015.04.003
3. G. Türkakar, T. Okutucu-Özyurt, "Dimensional Optimization of Microchannel Heat Sinks with Multiple Heat Sources", International Journal of Thermal Sciences (ISI) 62, 85-92 pp., 2012 , DOI: 10.1016/j.ijthermalsci.2011.12.015

Refereed Conference Proceedings

1. Türkakar, G., Okutucu-Özyurt, T., International Symposium on Thermal and Materials Nanoscience and Nanotechnology, "Proceedings of the International Symposium on Thermal and Materials Nanoscience and Nanotechnology", "Effects of Thermophysical Properties and Entrance Region on the Dimensional Optimization of Microchannel Heat Sinks", 042(CD) pp., Antalya, Turkey, June 2011
2. Okutucu, T., Türkakar, G., Abstract in 26th European Conference on Operational Research Conference, 6 pp., 2013 "Optimization of microchannels for liquid cooling of electronic chips", Rome, Italy, 1-4 July 2013.
3. Koyuncuoğlu, A., Türkakar, G., Redmond, M., Okutucu-Özyurt, Tuba., Külah, H., Kumar, S., International Symposium on Convective Heat and Mass Transfer, Conv 14, "An Experimental Study on Performance Enhancement of CMOS Compatible Monolithic Microchannel Heat Sinks", Kuşadası, Turkey, 8-13 June, 2014.
4. Türkakar, G., Okutucu-Özyurt, Tuba., The 15th International Heat Transfer Conference, "Irreversibility Analysis of an Evaporator for Use in a Micro-Refrigeration Cycle", Kyoto, Japan, 10-15 August, 2014.

Refereed National Conference Proceedings

1. Türkakar, G., Okutucu Özyurt, T., “Çoklu Isı Kaynaklı Mikrokanallı Isı Alıcılarının Boyutsal Optimizasyonu,” Proc. Of 19th National Thermal Sciences and Technology, Editors, Haşmet TÜRKOĞLU, Aydın DURMUŞ, Lütfü NAMLI, 345-355 pp., Samsun, Turkey 09 - 12 September 2013.

RESEARCH INTERESTS

Dimensional optimization of microchannel heat sinks, micro refrigeration cycles, entropy generation minimization in microchannels, heat transfer and fluid flow in microchannels, electronics cooling.